

THESIS ON MECHANICAL AND INSTRUMENTAL ENGINEERING E54

Hard PVD Coatings for Tooling

ANDRE GREGOR

TUT
PRESS

Faculty of Mechanical Engineering
Department of Materials Engineering

**Dissertation was accepted for the defence of the degree of Doctor of
Philosophy in Engineering on November 5, 2009**

Supervisor: Prof. Priit Kulu, Faculty of Mechanical Engineering, Department of
Materials Engineering

Oponents: Prof. Jakob Kübarsepp, Vice Rector for Academic Affairs, TUT
Prof. Jari Koskinen, Aalto University School of Science and
Technology, Dept. of Materials Science and Engineering

Defence of the thesis: June 18, 2010

Declaration:

Hereby I declare that this doctoral thesis, my original investigation and
achievement, submitted for the doctoral degree at Tallinn University of
Technology has not been submitted for any academic degree.

Copyright: Andre Gregor, 2010

ISSN 1406-4758

ISBN 978-9949-23-006-8

MASINA- JA APARAADIEHITUS E54

PVD kõvapinded tööriistamajanduses

ANDRE GREGOR

CONTENTS

INTRODUCTION	7
Acknowledgements.....	8
Author’s contribution.....	8
ABBREVIATIONS AND SYMBOLS	9
1 REVIEW OF THE LITERATURE.....	10
1.1 PVD technology.....	10
1.1.1 History.....	10
1.1.2 PVD coatings – global trends.....	10
1.1.3 AIP technology	11
1.1.4 Ion nitriding, duplex coatings and duplex treatment.....	32
1.2 Process/microstructure/property relationship.....	35
1.2.1 Thorton-Messier structure zone diagram	35
1.2.2 Mono -, multilayer, gradient and nanostructured coatings.....	37
1.2.3 Residual stresses	40
1.2.4 Surface roughness	40
1.3 Friction and wear properties of coatings.....	41
1.3.1 Friction.....	41
1.3.2 Wear mechanisms	43
1.4 Application areas of hard PVD coatings.....	46
1.5 Conclusions to the chapter and aims of the study	47
2 EXPERIMENTAL	50
2.1 Studied systems.....	50
2.1.1 Studied substrates and coatings.....	51
2.1.2 Sampling	52
2.2 Characterisation of studied systems	52
2.2.1 Characterisation of microstructure.....	52
2.2.2 Characterisation of “substrate – coating” system properties.....	56
2.2.3 Characterisation of friction and wear.....	64
3 TECHNOLOGY AND PROPERTIES OF COATINGS	70
3.1 Study of commercial coatings.....	70
3.1.1 Characterisation of studied systems.....	71
4 SELECTION OF HARD COATINGS FOR TOOLING	131
4.1 Selection based on the properties of the system substrate – coating.....	132
4.2 Selection based on wear conditions/operation parameters.....	136
CONCLUSIONS.....	138
REFERENCES	140
LIST OF PUBLICATIONS	151
ABSTRACT.....	152
KOKKUVÕTE	153
CURRICULUM VITAE (CV).....	154
ELULOOKIRJELDUS	157

TEADUS

Akna taga, tühjus haigutab
kaua veel peab ootama ...
valges mees nüüd nuppu vajutab
katood see lõpuks käivitus

Elektronid, sula osad
kambris kandusid nüüd laiali
kõrge pinge, vool ja kuma
leegi kaarja moodustasid

Mähis kiirendab ja tõukab takka
kümme kilomeetrit sekundis
temperatuur see veel ei hakka
puldil numbreid näitama

Avab kraani üks või kaks
gaas nüüd pääseb kambrisse
sadestub seal pinne paks
seitse või kaheksa mikronit

Titaannitriid ja aluuminum
on ained, mis sulavad kokku
mu arvates see katsete seeria
on jõudnud peaaegu lõppu

Vaakumpump ja heitgaasi voolik
vesijahuti ta sulgeb
võtab mütsi ... jope nagist
... kodu poole kulgeb.

Author, Tallinn 2006

INTRODUCTION

In the vacuum vaporization of metals such coatings as anticorrosive, wear-resistant, refractory, antifriction, superconductive, optical etc. can be produced. The vacuum-arc deposition (VAD) technology makes it possible to produce coatings from any metals.

In a vacuum arc plasma coating equipment a consumable cathode is vaporized by means of a vacuum arc discharge, a plasma flow of the metal vapour is formed, said metal being in a highly ionised state at a high value of energy and concentration of particles, and in the following condensation thereof forming a coating [1].

Hard coatings based on transition metal nitrides and carbides are widely used today to protect materials against wear, abrasion and corrosion [2, 3, 4, 5]. Due to their remarkable properties such as high microhardness, chemical inertness, high wear and abrasion resistance, these coatings are employed in various machining applications to improve the performance of tools and mechanical components.

During the past decades, interest in transition metal nitrides has grown considerably. Nitrides of various elements play an important role in industry, science, and technology for their interesting and useful resilient properties. For example, many transition metal nitrides based on titanium, boron, and nitrogen have stimulated commercial interest because of their extreme hardness, wear and corrosion resistance, and thermal and electrical properties [6].

The increasing demands in performance of high speed dry machining resulted in a rapid progress to produce coatings with good wear and oxidation resistance at high temperatures. Of these coatings, those made of TiAlN have successfully been applied as protective films on cutting tools [1, 7]. Their better performance as compared to that of the current wear resistant films (TiN, TiC, Ti(C, N)) was attributed to the formation of an aluminium oxide layer on the film surface. Since multilayer coatings often exhibited better features for industrial applications than single layer coatings, TiAlN based multilayers such as alternate TiAlN/CrN, TiAlN/TiN or TiAlYN/VN founded the use in protecting machine parts and tools [8, 9, 10, 11].

The aim of the study is focused on the architecture and characterization of coatings and substrates that can be used in tooling. The need of study of the selection of appropriate substrate material and heat treatment technique, coating material and architecture with its unique physical and chemical properties for particular application.

Acknowledgements

First of all I would like to express my deep gratitude to my supervisor professor Priit Kulu, of the Department of Materials Engineering, for continuous support, encouragement and valuable advice during this work.

I would like to thank my colleagues Fjodor Sergejev, Andrei Surzenkov, Mart Saarna, Alina Sivitski, Valdek Mikli, Can Emrah Yaldiz, Vitali Podgursky, Eron Adoberg, Tiit Varema, Priidu Peetsalu, and Irina Hussainova for their contribution in evaluation of coatings and their technical assistance.

During this work I had the pleasure of collaboration with Esko Harju from Helsinki University and Benny Andre from Uppsala University.

Many thanks to my other colleagues from TUT, Department of Materials Engineering and Department of Thermal Engineering and my gratitude to my colleagues from Eesti Innovatsiooni Instituut for their patience.

I express my gratitude to my mother Kai and father Vitali for their patience and encouragement.

Author's contribution

The author of this thesis took part in sample preparation routine, was responsible for carrying out of the experiments, collecting, processing and further analysis of experimental data. The intellectual merit, which is the result of the framework where the contribution of every author should not be underestimated.

ABBREVIATIONS AND SYMBOLS

AFM	-	Atomic Force Microscope
AIP	-	Arc Ion Plating
CAE	-	Cathodic Arc Evaporation
CIB	-	Condensation with Ion Bombardment
CoF	-	Coefficient of Friction
EDS	-	Energy Dispersive X-ray Spectroscopy
EGR	-	Exhaust Gas Recirculation
FR	-	Fracture Ratio
H/E ratio	-	Hardness – Elastic modulus ratio
HCM	-	Hollow Cathode Magnetron
HIP	-	High Isostatic Pressure
HM	-	Hardmetal
HSS	-	High Speed Steel
CWTS	-	Cold Working Tool Steel
IBAD	-	Ion Beam Assisted Deposition
MePIII&D	-	Metal Plasma Immersion Ion Implantation & Deposition
MPSIID	-	Metal Plasma Source Ion Implantation Deposition
OECD	-	Organization for Economic Cooperation and Development
PAPVD	-	Plasma Activated Physical Vapour Deposition
PBII	-	Plasma Based Ion Implantation
PIII&D	-	Plasma Immersion Ion Implantation & Deposition
PIIID	-	Plasma Immersion Ion Implantation Deposition
PIIP	-	Plasma Ion Implantation Process
PIN	-	Plasma Ion Nitriding
PIP	-	Plasma Ion Plating
PLD	-	Pulsed Laser Deposition
PM	-	Powder Metallurgy
PSII	-	Plasma Source Ion Implantation
PVD	-	Physical Vapour Deposition
RMS	-	Root Mean Square
RPM	-	Revolution Per Minute
SCCM	-	Standard Cubic Centimetre
SEM	-	Scanning Electron Microscope
SF	-	Spray Formed
TM	-	Melting Temperature
UBM	-	Unbalanced Magnetron Sputtering
UHV	-	Ultra High Vacuum
VAD	-	Vacuum Arc Deposition
VAE	-	Vacuum Arc Evaporation
σ	-	Residual stresses

1 REVIEW OF THE LITERATURE

1.1 PVD technology

1.1.1 History

The History of cathodic arc plasma deposition maybe traced back to the 18th century. The observation of pulsed and later continuous discharges is closely related to invention of electrical storage (the capacitor and electrochemical battery). Based on discharges of capacitor banks, Joseph Priestley observed the formation of coatings on glass as early as 1766.

Continuous arc discharges were made by *Vassili Petrov* in St. Peterburg (1803) and independently by *Humphry Davy* in London (1808). These developments were mentioned in recent publication [12].

Much understanding was gained by *Michael Faraday's* discovery of electromagnetic induction in 1831 and James *Maxwell's* theory of electromagnetism in 1873. First practical applications of cathodic arc coatings were patented by *Thomas Alva Edison* [12]. Cathodic arcs remained a subject of research with tough challenges, with application in switching rather than coating.

Researcher *Tanberg* developed clever techniques to uncover the secrets of cathode spot physics [12]. With the grow of industrial demand after WWII, cathodic arc coating technology was rediscovered.

Arc plasma sources for DC (direct current) operation were developed in the United States of America and in former Soviet Union. Of particular importance were the patents by *Snaper et al.* [13, 14] and *Sablev et al.* [15, 16, 17, 18, 19] because they describe the basic design of these sources. Leading companies like Multi-Arc Inc. and Vapour Technologies Inc. who first replicated and later improved Soviet arc technology used DC arc sources.

1.1.2 PVD coatings – global trends

Nanostructured and nanocomposite coatings are new branch of materials that possess unique physical and mechanical properties. A nanocomposite coating comprises of at least two phases: a nanocrystalline phase and an amorphous phase, or two different nanocrystalline phases. Toughness and hardness are important aspects for coating applications in manufacturing industry. Hardness is defined as a resistance of a material to plastic deformation. Now, it is accepted that materials can be classified as hard, superhard or ultrahard for hardness over 20, 40 or 80 GPa, respectively [20, 21, 22]. However, for engineering applications, hardness must be complimented with high toughness, which is a property of equal importance. Toughness is an important mechanical property related to the materials resistance against impact loads and it describes the resistance against the formation

of cracks [21]. Two most important trends in modern coatings technology are the development of hard yet tough nanocomposite and thick PVD coatings.

1.1.3 AIP technology

PVD AIP (Arc Ion Plating) process has been used for industrial coating deposition for more than 40 years. A term “Ion plating” has introduced by *Mattox* as early as in 1964 [23]. Use of TiN as a coating material decreases friction and wear, increases corrosion resistance of materials, protects substrate from overheating, and improves decorative properties of articles. Unfortunately, the use of a conventional DC AIP for such modern coatings as (TiAl)N, TiC, CrN, (TiC)N, (TiAl)N, ZrN, MoS₂, DLC, including multilayered ones, is bounded by parameters of existing technological equipment and methods of coating deposition. Coatings deposited using conventional technologies are characterized by low adhesion strength, high roughness, heterogeneous structure, and low wear resistance [24].

The use of thin, wear-resistant PVD coatings such as titanium nitride (TiN) on cutting and forming tools has become widely established over the last 15 years. However, the expansion of PVD applicability into other areas has been constrained by limitations on the coating thickness. Hard coatings like TiN normally contain a high degree of internal (usually compressive in-plane) stresses owing to lattice distortion and thermal mismatch effects; it is, therefore, difficult to produce single-layer TiN coatings thicker than 6–8 μm, without encountering adhesion problems on typical substrate materials employed [25].

Hard coatings are used to enhance the wear and corrosion resistance of the surfaces of materials. For the purposes of wear resistance, transition metal nitride and carbide coatings have proved extremely successful [26] and hence such coatings are widely used on cutting and shaping tools. Reactive cathodic arc evaporation (CAE) is one physical vapour deposition technique employed to produce such coatings. It has been found that the adhesion between the coating and the substrate is improved if, prior to deposition of the coating, the substrate surface is sputter cleaned in high vacuum using ionised species of the metal used in the coating. This sputtering process cleans the substrate surface by removing surface oxides and other contaminants. It also produces an interface region between the substrate and the coating in the form of a layer of graded composition [27, 28].

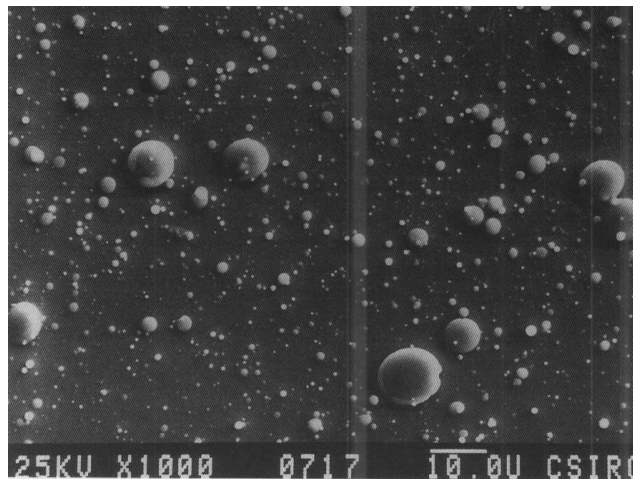


Figure 1.1. SEM image of microdroplets on the surface of Ti-film deposited by CAE [37].

Wear-resistant PVD coatings have found widespread applications in areas such as metal cutting and metal sheet forming. Depending on deposition parameters, such as bias voltage, nitrogen pressure, arc current and temperature, a wide range of coating properties may be expected [26, 27]. The CAE method is a successful physical vapour deposition (PVD) technique. However, the method may produce unwanted droplets or macroparticles, which can lead to poor adhesion, low density and increased surface roughness (Figure 1.1) [29, 30, 37].

The production of vacuum arc

First commercial PVD equipment was designed and manufactured in former Soviet Union in Ukraine and mostly for the purposes of the military needs. These first commercial PVD process coaters were named as „Bulat“ and were produced in early 1970-s. First US patents were filed by *Snaper* [13] from Institute of Plasma Physics (National Science Centre) in 1971 and by *Sablev* et al. at 1974 [15] followed by *Andreev* et al. and *Axenov* et al., [1, 31, 32, 33, 34] from Kharkov Institute of Physics and Technology. They were the leading scientists in a PVD technology during that time.

Vacuum environment protects the processes against attack from atmospheric gases. Large mean free paths and low boiling points in vacuum are helpful in depositing thin films. Low-pressure vacuum arcs can provide more energy to the deposit films at lower temperatures. Plasma can be manipulated with electric and magnetic fields. This has been exploited in exploiting plasma interactions with materials and developing novel techniques of thin film deposition. Material to be deposited is heated and vaporized in vacuum. The vapours condense on the substrates, which

are kept at specified distance from the vapour source. Often the substrates are cleaned *in situ* using glow discharge plasma. This improves the adhesion of the film. Increasing the substrate temperature improves the adhesion further and also helps in getting denser films with fewer voids. Resistive heating, high-energy electron beam heating and induction heating are some of the options available for vaporizing the source material. Using several sources it is possible to deposit multilayer films.

The basic principles of PAPVD / IBAD technique

The basic principle of PAPVD (Plasma Assisted Physical Vapour Deposition) is illustrated in Figure 1.2. The substrate is bombarded with energetic ions while the film is being deposited. The ions – could be argon – may have energies up to 1 keV. These ions share their energy and momentum with the depositing atoms. As a result the mobility of the depositing atoms increase leading to denser films. It is like shaking a bottle while filling it with grains. As the ratio of ion flux to the flux of the depositing atoms increase the number of voids in the film decrease making it denser. Increasing the energy of the ions or the temperature of the substrate has an effect. However, the bombarding atoms can also sputter away some of the atoms being deposited and reduce the rate of film growth. Ion bombardment increases the substrate temperature and influences the film growth further. In addition, if the same ions bombard the substrate before deposition, the impurities sitting on the surface and possibly some atoms of the substrate as well get etched away. This enhances the bonding between the substrate and the depositing atoms. There are several ways in which ion bombardment can be realized. In the system shown in Figure 1.2, an ion source is added to a conventional PVD system. Flux and energy of argon ions can be controlled independently [35].

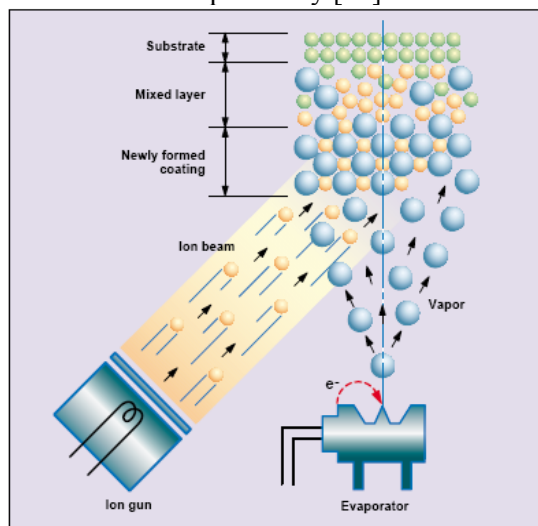


Figure 1.2 IBAD source is used to deposit dense, low stress coatings with improved adhesion [36].

Cathodic arc evaporation

Vacuum arc is a metal vapour arc in a vacuum environment [37, 38, 42]. An electric direct current arc is generated when the flow of current is suddenly interrupted. It is seen as bright flash of light. This normally occurs when mechanical switches are operated, at loose contacts etc. During an arc the electrode material evaporates and reacts with atmospheric gases. This gets deposited as a coloured layer on nearby surfaces. An electric arc can also be generated in vacuum. A voltage is applied between the cathode and the anode, which could be the wall of the vacuum chamber. The cathode is brought in contact with the anode using an igniter. A large current flows. When the igniter is withdrawn the arc is generated on the cathode surface. One can see bright spots – called the cathode spots – moving randomly all over the cathode surface. A current is maintained in the circuit. It could be few tens of amperes to few kilo amperes. It is limited only by the power source. The voltage across the electrodes falls to about 25 V. This is called as a random arc. Most of the processes of the arc occur very close to the cathode spot that has a short life of 100 – 120 ms (Figure 1.3 a) and occupies a tiny space of 10 – 30 μm . This transient nature makes it difficult to study the arc. These spots move randomly in the absence of any magnetic field. As one spot dies another is born some where along the periphery of the dying spot. The physical phenomena of cathode spots are roughly understood and several theories are given in following publications [37, 38, 42]. The current density per square meter in the surface of the target is between $10^6 - 10^8 \text{ A/m}^2$. This locally heats up the cathode to very high temperatures of the order of 10000 $^\circ\text{C}$ [68] and an area corresponding to the cathode spot melts. This micro pool of molten cathode emits electrons by thermionic and field emission processes. These electrons ionise the vapours of the cathode material escaping the molten pool. Extremely high-density plasma ($10^{24} - 10^{26} \text{ m}^{-3}$) is formed very close to the cathode. This plasma is of the cathode material. It is not necessary to have any gas to maintain the arc discharge. Cathodic arc is also known as vacuum arc. Some of the ions from the plasma are attracted to the cathode. The escaping vapours also exert a pressure on the molten pool. These two factors cause splattering of the molten cathode material leading to emission of droplets of various sizes – sub-microns to a few microns-at large angles to the normal of the cathode surface. It is observed that the ions are multiply ionised. Ions with charge states up to 6^+ have been observed. Ions from low melting point metals like lead are singly ionised while for refractory metals average ion charges up to 3^+ are observed. The degree of ionisation is seen to decrease with increasing arc current. It is possible that multiple ionisations are caused by multiple collisions with electrons in the high-density plasma close to the cathode. But the details need to be understood. The ions from the cathodic arc can have energies up to 150 eV. This is more than the cathode voltage of about 19 – 30 V. Two alternate explanations have been put forward to explain this anomaly. As per the potential hump theory [39], a region of higher potential is formed near the cathode due to excess ionisation. Ions in this region are accelerated large energies. The alternate

explanation is called the gas dynamic theory [40]. According to this, multiple collisions with electrons in the region of high density plasma leads to ion acceleration. If this is true, the ion energy should be independent of its charge state while as per potential hump theory higher charge state ions should have higher energy. There is no unambiguous evidence in favour of either of the explanations. Coatings obtained from cathodic arc sources are very dense and adhesion to the substrates is good. This is because the bombarding ions have high energy, which can be further, increased by biasing the substrates. Since the plasma is almost fully ionised, the ion to atomic flux ratio is very high. The films are usually free of voids. The only problems associated with the cathodic arc are the formation of micro droplets that are emitted from the molten pool of the cathode spot. These make the coatings rough and textured. This is not acceptable for some applications like optical coatings. Several techniques have been devised to get smooth films. Some are briefly discussed below.

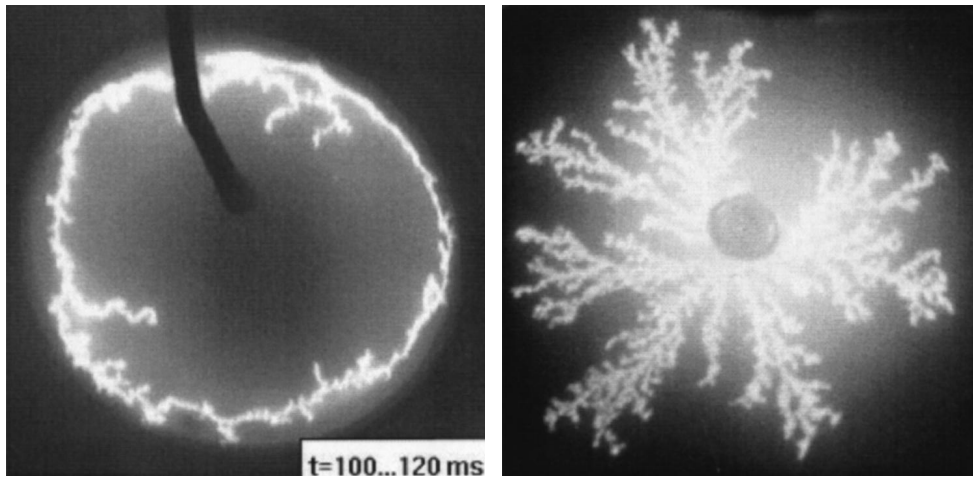


Figure 1.3. Cathodic arc for (a) DC arc discharge with arc current of 100 A, pulse duration of 100 – 120 ms and (b) AC discharge with high current arc - peak arc current 5000 A, pulse duration 1 ms. Evaporated mass of the target material was 3 and 2 mg accordingly [41].

The number of cathode spots can be reduced by applying external magnetic fields, however there are no method in existence that completely prevents the droplet deposition on the substrates without special optical handling systems [41]. The use of AC laser triggered VAD technology developed in Fraunhofer IWS. A comparison of conventional DC and AC high current arcs are given in Figure 1.3 b. Such technology allows to increase the average arc current and subsequently the deposition rates; to increase the arc spot velocity from average 10 m/s for DC VAD to 50 m/s for AC VAD resulting in reduced number of macroparticles on the substrate [41].

Here, another more common attempt is to minimize the splattering and production of microdroplets [33, 42] by using a magnetic field as shown in Figure 1.4 and in Figure 1.5 enables to control and increase arc spot movement velocity. The basic phenomenon that facilitates magnetic control of cathode spot location and motion is known as *retrograde motion*. When a magnetic field B is present in the vicinity of the cathode onto whose surface a current vector I is directed, there is a strong tendency for the cathode spot to move in the direction opposite to the force *e.g.* $-(I \times B)$ as shown in Figure 1.5 b. Various explanations are offered to understand this [42, 45]. The retrograde movement velocity of the vacuum arc increases linearly with the magnetic field strength B and decreases with gas pressure and temperature rise of the cathode surface. Plasma expansions up to high velocities of 3–5 km/s are present during arcing [45]. The velocity of steered arc is in the range of 2 – 90 m/s [37, 42]. With the aid of magnetic arc steering the residence time of the cathode spot at each position is reduced. The size of the molten metal pool and hence the amount of splattering is minimized. The number of macro particles in the film is reduced considerably. The angular distribution of the macro-particles also changes. Magnetic field cannot be increased indefinitely as at higher fields (~ 50 mT) the arc becomes unstable. The reduction of the number of macroparticles is more pronounced in the case of reactive deposition. This is due to the fact that magnetized electrons near the cathode excite, disassociate and ionise reactive gases like nitrogen and form a thin layer of high melting point film – say titanium nitride – on the cathode. This is seen as a deep purple hue emanating at the arc and spreading out along field lines. On such films cathode spots move faster, resulting shorter residence time of arc spot. Complete elimination of macro particles is not possible with the steered arc. Large steered arc cathodes are being used in industry for the deposition of cutting tools, decorative coatings and other applications.

Another modification of the arc steering system consists of non-uniform magnetic field generated by a combination of coils and pole pieces (Pos. 6. in Figure 1.4 a and Figure 1.5). At the cathode, the field lines form an acute angle [42, 63, 45]. The acute angle α with the side surface of the cathode (Figure 1.5 a Pos. 22) [17, 43] is defined by the lines of force (Figure 1.5 a Pos. 21) of the magnetic field B . This confines the plasma to a small region in the centre. The emission of droplets is reduced as in the steered arc. The expanding plasma encounters the non-uniform and strong magnetic field near the pole gaps. Here as it gets compressed and density increases. The electrons and ions bombard the droplets escaping from the cathode. Smaller drops are completely vaporized and larger ones become smaller. The net effect is an increase in plasma density and a decrease in the number of macro particles. It is said that the coating could be made almost free of macro-particles. But it is difficult to have large cathodes for industrial requirement. As an alternate one can increase the number of cathodes in the coating system.

Here, the short description of operation of early AIP evaporator. Plasma of the coating material said metal is generated from the surface of the electrode, often

also called „target“ and „cathode“ (Pos. 1 in Figure 1.4). Plasma is initiated by the trigger (Pos 10 in Figure 1.4), which momentarily generates an electric arc between the trigger (it is electrically connected with the anode) and the target and creates a spot or series of spots. After the plasma is initiated, the trigger electrode is silenced and the current flow is created between the target and the anode.

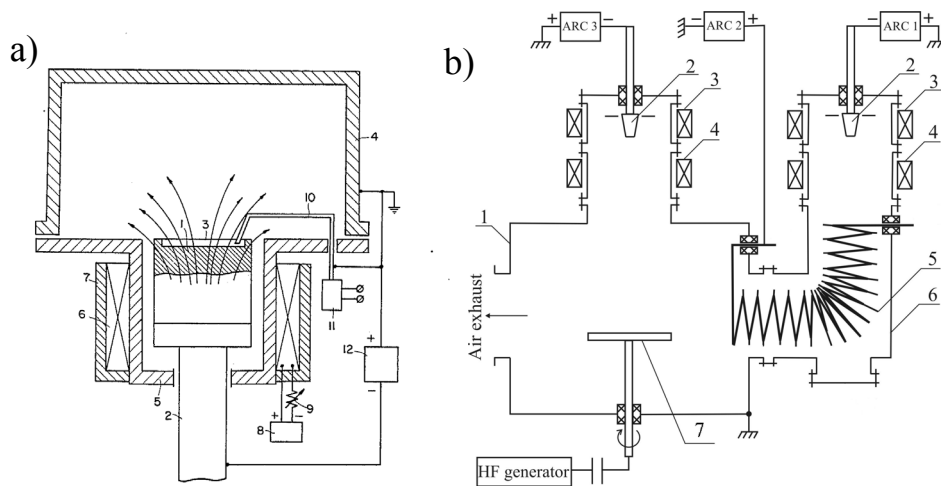


Figure 1.4. Early design of PVD arc evaporators [33]: a - illustration of AIP processing unit Bulat-6, and b – the same with macroparticle filter [44].

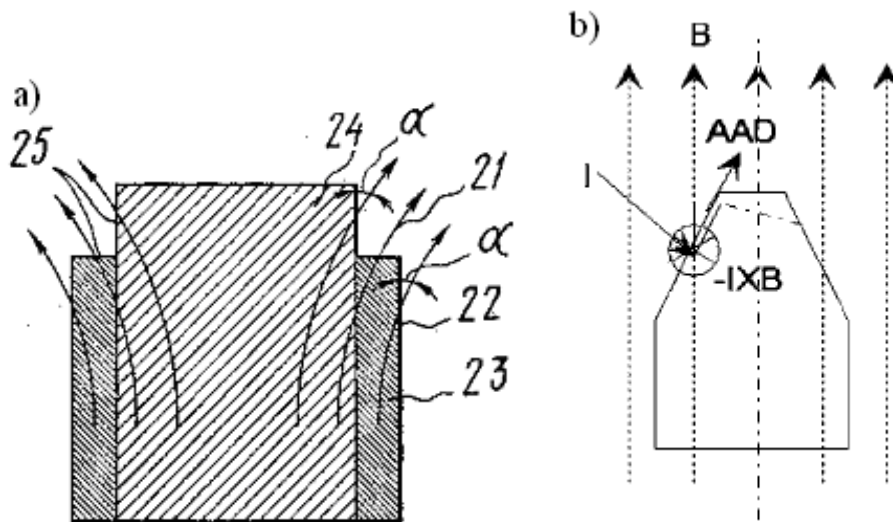


Figure 1.5. A composite cathode made of two different metals: a - the lines of force (21) of the magnetic field B and acute angle α [17, 45], and b – a “Frustum cone” – type cathode [45].

As the arc current flows between the anode and cathode, plasma-generating spots are created on the cathode surface and the spots tend to move randomly or chaotically over the front surface of the cathode. The cathode and the mount (Pos. 2 in Figure 1.4 a) are placed in a barrel (Pos. 5 in Figure 1.4 a) made of non-magnetic material, carrying the magnetic coil (pos. 6 in the Figure 1.4 a). The coil is disposed below the plasma-generating surface (Pos. 3 in Figure 1.4 a) of the cathode so that the force lines (shown by arrows in Figure 1.4 a and Figure 1.5) of the magnetic field thereof are inclined to periphery of the plasma-generating surface of the cathode. The coil is covered with the magnetic circuit (Pos. 7 in Figure 1.4 a), which increases the inclination of the force lines of the magnetic field of the coil in relation to the plasma-generating surface of the cathode, which intensifies the effect of magnetic field on the movement of cathode spots over the cathode surface. The magnetic field is used to spread or enlarge the evaporative surface area on the cathode. By proper adjustment of the coil current (coil current is between 0 – 0.6A and strength of the magnetic field is held between 0.5 – 8 mT), the plasma can be caused to spread out over the entire operating or evaporative surface of the cathode. A “Frustum cone” – type cathode is used to cause greater efficiency in the vapour deposition process as the retrograde upward spiralling motion of the cathode spot results in more efficient utilization of cathode [45] (Figure 1.5 b). The cathode is connected to the negative potential of the DC power supply and anode to the positive potential respectively. The current flow between the cathode and anode is adjustable between 50 – 150A and has a arc supply source voltage of 20 – 30V [33]. This design evolves still a small cathode evaporative surface area and will cause an emission of a large number of macroparticles (Figure 1.1), which will deposit on the surface of the substrate. Secondly, this design did not evolved resistive heaters inside the vacuum chamber, so substrates have to be heated up by ion bombardment of gaseous and/or metallic ions prior to the deposition. This design evolves a bias power supply (bias voltage up to 1.7 kV), which is connected between substrate and chamber walls, which helps to heat up the substrates by Ti^+ ion etching.

The combination of ion nitriding in DC discharge plus arc ion plating as a duplex substrate surface treatment method is possible. This configuration enables to use sputter cleaning of the substrates, oxide removal, ion nitriding and deposition of the coating in a single PVD unit [46].

Another approach is to separate the macro particles from ions and electrons by using a curved magnetic field. Axenov et al. and his co-workers first used such a filter. Since then, plasma transport through such filters has studied by various workers. An example of this is shown in Figure 1.4 b. Here a 90 ° bend or a quarter of a toroid is used. Cathode is at the end and the substrates are at a distance from the other end. The magnetic field is such that the diameter of the duct is much smaller than the ion gyro radius and much larger than electron gyro radius. In other words, the electrons are magnetized and the ions are not. Electrons spiral around

the field lines and go out. Ions follow the electrons to maintain plasma neutrality. The macro particles, even if they are charged, are not affected by the magnetic field, as they are too heavy. They travel in straight lines and hit the walls of the duct. The duct is designed such that it is optically blind so that macro particles cannot reach the substrates unless they are multiply reflected from the walls. Thus one can get almost macro particle free films. All the plasma generated at the cathode would not reach the exit of the duct. Some plasma is lost to the walls due to cross-field diffusion and various drifts caused by curved magnetic fields. Biasing the duct can increase transmission efficiency. Transmission efficiency can also be improved by increasing the magnetic field. However, beyond a certain field efficiency starts reducing due to the onset of instabilities in the plasma [47]. Filters come in various shapes and sizes [45, 48, 49,50]. They include S-shape filters [20] and off plane double bend filters [21]. Design objects are to eliminate macro particle flux and increase plasma transport efficiency. It depends on various factors like the diameter and other geometrical factors of the duct, magnetic field, bias on the duct, cathode material etc. The efficiency is specified by the system coefficient, which is as the ratio of the total ion current at the exit of the filter to the arc current. For unfiltered arcs this is usually in the range of 10% to 20%. For 90° filters a system coefficient of 2.5% has been achieved. About 0.6% is reported for a S-shape filter. Filtered arc have limited industrial use due to low deposition rates and restricted geometry make.

Review of cathode design and cathode spot control

There are many different types of cathodes designed over the past decades up to nowadays. The early commercial equipment had “frustum-cone” – type or “arched-field” – type non-rotating cathode [45], made of mostly one metal (e.g. Ti, Cr). Over the past 30 years scientists and engineers have developed technical solutions to control the speed and path of the arc spot, thus minimizing the generation of macroparticles and allowing to burn a low voltage arcs on composite targets [60].

Below, in Figure 1.6 are given some examples with explanations of improvements over the previous design shown in Figure 1.4 a. In Figure 1.6 a consumable cathode (Pos. 2 in) has an end face (Pos. 3) which differs from the design shown in Figure 1.4 a. In this design (Figure 1.6 a) an anode (Pos. 5) is placed inside the longitudinal axially-symmetrically aligned electromagnetic coil (Pos. 4). The number of turns per unit length of the electromagnetic coil is greater around the cathode than in the remaining proportion of the coil, moreover the coil extends beyond the ignition electrode (pos. 6 in Figure 1.6 a) at the side opposite to the working end face of the consumable cathode.

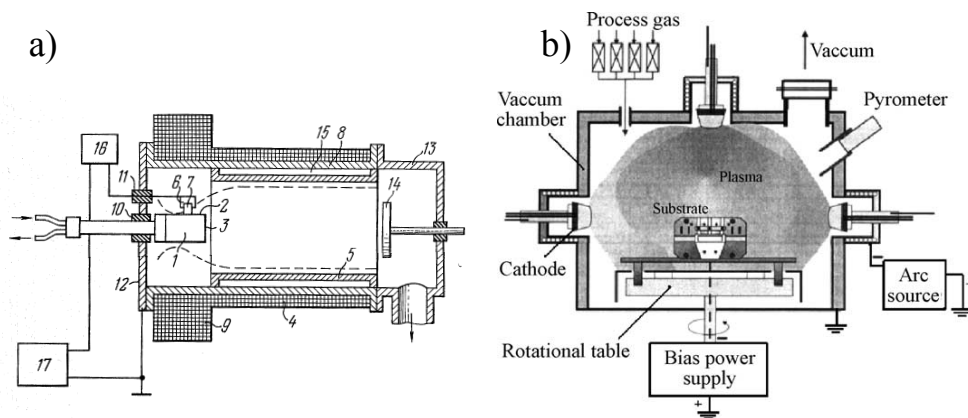


Figure 1.6. Arc evaporator from AIP unit „Bulat-6“: a - principle of having a "bottle necked" type magnetic field located behind the rear face of the cathode [33, 51], and b - schematic of an AIP unit “Bulat-6” [52].

Such an arrangement makes it possible to obtain a magnetic field whose maximum is shifted from the ignition electrode to the side opposite to the working end face. Therefore, in the process of operation the plasma flow generated by the cathode is injected into a longitudinal axially symmetrical magnetic field with a „plug“ beyond the working end face of the cathode. The plasma flow, not meeting a retarding potential barrier on its path, passes to the coil outlet without any obstacles. As a result, practically all ions generated by the cathode are transported without any losses to the outlet. Investigations have demonstrated that the above-considered way of stabilisation of the cathode spot is effective only in the case where the number of turns per unit length of the solenoid around the consumable cathode exceeds the number of turns per unit length in the remaining portion of the solenoid at least two times. The dotted lines shown in the Figure 1.6 a. are magnetic field lines obtained from the electromagnetic coil around the cathode and anode. Maximum magnetic field intensity of the coil is located in that portion thereof which is disposed close to the igniting electrode (striker) [33].

The detailed description of the start-up of the arc-evaporator is as follows:

- The power supply (Pos. 17 in Figure 1.6 a) for an arc discharge is switched on.
- The power supply for the solenoid (not shown in the Figure 1.6) is switched on and a magnetic field is obtained, whose lines of force are disposed as shown in the drawing by dotted lines.
- Maximum magnetic field intensity of the solenoid is located in that portion thereof which is disposed close to the igniting electrode.
- The ignition-pulse generator for ignition electrode (Pos. 16 in Figure 1.6 a) is switched on. A spark discharge over the ceramic jumper of the ignition

electrode is obtained. This small spark discharge forms a cathode spot of the arc discharge between the side surface of the cathode and the tubular anode.

- The cathode spot drifts towards the working end face of the cathode due to the fact that:
 - The arc where the cathode spot appears, the magnetic lines of force intersect the side surfaces of the cathode at acute angle directed towards to the working end of the cathode and moves to the working end face while accomplishing chaotic shifts.
 - Under the action of an electric field whose form of equipotentials is determined by the topography of a magnetic field, the generated plasma flow of the evaporised material of the consumable cathode is directed completely towards the substrate.
 - The plasma flow of the evaporised material of the cathode is transported along the tubular anode practically without any losses since the radial electric field prevents the drift of the ion component of plasma onto the walls of the tubular anode [1].

In general, those types of evaporators described above have cone-type cathodes made of material to be evaporated. The surface area of cathode is relatively small which causes the formation of large number of macroparticles. These designs employ a uniform erosion of the cathode front surface. In these cases only pure metals (as shown in Figure 1.7) were used to form plasma of an evaporative material.

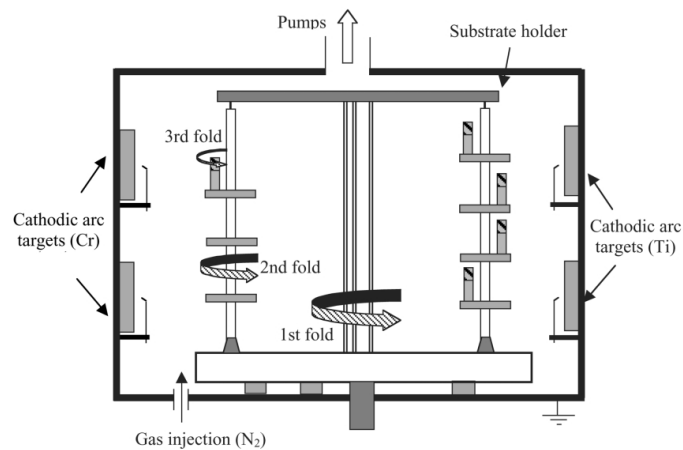


Figure 1.7. Schematic view of the coating unit including 4 arc cathodes and a threefold substrate holder [53, 54, 55, 56]

At about the same time with the designs described above [33, 44, 45, 46, 51] a method of a cathode having multiple layers of metals together was used (Figure 1.5). The cathode spot was retained on the working end of the consumable cathode with the help of a solenoid-generated magnetic field [17].

With the following patents [57, 58] dated from 1988 and 1989 accordingly, first time ever rotating cathodes with arc spot steering by magnetic fields generated by the combination of permanent and/or electromagnets locating inside the target [68, 69], were used in AIP technology.

Here, a short overview of the technological progress of rotating cathodes with magnetic arc steering feature is given in below. Previously, hollow cathodes with embedded magnets were used only in sputtering technology [59]. Hollow cylindrical cathode benefit from having considerably larger surface area than a planar cathode occupying the same space within a vacuum chamber. According to *Kuriyama et al.*, target (cathode) and anode are in the form of cylinders and a magnet is disposed in the cathode in such manner that the electro-magnetic force encloses the electrons in an electrode space to increase the electron density, thus resulting higher deposition rates (Figure 1.8).

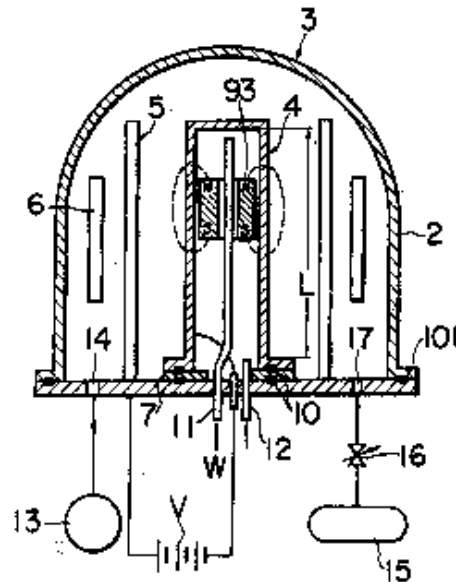


Figure 1.8. Sputtering device having movable permanent magnets inside the target providing even utilization of the target material and to obtain uniformity in thickness of a metallic film deposited on a workpiece [59].

The new technology was invented by *Veltrop et al.* and patented [57, 58] by Hauzer Holding B.V in 1988 (Figure 1.9 and Figure 1.10). Such technology enables precisely controlled helical path movement of the arc spot along the target surface (Figure 1.13). The magnetic field generating device (Pos. 8 in Figure 1.9) disposed into the cylindrical target (Pos. 3 in Figure 1.9) comprises an assembly of permanent magnets (Pos. 23 in Figure 1.10) or electromagnets or its combination. The intention of such arrangement is to keep the cathode spot in the desired area (Figure 1.9 b) of the target surface. By rotating the target it is possible to provide a

fresh target surface and target surface could be evenly eroded. It is also possible to rotate the magnetic field generating device along the surface of the target (Figure 1.10 b). If one wishes to run the cathode arc spot on this side, that faces the substrate holder, then the magnetic field generating device should be directed into substrate direction. If the arc spot is needed to run in an opposite direction of the target – the magnetic field generating device should be directed into this new desired direction. Such arrangement could be used to clean the target before the beginning of the deposition process of the adhesion layer. The drawback of this technology is that only a small part of the electrode is covered by magnetic field; under high currents the arc can penetrate into the area of low magnetic field intensity, which slows down the arc velocity resulting increased number of macroparticles [69].

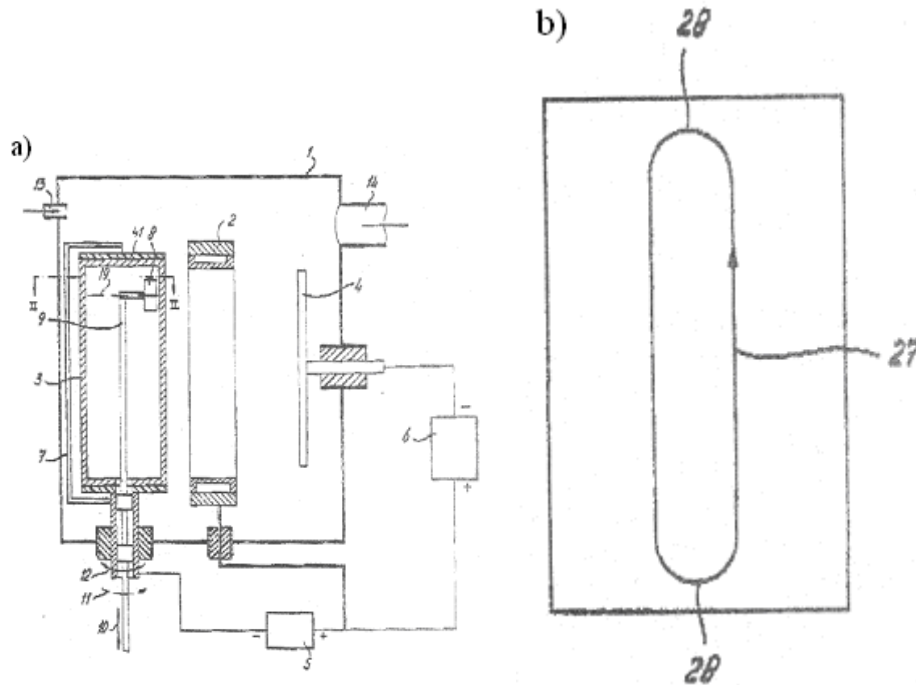


Figure 1.9. Cross-section view of the hollow cathode (3) and the surrounding anode (7) (a), and projection of the path of movement (retrograde movement) of the arc (27) (b) [57, 58].

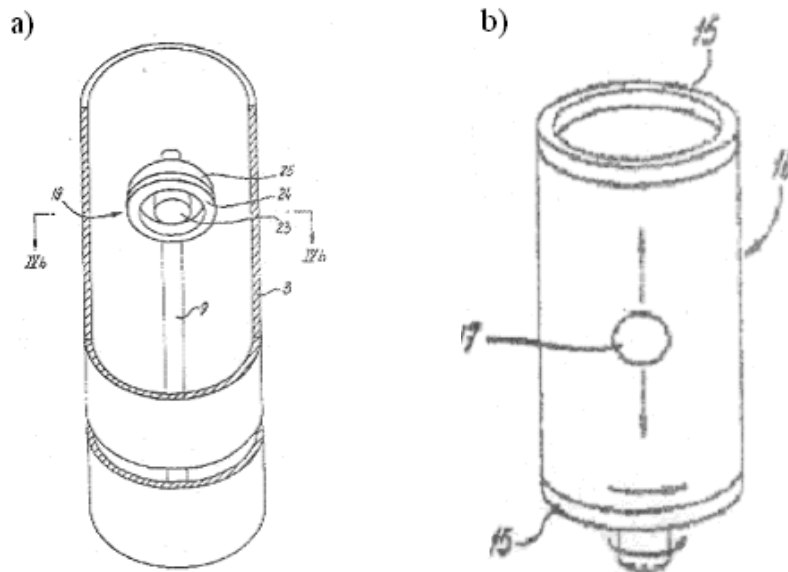


Figure 1.10. Cross section view of the rotating hollow cathode (3) with integrated magnetic field generating device (a) and view of the cathode showing the rotation of the cathode and reciprocating movement of the magnetic field generating assembly (b) [57, 58]

Another design [60] was invented by *Welty* and was patented by Vapour Technologies Inc. in 1993. This design uses axial magnetic field to force the motion of the arc into an open helical trajectory on the cathode surface.

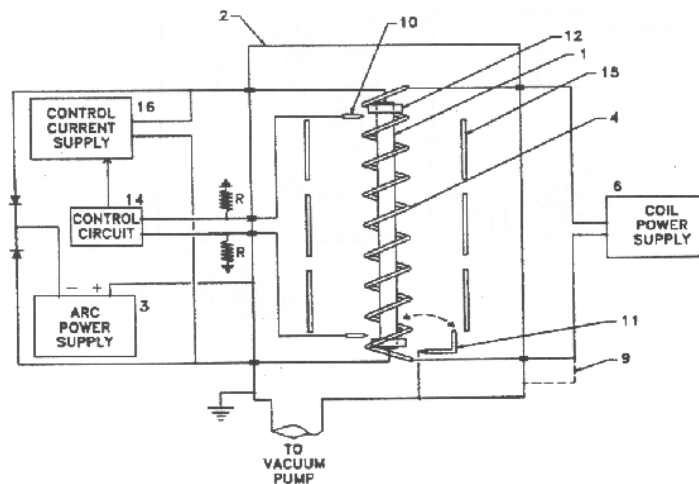


Figure 1.11. Schematic of the vacuum arc evaporation apparatus with control unit providing control over the speed and path of motion of an arc spot on the surface of the cathode [60].

The motion of the arc spot on a cylindrical surface could be described as a sum of circumferential and longitudinal movement of the arc spot on the cathode. The object of this invention is a method of superimposing following arc motions into desired arc movements:

- Applying an axial magnetic field component parallel to the cylindrical axis of the cathode via helical electromagnet coil (Pos. 4 in Figure 1.11) placed coaxially around the cathode. Electromagnet coil (solenoid) generates a magnetic field with flux lines parallel to the cathode axis i.e. axial magnetic field.
 - Axial magnetic field generates the arc motion around the circumference of the cylindrical cathode. Under the influence of axial magnetic field component, the arc rotates around the cathode as it travels down the length forming an open helix.
 - Increasing the field strength of the applied axial magnetic field increases the velocity i.e. speed of the arc spot movement i.e. speed around the circumference of the cylindrical cathode, thus reducing the macroparticle generation by reducing the amount of time the arc spends in each crater along its track.
- Circumferential magnetic field is a sum of self magnetic field due to the arc current flowing through the cathode to the arc spot, and an optional applied circumferential magnetic field due to the variable control current through the cathode that is supplied independently of the arc current.
 - Control of the strength of the circumferential magnetic field allows to control the speed of longitudinal arc spot movement by following methods:
 - An arc power supply is connected to both ends of the cathode simultaneously. The fraction of the arc current, which is supplied to each end of the cathode, while maintaining the total arc current constant between the cathode and anode. The net circumferential magnetic field component at the location of the arc spot along the cathode length will then be the function of the division of arc current between the two ends of the cathode. If the currents at both ends are balanced, the arc will rotate around the circumference (Figure 1.12 b) at an independently controllable speed due to the axial magnetic component caused to the helical solenoid (Figure 1.12 d) arranged co-axially with the cathode. If the currents are unbalanced, the arc will move along the length of the cathode toward the higher current end of the cathode [18] (Figure 1.12 a and

c), at speed proportional to the rate of imbalance in the current feed [60].

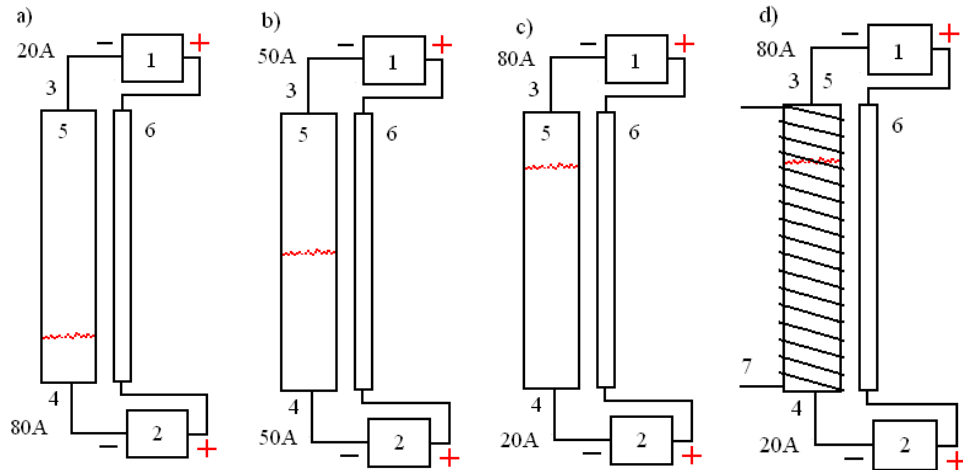


Figure 1.12. Vacuum arc evaporation apparatus where the rotational speed of the arc can be predetermined by the axial magnetic field created by the helical solenoid (Pos. 7) and the vertical position of the rotational arc spot can be positioned and scanned (the red line in the cathode surface imitates the arc spot track) from one end of the cathode to the other by the circumferential magnetic field, at speed independent of the total arc current, which can be held at constant [60].

- There is second method of controlling the circumferential magnetic field strength around the cathode, thus controlling the speed of the arc spot movement. Arc DC current power supply (Figure 1.14, Pos 1) is connected to both end of the cathode simultaneously, providing equal current flow to each end of the cathode. At this stage circumferential magnetic field is created over the cathode and the arc has no tendency to move along the length of the cathode due to the balanced current flow at both ends of the cathode. Then, both ends of the cathode are connected to another power supply (Figure 1.14, Pos 7) to pass a control current through the cathode from one end to another. By changing the polarity and magnitude of the current of the control power supply (Figure 1.14, Pos 7), one can force the arc to move in one direction or other along the length of the cathode. Since the control current power supply is not part of the cathode – anode circuit, changes in the magnitude or polarity of control current have no effect on the arc current that remains constant. This allows the increase of the circumferential magnetic field strength greater than it would have existed from the arc current alone. This allows the use increased arc velocity together with low arc currents and in presence of strong axial magnetic field component [60].



Figure 1.13. Photograph of the vacuum arc, rotating around the cathode due to the axial magnetic field generated by the helical solenoid [61].

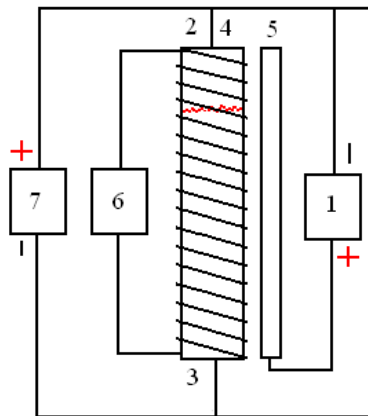


Figure 1.14. Vacuum arc evaporation apparatus according to *Welty* [60] having arc current flow balanced to both end of the cathodes, where the rotational speed of the arc can be changed by the axial magnetic field created by the helical solenoid that is feed from the coil power supply (Pos. 6). Magnitude and polarity of the circumferential magnetic field strength (position and speed of the arc longitudinal movement) can be changed separately from the cathode – anode assembly via separate control power supply (Pos. 7) directing control current through the cathode at desired direction (polarity) and magnitude (control current).

Another design [18] using similar basic concept dates from 1995 from Kharkov from *Sablev et al.*, *Andreev et al.* and his co-workers is presented in Figure 1.15. This design does not have a magnetic field generating solenoids, as in his earlier designs [1, 15, 16, 17, 19, 33, 34] to keep the arc in a front area of the planar cathode and protecting the arc from escaping to the side surfaces of the cathode. The cathode itself can be used as a current position transducer of the cathode arc spot and its power supply leads serve as the detector in this design [18].

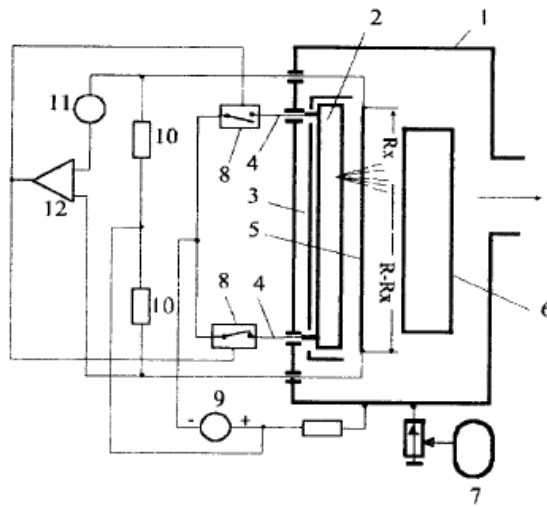


Figure 1.15. Extended planar cathode with magnetic arc steering in an AIP coating processing system [18, 62]

Above described technology is based on the metal arc evaporator in which the unit for determination of the cathode spot position on the cathode evaporation surface allows control of cathode spot movement according to a given program. Cathodes (Pos. 2 in Figure 1.15) having an extended shape and power supply leads (Pos. 4 in Figure 1.15) connected on the opposite sides of cathode; the cathode spot always extends towards the turned-on power supply lead. Reciprocation of the cathode spot can be accomplished by alternating the power supply leads by using control switches (Pos. 8, Figure 1.15). Arc discharge current passing through extended cathode generates a magnetic field the directions of which forces cathode spot to move in the direction of turned-on power supply lead [18]. The use of such system results in uniform coating over the whole surface of the substrate.

Japanese company Kabushiki Kaisha Kobe Seiko Sho from Kobe, have patented several similar solutions related to rotating arc cathodes and magnetic steering of vacuum arcs [63, 64, 65] in between 1998 and 1999. In [63] there is given a solution for a problem of water-cooled anode that is usually kept at low temperatures related to deposition process, that releases moisture etc. in a coating operation which influences the quality of the film the substrates. They propose to use a resistive heated anode that could be heated to high temperatures before the coating deposition process start to prevent exfoliation or separation of the condensed film on the anode during the coating deposition. In [64] a method of controlling the behaviour of arc spot movement even in a case of large arc discharge currents is described.

A relatively unique method of a combined PVD - PACVD technology is dated from 2000 from *Holubar* and *Jilek* from SHM S.R.O from Czech Republic [66,

67]. These patents include a method of producing coatings partly with AIP (CAE) technology by burning a low voltage arc on a rotating target (Pos. 2, Figure 1.16) made of pure metals or alloys (Figure 1.16) and partly by PACVD by using appropriate gases (TiCl_4 , CH_4 , $\text{B}_3\text{N}_3\text{H}_6$, SiH_4) suitable for the PACVD process, and gas ionisation with the aid of low voltage arc on the cathode. The apparatus also have arc spot magnetic steering feature with the aid of electromagnetic coils (Pos. 11 and 12 in Figure 1.16) for the arc spot positioning and by varying the intensity of the magnetic field strength of the coils, one can increase the arc spot movement speed and thus the increase the ionisation rate of the reactive gases for the PACVD process. Therefore, the plasma for the CVD process could be sustained with the ionisation generated by the low voltage arc instead of the glow discharge, which would have resulted irregularity of the coating growth. After all, combining CVD and PVD into a same chamber and sustaining the plasma for the CVD by glow discharge alone would cause intoxication of the non-operating cathode/cathodes. But, by sustaining the plasma for the CVD with the aid of low voltage arc (by evaporating metallic component for the coating), suppresses the intoxication of the cathode [66].

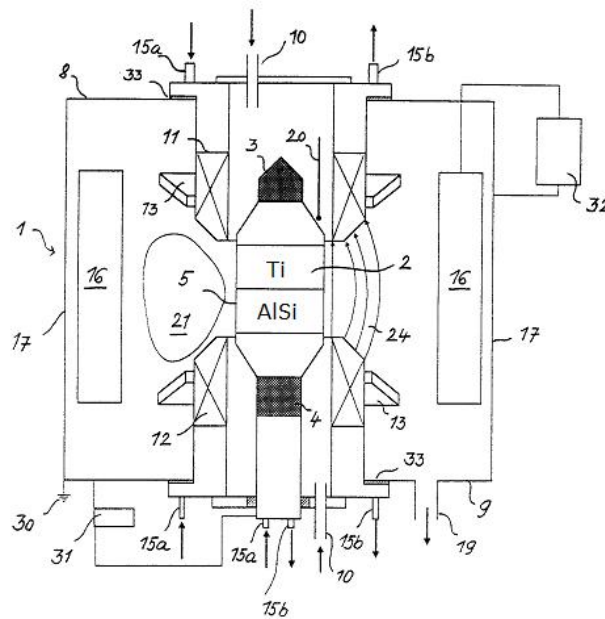


Figure 1.16. Combined PVD / PACVD vacuum coater comprising a rotating composite target [66, 67]

Another PVD technology achievement dates from 2002 from *Holubar, Jilek, Morstein* and *Cselle* from SHM S.R.O and Platit AG [68, 69]. The invention consists of at least one magnetic coil (Pos. 7a and 7b, Figure 1.17) or at least one permanent magnet inside each cathode (Pos. 2a and 2b, Figure 1.17). With such embodiment the surface of the cathode that is being evaporated will show uniform erosion (Pos. 11, Figure 1.17) that extends the life of the cathode considerably. Due

to the fact, that the length of the source of the magnetic field approximate equals the length of the hollow cathode, resulting acceptably small quantities of deposited macroparticles [68, 69].

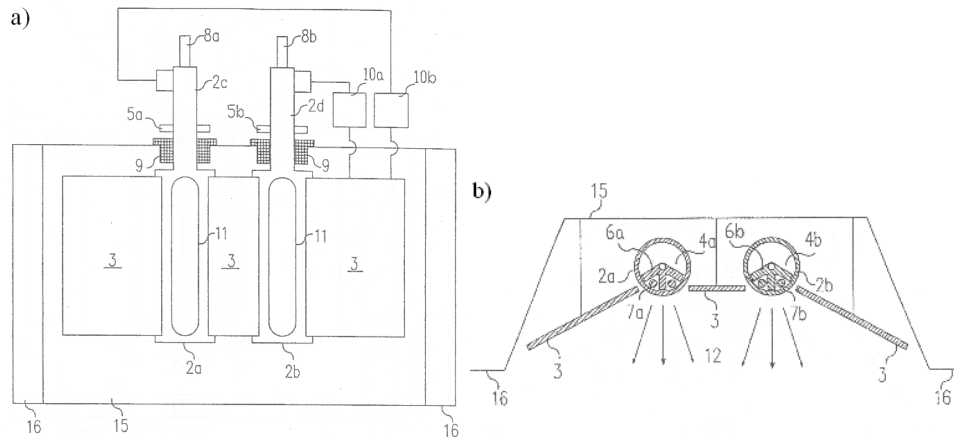
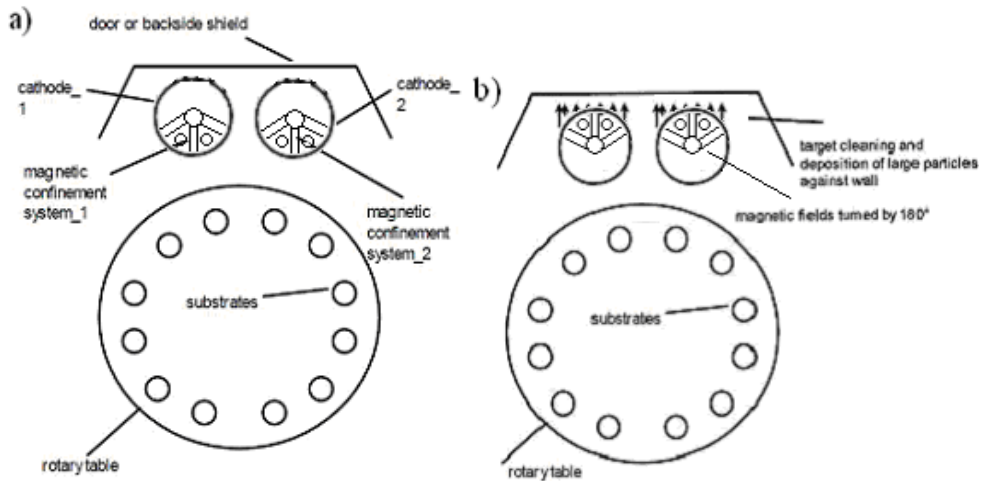


Figure 1.17. Low-voltage cathodic arc evaporation unit with magnetic field sources integrated into hollow cylindrical rotatable cathodes; a) front view, and b) top view [68, 69].

Here are given patents of rather similar PVD technology dated from 2004 and 2005 from *Morstein, Cselle, Jilek* and *Blösch* from PIVOT a.s. [70, 71].



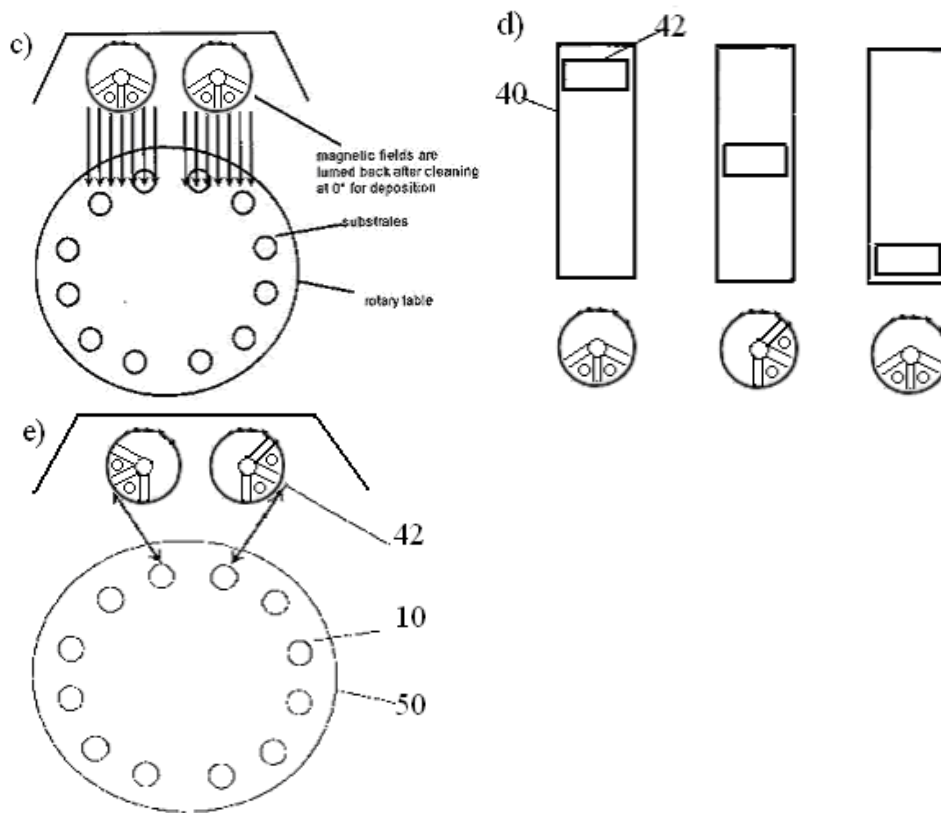


Figure 1.18. Schematic of low-voltage cathodic arc evaporation apparatus having two rotating cathodes with integrated magnetic field generating coils [69, 70].

These two above described patents (Figure 1.17 and Figure 1.18) include a method similar to that described above in Figure 1.16 with the main exception of having the coils embedded into the rotating cathode assembly and the magnetic source is being moved axially along the cathode (Figure 1.18 d) during the deposition of the coating. During heating of the substrates magnetic field sources are both aligned in the normal position (Figure 1.18 a). Prior the deposition of the substrates targets are cleaned by turning the magnetic field sources 180 degrees from the substrate as facing the chamber door inner surfaces (Figure 1.18 b). During the deposition of the substrate magnetic field sources are turned towards it (Figure 1.18 c). Magnetic field sources are turned approximately 45 degrees outwards while positioning in the middle of the cathode (Figure 1.18 d and e) [70, 71].

1.1.4 Ion nitriding, duplex coatings and duplex treatment

Heat treaters use a number of surface hardening processes to enhance the wear and fatigue resistance of metal components. Popular processes are carburising and nitriding. Conventional nitriding of workpieces is carried out in an atmosphere of partially dissociated ammonia or in a cyanide-cyanate salt bath, at temperatures of 650 – 850°C [77]. Ion nitriding is much more advanced method that gas nitriding benefiting with enhanced control of white layer, reduced distortion of the workpiece, processing time (usually 2 – 16 hours) [72, 73] and energy consumption [77], the workpiece surface is alloyed with nitrogen as result of a reaction caused by a high voltage glow discharge (Figure 1.19) between the metal work being processed (the cathode) and the vacuum chamber walls (the anode). An aspect of the DC glow discharge arc prevention is a function of operating parameters such as applied voltage, vacuum level (1 – 10 torr) [80] and gas mixture. Voltage (typically 700 – 1500 V) [73, 77, 80] from a controlled D.C. power supply energizes the substrate and the electrically isolated walls of the vacuum chamber. The resultant plasma (DC, RF or microwave discharge) [80] glow discharge (Figure 1.20) [80] is caused by the ionisation of hydrogen and nitrogen gas (positive ions strike the workpiece surface and electrons are emitted to the anode producing a glow discharge around the workpiece), which is bled into the vacuum chamber at a controlled rate. Gas ions bombard the workpiece being processed raising the temperature of the work piece to the 450 – 560 °C range – *i.e.* below the tempering temperature, resulting that the structure and mechanical properties remain almost completely unaffected [74] (also external heaters can be and are usually used) [73, 75, 77]. The photons released by this reaction create the blue-violet glow surrounding the work pieces. Positively charged hydrogen ions accelerate to the work at great velocity and act as a reducing and cleaning agent, removing oxides and small quantities of impurities from the surface. Under vacuum and glow discharge ions develop in nitrogen – hydrogen mixture. Under high – energy ion-bombardment Fe – atoms are sputtered from the surface that react with atomic nitrogen in the gas plasma and form unstable FeN. After depositing on the surface, FeN releases nitrogen to form lower order ion nitrides Fe₂N, ε-Fe₃N, γ-Fe₄N (Figure 1.21 and Figure 1.22). High – energy bombardment introduces vacancies and vacancy clusters on the metal surface that increases the diffusion process of nitrogen, resulting the formation of ion nitrides [72]. Nitrided case consists usually of compound layer (as shown in Figure 1.22) composes mainly of ε-Fe₃N, γ-Fe₄N iron nitrides; compound network that develops from the surface compound layer also called sub-surface layer, and diffusion zone [73]. The input of nitrogen atoms into the surface leads to the formation of compressive stresses in the nitrided region that increases the fatigue strength of tools. Also the H/E ratio is increased since hardness is increased considerably (a 50 – 200 μm thick nitride layer can reach hardness of up to 1200 HV0.05) [78] but elastic modulus remains practically constant [74]. The hardness, thickness and composition of these cases depend on the material being nitrided and the control of the following variables: time,

temperature, gas composition, pressure, voltage and current [36, 75, 76, 80] and ultimately the desired nitrated case. Processing time can vary between one hour and fifty hours depending on the type of alloy and the case depth requirement [36, 73, 75, 76, 77, 78, 79].

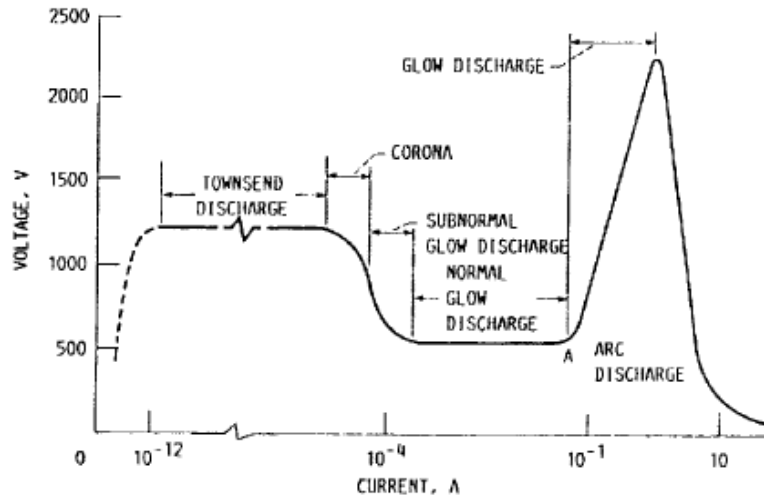


Figure 1.19. Voltage-current characteristics of different types of discharge in argon [80].

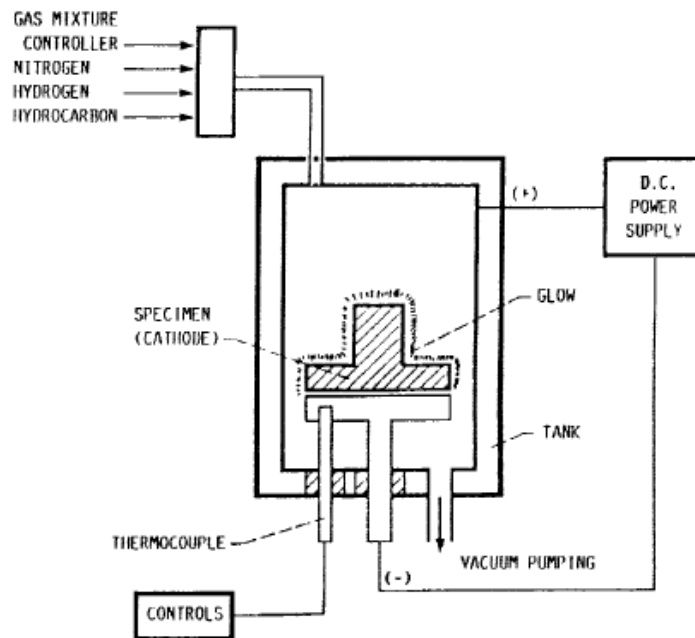


Figure 1.20. Schematic of ion-nitriding system [80].

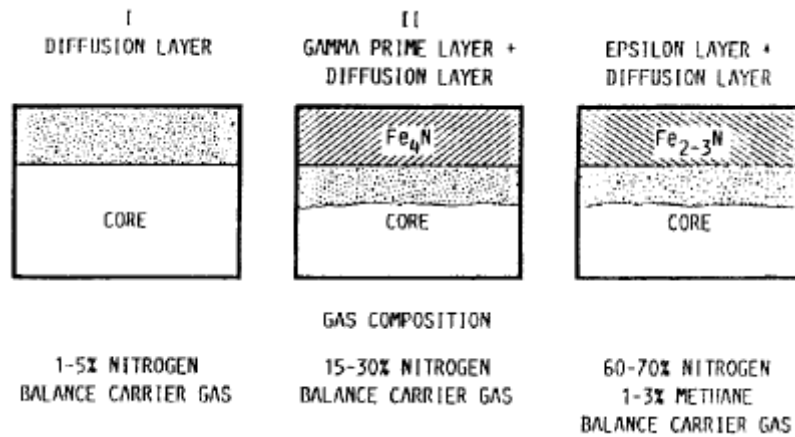


Figure 1.21. Metallurgical configuration during plasma nitriding [80].

PVD hard coatings are well – known for providing surfaces with enhanced tribological properties in terms of low friction and high wear resistance. However, their tribological performance is often limited by elastic and plastic deformation of the substrates, which can result in eventual coating failure. The development of duplex plasma treatments of surfaces offer enhanced properties to tooling by improving wear, fatigue and corrosion resistance and the load carrying capability of steel substrates [82]. Duplex treatment usually refers to combining nitriding heat treatment with the subsequent PVD coating [23, 37, 80, 81, 82, 83, 84, 90,].

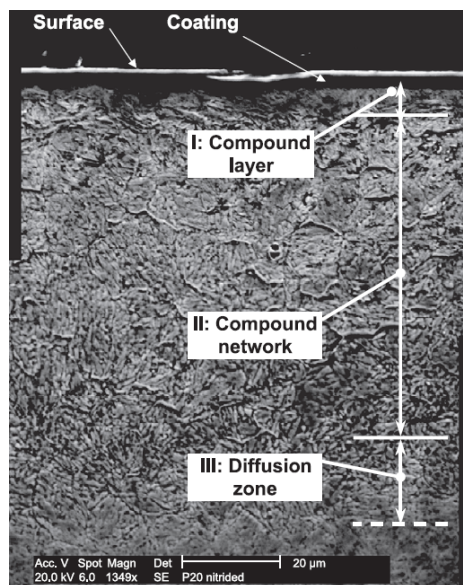


Figure 1.22. A SEM micrograph showing the cross-section microstructure of nitrided case formed on P20 cold work steel [73].

1.2 Process/microstructure/property relationship

The properties of advanced coatings are frequently determined by the microstructure, which in turn is developed during processing. In this connection, the processing/microstructure/properties relation is the focus of many research works. The hardness and thickness of coatings produced by different coating deposition methods is given below (Figure 1.23) representing the importance of selecting the appropriate coating technology for different applications.

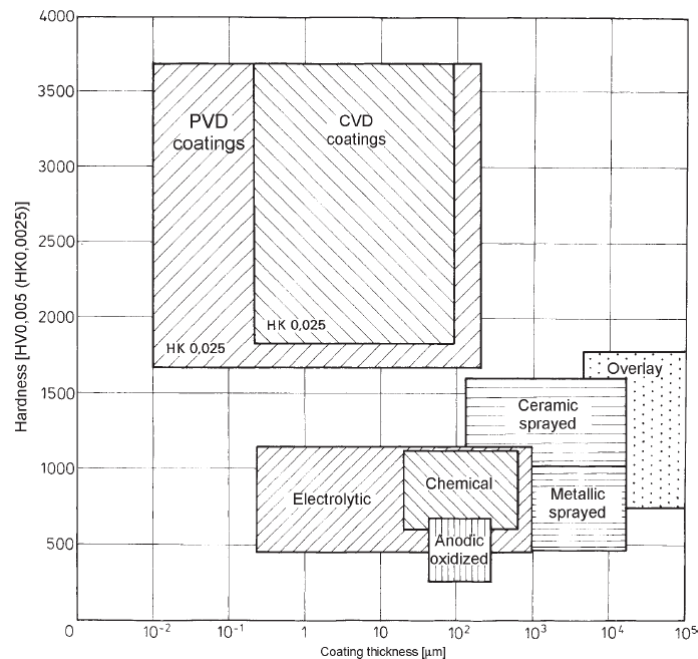


Figure 1.23. Ranges of thickness and hardness of some coatings [85].

1.2.1 Thornton-Messier structure zone diagram

Thornton–Messier structure-zone diagrams [22] have been proposed to correlate the microstructure of thin films with deposition parameters. One of the main parameters of the structure-zone diagrams is homologous temperature (T_s/T_m), defined as the ratio of the substrate deposition temperature (T_s , K) to the melting point of thin film material (T_m). The substrate temperature plays a key role in determining the ad atom surface mobility and the bulk diffusion rates.

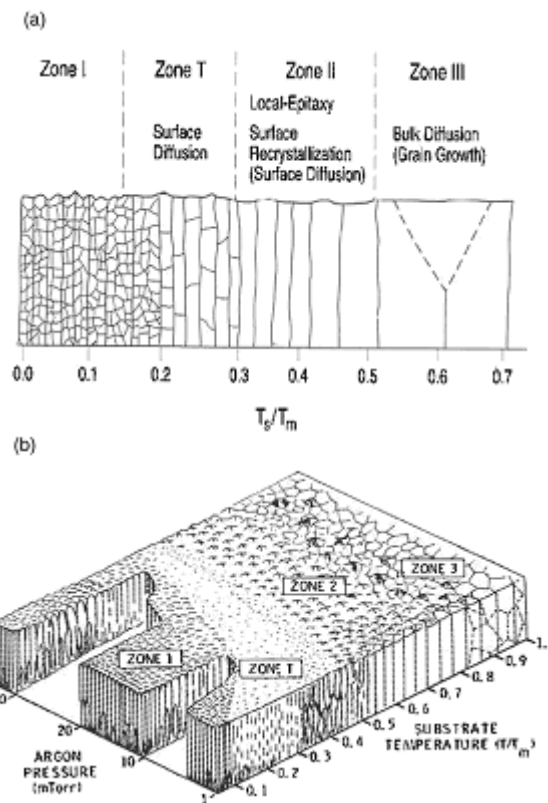


Figure 1.24. Structure zone diagrams for PVD coatings: a – *Grovenor*; b – *Thorton* [22].

Table 1.1. Classified microstructures of the four zones according to their homologous temperatures (T_s/T_m)

Zone type		<i>Grovenor et al.</i>	<i>Thorton</i>
I	0 – 0.15	Equiaxed “granular” fine grains with grain diameters in the range 5–20 nm resulted from a high nucleation rate and a low grain growth rate. The mobility of the deposited atoms is low at lower substrate temperatures.	Columnar structure with pronounced pores and open columnar boundaries. This structure is promoted by a high working gas pressure or a low homologous temperature.
T	0.15 – 0.30	Transitional microstructure between Zone I and the columnar Zone II. The adatoms can migrate via surface diffusion driven by the higher substrate temperatures.	Dense arrays of fibrous grains. Surface diffusion of adatoms are enhanced by increased substrate temperatures. A reduction in sputtering gas pressure during deposition increases the mean free path for elastic collisions

			between coating species and the sputtering gas atoms, thus leading to higher kinetic energy of coating species impinging on the substrate surface, thereby producing relatively dense microstructures.
II	0.30 – 0.50	Columnar structure, resulting from deposited atoms having sufficient surface mobility to diffuse and to increase the grain size.	Columnar structure, grains are separated by distinct boundaries.
III	> 0.50	Grain growth is controlled by bulk diffusion, as the substrate temperatures are higher than $0.5T_m$	Bulk diffusion of adatoms predominates

Grovenor et al. examined the microstructure of metal films grown by thermal evaporation [22]. They classified the microstructures into four zones according to their homologous temperatures as depicted in Figure 1.24 a. and in Table 1.1. *Thorton* incorporated an additional parameter, the sputtering gas pressure in the structure-zone diagram (Figure 1.24 b). *Messier* replaced the sputtering gas pressure of structure-zone diagram with the bombardment energy. Though the combined *Thorton–Messier* diagram can successfully predict the microstructures of deposited thin films in many cases, the effects of ion bombardment rate such as ion/metal flux ratio are not considered or incorporated. The bombardment rate should be considered to be just as important as the bombardment energy during film deposition.

1.2.2 Mono -, multilayer, gradient and nanostructured coatings

Coatings deposited by PVD techniques can be divided into two groups:

- *Simple*, known as *monolayer* or *single layered* coatings, comprising one material - a metal (e.g., Al, Cr, Mo, Cu, Ag, Au) or a phase (e.g., TiN, TiC) [85]. For many years this was the approach used to find coatings related solutions to specific application problem. In addition to the use of single component materials we have seen that improved tribological properties can be achieved by adding into the coating elements of other materials to produce a doped or composite coating [90].
- *Complex*, comprising more than one material (metal, phase or compound), with the materials distributed in a varied manner relative to each other [85].

Several types of *complex* coatings are listed below:

- *Alloyed* (multi-component) coatings in which the sub-lattice of one metallic element is partially filled by another metallic element. There are over 600 compounds known involving carbon and nitrogen with transition metals, including the best researched compounds as solutions of nitrides: TiN, VN, ZrN, NbN, TaN, WN, CrN and MoN with TiC, VC, ZrC, NbC, and TaC. Best-researched and featuring best tribological properties are the TiCN and TiAlN [85].
- *Multi-phase* coatings constitute a mixture of two or more divisible phases, e.g. TiN/Ti₂N or TiC/TiN [85].
- *Composite* coatings comprise a mixture of two or more phases and are specific type of multi-phase coating in which one phase is discretely dispersed in another phase, occurring in a continuous manner e.g., Ti/Al₂O₃ [85].
- *Multi-layer* coatings, also known as *microlaminates* [85] offer a wide range of possibilities to further improve the tribological properties of surface coatings. These comprise simple layers of different materials, deposited on top of one another with different properties. By changing the relative concentration of non-metallic elements in a coating composition produce a change in mechanical and physical properties. An example of a multi-layer coating TiC/TiCN/TiN [85].
- *Nanolayer* coatings, also known as *superlattice coatings* offer a range of possibilities to further improve the tribological properties of coatings. *Nanolayered* coatings are considered as coatings with layer period thickness of less than 100 nm.
- *Gradient* coatings are a type of multicomponent coating in which the chemical composition, properties of individual layers occurs in a continuous manner and structural morphologies continuously change when moving from the substrate to the surface. This gives the possibility to vary the properties of the coating at different depths from the surface. An example of a gradient coating is TiN/TiCN, TiN/TiCN/TiC [85, 90].
- *Nanocomposite* coatings are coatings with structural features, like the grain size, with dimensions below 100 nm. Such coatings can be achieved by controlling deposition parameters when mutually insoluble phases are simultaneously deposited or by subsequent heat treatment. The yield strength, hardness and toughness of polycrystalline materials all generally improve with decreasing grain size. A similar phenomenon seems to be valid for thin coatings down to nanometre size grains. In addition to mechanical properties, nanocrystalline materials can exhibit higher thermal expansion, lower thermal conductivity, and unique optical, magnetic and electronic properties. Nanocomposite hard coatings may be formed by a nitride-forming transition metal and a metal component or another compound, which is not dissolved in the nitride. In a second class of

nanocomposite coatings the nitride crystallites are embedded in an amorphous phase of another compound [85, 90].

Many of the gradient layer coatings mentioned above, and even some coatings classified as nanocomposites, are in fact multilayers. This may arise due to the nature of the deposition process, involving, for example, planetary rotation of components past a series of vapor sources. There are three main reasons why it may be advantageous to use layered coatings:

1. Interface layers. These are increasingly used to improve the adhesion of a coating to the substrate and to ensure a smooth transition from coating properties to substrate properties at the coating/ substrate boundary [85, 90].
2. Large number of repeated layers. By depositing several thin layers with various mechanical properties on each other the stress concentration in the surface region and the conditions for crack propagation can be improved [85, 90].
3. Diverse property layers. The properties of the surface can be improved by depositing layers of coatings that separately have different kinds of effects on the surface, such as corrosion protection, wear protection, thermal isolation, electrical conductivity, diffusion barrier and adhesion to the substrate [85, 90].

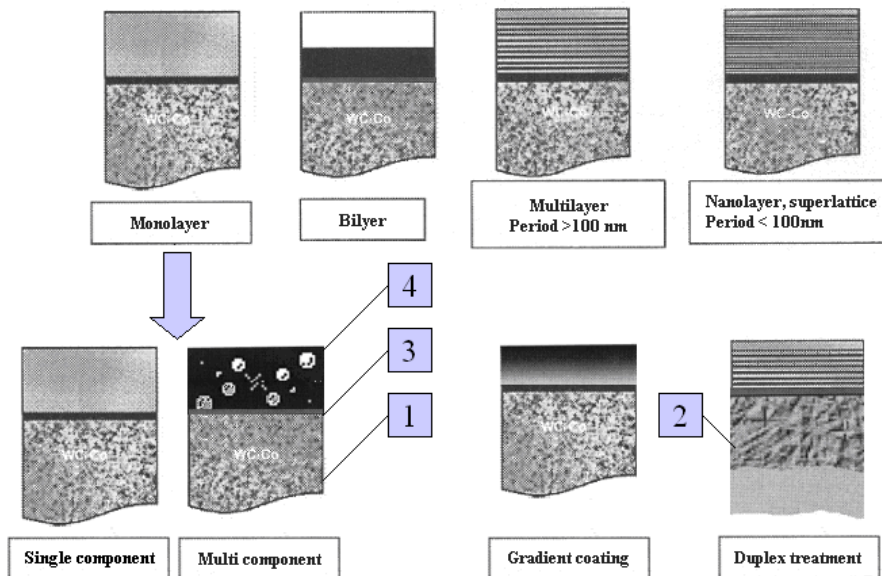


Figure 1.25. Different structures of tribological PVD coatings [86]: 1 – substrate; 2 – nitrided, carbonised, carbonitrided or laser treated zone of the substrate; 3 – adhesion layer; 4 – PVD coating

The plasma-assisted PVD process is most suitable for the production of both multilayer and multicomponent coatings because of its high flexibility in terms of materials, which can be deposited. With this process surface layers can be formed from any desired metal or metal-based component, and the coating can be deposited on virtually any substrate [85, 90].

1.2.3 Residual stresses

Residual stresses are present in most surface coatings and play a considerable significance in various applications, since they may influence characteristics such as wear resistance, fatigue crack propagation and damage development [108]. Residual stresses arise due to the grain growth behaviour during coating deposition (intrinsic stresses), lattice mismatch epitaxial film growth and phase transformations [87]. In addition thermal stresses arise during cool down from the deposition temperature due to the differences in thermal expansion of constituent materials. For all types of coating, the main sources of residual stresses are (a) differential thermal contraction and (b) phenomena occurring during deposition. It is common for these to be referred to respectively as extrinsic and intrinsic stresses [88]. The residual stress level is highly dependent on the manufacturing process of the coatings. In thin coatings, usually very high stresses develop. The presence of residual stresses may promote debonding and spallation of the coating. This becomes increasingly likely as the thickness of the coating is increased. [88]. The presence of residual stresses can be beneficial or lead to a failure of the coating – high compressive stresses in the coating prevent initiation of surface cracks or may cause cracking, delamination because of the poor bonding between the layers. Therefore accurate measurement and prediction of the residual stresses is vital in avoiding cracking and delamination of the coating [108].

1.2.4 Surface roughness

The surface parameter used to evaluate surface roughness, in this study, is the roughness average, R_a . This parameter is also known as the arithmetic mean roughness value, arithmetic average (AA) or centreline average (CLA). R_a is recognized universally as the most common international parameter of roughness (ISO 4287, 1997 standard). The average roughness (R_a) is the area between the roughness profile and its centreline, or the integral of the absolute value of the roughness profile height over the evaluation length (Figure 1.26.). Therefore, the R_a is specified by the following equation [89]:

$$R_a = \frac{1}{L} \int_0^L |Y(x)| dx \quad (1.1)$$

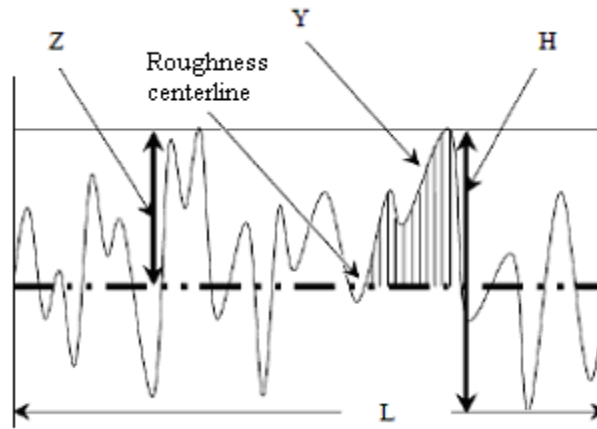


Figure 1.26. Surface roughness profile [89].

1.3 Friction and wear properties of coatings

Because the PVD coatings of interest are developed mostly for tooling, a brief overview about friction and wear in general, and about wear resistance and surface fatigue in particular are given below.

1.3.1 Friction

Friction is the resistance to motion, which is experienced when one body moves tangentially over another with which it is in contact. Thus friction is not a material property; it is a system response in the form of a reaction force. The coefficient of friction, μ , is the tangential frictional force F divided by the normal load w on the contact:

$$\mu = \frac{F}{w} \quad (1.2)$$

Basically friction can be divided in two components, an adhesion force, F_a , due to adhesion between the two surfaces, and a deformation force, F_d , due to deformation of the surfaces so that:

$$F = F_a + F_d \quad (1.3)$$

The deformation force is called ‘ploughing friction’ when it takes place on a macroscale and ‘asperity deformation’ when it takes place on a microscale.

The effect of friction can be divided into three basic mechanisms, one due to asperity deformation, one due to adhesion and one due to particle ploughing as shown in Figure 1.27.

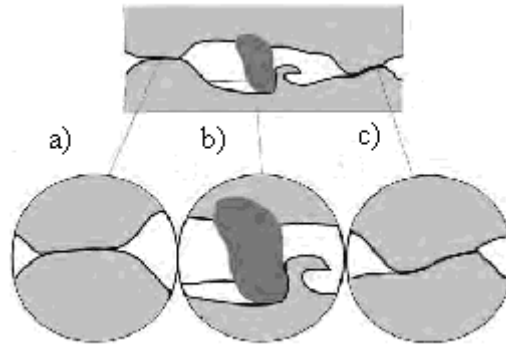


Figure 1.27. Three components of sliding friction; a – adhesion; b – ploughing; c – asperity deformation [90].

Sliding friction

The development of new surface deposition techniques, especially PVD and CVD and their combinations, has made it possible to produce surface structures and contact systems with extremely low friction. The measured values of the coefficient of friction for carbon and molybdenum disulphide-based coated surfaces have been about 50 times lower than what has earlier been achieved in dry sliding.

Rolling friction

We have so far considered friction mechanisms only in relation to the sliding of one surface over another. In the case of rolling, the coefficient of friction is normally smaller. The general considerations in relation to contact mechanisms are also valid for rolling contacts, but, because of the difference in contact kinematics, other contact effects dominate the frictional behaviour.

The main contributions to friction in rolling contacts are:

- micro-slip effects within the contact area,
- elastic hysteresis of the contacting materials,
- plastic deformation of the materials, and
- adhesion effects in the contact.

The contact mechanics for rolling are certainly complex but fairly well understood on a macroscopic level.

1.3.2 Wear mechanisms

Tribology, which focuses in friction, wear and lubrication of interacting surfaces in relative motion, is a field of science defined in 1967 by committee of the OECD [91]. Wear is the major cause of material wastage and loss of mechanical performance and any reduction in wear can result in considerable savings.

Wear is commonly defined as the removal of material from solid surfaces as a result of one contacting surface moving over another. Thus both friction and wear are simultaneously the results of the same tribological contact process that takes place between two moving surfaces.

A wear mechanism is a classification of the process by which material is removed from the contact surface. Typical wear mechanisms are adhesive, abrasive, fatigue and chemical wear. It is very common that in a real contact more than one wear mechanism is acting at the same time. The precise combination of wear mechanisms depends on the contact conditions and will result in a specific type of wear.

A wear mode is a classification of the type of contact, which is characterized by a specific kind of movement, geometry or environment. Examples of wear modes are sliding wear, rolling wear, fretting, erosion, impact wear and cavitation [90].

Adhesion

Adhesion is very serious forms of wear characterized by high wear rates and large unstable friction coefficients. When asperities of one surface come into contact with asperities of the counter surface they may adhere strongly to each other and form asperity junctions as shown in Figure 1.28. Relative tangential motion of the surfaces causes separation in the bulk of the softer asperities and material is removed. Transfer features of the removed material can greatly modify the sliding characteristics promoting the suppressing wear. In adhesive wear the surface material properties, atmosphere, as well as possible protecting surface films or contaminants, play important roles [90].

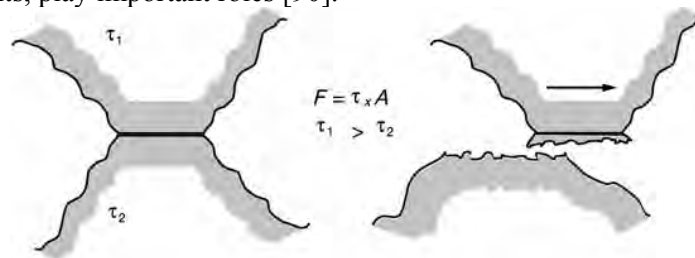


Figure 1.28. The basic mechanism of adhesive wear [90].

Abrasion

Abrasion is wear mechanism by plastic deformation as shown in Figure 1.29. Abrasive wear occurs in contacts where one of the surfaces is considerably harder than the other or where hard particles are introduced into the contact. The harder surface asperities are pressed into the softer surface, which results in plastic flow of the softer material around the hard one. When the harder surface moves tangentially, ploughing and removal of softer material takes place resulting in grooves or scratches in the surface.

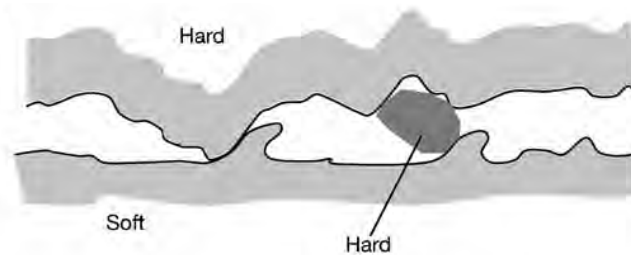


Figure 1.29. The basic mechanism of abrasive wear [90].

Depending on the geometry of the harder surface and the degree of penetration, the removal of material can take different forms, such as ploughing, wedge formation or cutting. Wear modes such as gouging abrasion, grinding abrasion and erosion abrasion can be distinguished.

Erosion

Erosion can appear in various forms: erosion by cavitation in pipes, water lines and pipelines; erosion by solid ash particles impact (Figure 1.30) in boilers, and in solid fuel operated gas turbines etc. Erosion is also known as a method of processing of materials (cleaning of castings and house facades, etc.). In this thesis erosion caused by impacts of solid particles is studied [92].

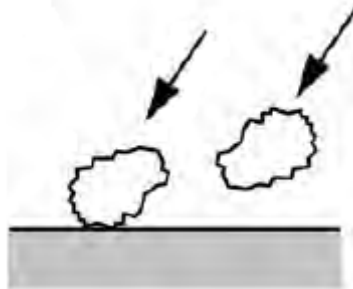


Figure 1.30. The basic mechanism of erosion wear by impact of solid particles [90].

Fatigue

Fatigue crack growth is now a well-documented phenomenon which results from loading and unloading of a surface, at a stress level in the material that it can sustain once but not if repeated many times. Fatigue can form the origin for large-scale cracking and liberation of surface material to form wear debris as shown in Figure 1.31.

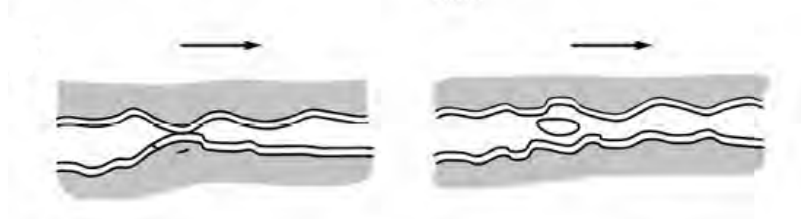


Figure 1.31. The basic mechanism of fatigue wear [90].

Pitting and spalling are wear failure modes in which the fatigue wear mechanism dominates. Surface fatigue or surface fatigue wear is caused by deformations of asperities and surface layers at sliding interface. Contacts between asperities during sliding are accompanied by repeated high local stresses causing fatigue cracks initiation, propagation and fracture [90]. The process of debris formation by fatigue wear is described in [93]. The main elements of coating fatigue response as for brittle materials are microstructure and residual stresses. Fine and homogeneous material structures are characterized by slow crack growth [93].

Oxidation

In chemical wear the wear process is dominated by detrimental chemical reactions in the contact, initiated by the influence of the environment, in combination with mechanical contact mechanisms as shown in Figure 1.32.



Figure 1.32. The basic mechanism of chemical wear [90].

Oxidation wear is the most common chemical wear process. A thin layer of oxides will be formed on the top of metal surfaces. This is an important protecting layer because without it both the friction and wear in metal contacts would be extremely high. If this layer is continuously removed by a rubbing action, and the formation of new layers is speeded up by a high humidity environment that can easily reach the contact, the result is a typical oxidation wear.

1.4 Application areas of hard PVD coatings

The application of TiN coatings made by PVD methods started with cold-forming tools and twist drills at the end of '70s [37]. The typical fields of applications of different coatings are as follows: cutting, punching and forming tools, moulding tools, machine and automotive parts, decorative coatings, and biomedical applications.

In cutting and turning tools applications, PVD technology is widely used to coat HSS and cermet tools (inserts, drills etc.). Worn tools are usually re-grinded and recoated thereafter again. Chemical removal of the coatings prior a new coating deposition is used as well. PVD coatings reduce the flank wear of turning inserts resulting longer tool life [37, 90]. Some PVD coatings have increased thermal and oxidation stability over TiN enabling higher cutting speeds and reduced cutting fluid (provides cooling and lubrication features) use. The temperature in the tool – workpiece contact can reach as high as 900 to 1300 °C when cutting steel [90]. PVD coatings help to reduce a significant part of the total machining cost by reducing machine downtime during replacement and reduce the costs for regrinding and resetting worn tools [90].

In punching and forming tools application the use of PVD coatings gained much attention with the invention of CrN and TiCN coatings in addition to TiN and CVD treatment. The tribological situation is typically characterized by high surface pressures, low deformation velocities, sometimes high temperatures, and, depending on the lubrication, a variety of different friction conditions [90]. Composite treatment (also known as duplex treatment and duplex coatings) of highly loaded tools can give better performance than PVD coating alone [37].

In moulding tools and tools for plastic moulding both TiN and CrN are used successfully [37]. Often, higher corrosion resistance is required in case of plastic moulds.

In case of the tool application only tool needs to be protected with wear resistant coatings, but in case of machine parts, both components are often to be protected from wear, high temperatures and corrosion. Successful applications of PVD coatings are: pump elements (plungers) of high-pressure diesel and gasoline fuel injection pumps; injection nozzles of fuel injectors; highly loaded gears, transmission parts, gear selection forks; automotive valve elements (face, stem, seats, cam followers, valve lifters, cam lobes); piston rings, piston pins, cylinder inner surfaces, crankshaft journals, shell and ball bearing surfaces; EGR parts, turbine shaft journals of turbochargers; motorcycle and mountain bike front damper (fork) sliding surfaces.

The use of PVD coatings in decorative applications provides also increased abrasive resistance besides the desired decorative appearance. In some cases an increased corrosion resistance is achieved as well [37]. The field of applications is wide, covering watches, knives, scissors, spectacle frames and architectural elements (e.g., church decorative roofs) [37].

Hard PVD coatings are widely used in dental and surgical tools (scissors) and in orthopaedic implants as (hip stems) [37]. Total hip joint replacements are the largest field of tribological implants. Hip replacements are used in the case of either osteoarthritis or hip fracture. In the 1980s there were 120,000 total hip joint replacement surgeries per year and in 2006 the number had increased to about one million [90]. A healthy human joint has a remarkable lifetime of typically 75 years with more than 1 million loading cycles per year. The lifetime of hip joint replacements is about 10 to 15 years, and some 12% of patients require second replacements. There is currently an urgent need to extend the treatment to patients under 50 years who would require replacements to last at least 20 to 50 years. There are three main factors which limit this: (a) insufficient wear resistance, (b) loosening of the stem to hip caused by wear particles or (c) cement-to-bone interface failure or implant-to-bone interface failure [90].

1.5 Conclusions to the chapter and aims of the study

PVD technology, being an environmentally friendly has gained a well-known worldwide reputation in these years. Due to the steadily growing demand of the increase in tool lifetime, cutting speed and oxidation resistance in processing alloys and composites – new coatings and surface treatment technologies are to be developed to replace the state of the art TiN PVD coatings. However, many new PVD coatings are yet available for at least two decades now.

Other generations of hard coatings as multi- and nanolayers, gradient, superlattice and nanocomposite coatings were introduced along with the development of new high strength alloys, powder steels and composites; high speed CNC machines and industrial robots; new requirements for gas turbine engines (compressor and turbine blades) to resist abrasive wear caused by the impact of high velocity impinging abrasive particles; limitations in usage of cooling liquids in machining and increased demand for the time that it takes to replace the tool in CNC machining centre or in a multi position dye in fine blanking i.e. increased tool life. However, the evaluation of promising thin, nanostructured and gradient coating is of high importance due to their advantage concerning economic prospects as well as environmental impacts [94].

The usage of hard PVD coatings has gained much acknowledgement as a way to remarkably improve tribological and corrosion resistance properties of the material as new high performance coatings have higher hardness; better wear resistance;

lower surface roughness; lower coefficient of friction, higher fatigue and oxidation resistance. However, their application is restricted by the possibility of plastic deformation of the substrate [82, 83, 84], as the coatings themselves are very thin, and the load to be carried by the substrate.

Therefore, the importance of the selection of appropriate substrate material and heat treatment, coating material with its unique physical and chemical properties for particular application is crucial. Various PVD coatings differ from adhesion; hardness; coefficient of friction; state and magnitude of residual stresses; resistance to erosive, abrasive, impact and fatigue wear. Although introduced more than two decades ago, TiN still dominates among the hard coatings employed in the industry. Despite the many numbers of new PVD coatings and coating systems introduced in the last decade there are only few published works of cracking, fatigue, erosion, abrasion and impact resistance of PVD coatings. Thus to suppress wear and cracking in metal cutting and forming tools by the application of the coating, the wear and cracking mechanism must be determined.

Despite the numerous studies that have been carried out by other authors in the field of Ti and Al-based nitride and carbonitride PVD coatings such as TiN, TiCN, (TiAl)N, (AlTi)N having mono-, multilayer, gradient or nanocomposite design, relatively moderate attention has been paid to duplex coatings and duplex treatment techniques of PVD coatings. Plasma-nitriding exhibits characteristic advantages, being environmentally clean, and allowing an efficient low-temperature processing of materials for which only a certain maximum temperature is allowed, e.g. in order to avoid the formation of undesired phases for low tempering steels, due to the activation in the glow discharge plasma. For a large variety of different tool and machine components, a longstanding experience with plasma-nitriding has been acquired in mostly small companies, with successful applications mostly for conventional tool steels. The surface hardness of the tools can be increased by a factor of 2 – 3 [95]. The behaviour of PVD coatings under erosive, abrasive and impact wear conditions; fatigue and the cracking resistance of PVD coatings are important parameters for the design of tools of the metal sheet forming. Therefore, the present research is focused on the design and characterization of coatings that can be used in tooling.

The main objectives of the study are:

- study of different coating systems and coatings design to find the relationship between surface interface and tribological properties;
- optimisation of technological parameters of PVD technology for production of coatings with determined properties (recommendations for improvement of hard coatings properties);
- to elaborate the selection criteria for hard coatings for tooling – at different areas of metal processing (stamping, machining, moulding).

Activities planned to achieve the main goals of the study:

- study different systems “substrate-coating” (hardmetal – coating, HSS – coating, nitrided steel – coating) and coatings design (nano – and multilayer, gradient and nanostructured coatings);
- study of the microstructure and surface properties (hardness, roughness);
- study of the interface “substrate – coatings parameters (adhesion, cracking resistance, fatigue, residual stresses);
- study of the tribological properties of coatings (wear resistance, CoF);
- study of the technology for optimisation of tribological parameters and coatings design;
- application of different coatings at various conditions of exploitation;

2 EXPERIMENTAL

2.1 Studied systems

Hard PVD coatings on different steel and hardmetal substrates

The PVD coatings studied in the present work were produced in the Laboratory of PVD Coatings at TUT. Platit π -80 arc-ion plating PVD unit was used for deposition of hard coatings. Unit has two rotating cathodes embedded into the door (Platit patented LARC[®] - Lateral Arc Rotating Cathodes technology) of the vacuum chamber. All coatings were deposited using two of three cathodes available – Ti and Al or AlSi (18 wt% Si). Vacuum chamber has a usable volume of 80 litres in total (Figure 2.1).



Figure 2.1. PLATIT π - 80 coating unit featuring cylindrical, rotating cathode LARC[®] technology.

Duplex treatment of nitriding steel substrates

Duplex treatment is a process combining surface hardening (e.g. heat treatment, ion implantation or thermo-chemical treatment) and subsequent deposition of hard PVD coating. The nitriding process consists of a complex mechanism of reactive diffusion leading to the formation Fe_4N and Fe_3N compounds at the surface. Nitriding steel 38CrMoAl8 specimens with dimensions of $D = 27 \text{ mm}$, $h = 3 \text{ mm}$, were used for duplex treatment. Plasma nitriding process was performed in

Bodycote Lämpökäsittely Oy in Finland. Plasma nitriding was conducted at temperature of 500 – 520 °C. Process was specified to achieve surface hardness minimum of 1000 HV0.2 and minimum case depth of the specimens of 0.2 mm. Subsequent deposition of hard coatings was performed in the Laboratory of PVD Coatings at TUT.

Laser treatment of substrates

To increase the loading capacity of coated surface, different pre- and after-treatments of the substrate (as laser treatment) were applied. Laser beam treatment was performed using the Haas HL4006D 4 kW Nd:YAG laser with the wavelength of 1064 nm. The laser was operated in the continues wave mode, the dimensions of the laser spot were set as 4 x 9 mm. Treatment zone was shielded with argon at the flow rate of 20 l/min.

2.1.1 Studied substrates and coatings

High performance powder metallurgical (PM) cold work tool steel (CWTS) – Vanadis 6 and highly alloyed spray formed (SF) – Weartec™ produced by Uddeholm as well as nitriding steels and cermets were used as substrates for coatings deposition. Specimens with size of 20 x 20 x 5 mm plates were heat treated and prepared for the deposition of PVD hard coatings. After grinding and diamond suspension polishing (suspension diamond grain size 1 µm) all samples were degreased ultrasonically in phosphate-alkali solution, rinsed in ethanol and dried in air. The chemical compositions and hardness of tool steels are listed in Table 2.1 and Table 2.2.

Table 2.1. Chemical composition of the substrate materials investigated.

Substrate	Chemical composition, wt%									
	Ti	WC	Co	Other carbides	C	Si	Mn	Cr	Mo	Others
Vanadis 6	-	-	-	-	2.1	1.0	0.4	6.8	1.5	5.4 V
Weartec™	-	-	-	-	2.8	0.8	0.7	7	2.3	8.9 V
38CrMoAl8	-	-	-	-	0.38	0.4	0.4	2.0	2.0	1.65 Al
H10 (WC-Co)	-	89.5	10.0	0,5 TiC	-	-	-	-	-	-
H15 (WC-Co)	-	84.5	15.0	0.5 TiC	-	-	-	-	-	-
T70/14 (TiC-FeNiSi)	-	-	-	70	-	0.45	-	-	-	25.35 Fe 4.2 Ni

Table 2.2. Main mechanical properties of the studied substrates.

Substrate	Type	Young's modulus E, GPa	Hardness	Poisson ratio	Surface roughness, Ra, μm
Vanadis 6	PM CWTS	210	64 HRC 843 HV0.01	0.28	0.51 \pm 0.10
Weartec™	SF CWTS	199	64 HRC 843 HV0.01	0.28	0.51 \pm 0.10
38CrMoAl8	Nitriding steel	250 – 300	850 HV0.01	0.28	0.51 \pm 0.10
H10	WC-10Co, average grain size $d_g=0.5 \mu\text{m}$	590	1555 HV0.3	0.23	0.2 and 0.05
H15	WC-15Co, average grain size $d_g=2.0 \mu\text{m}$	590	1170 HV0.3	0.23	0.2
T70/14	70TiC-30 (Fe14Ni1.5Si) average grain size $d_g=2.2 \mu\text{m}$	410	1270 HV0.3	0.23	0.2

Five different PVD coatings among them monolayer, multiplayer, gradient – TiN, TiCN, TiAlN, AlTiN and nanocomposite coating nACo® (nc-(Al_{1-x}Ti_xN)/a-Si₃N₄) are studied.

2.1.2 Sampling

The samples for the present study were prepared in Laboratory of PVD Coatings at TUT and Uppsala University, Angstrom Laboratory, Sweden. Primary mechanical processing of substrates included cutting into specimens of required size with Struers cutting machine, samples for coating deposition were encapsulated into plastic using hot mounting machine Struers Prestopress- 3 and polished using Struers Pedemax-2 apparatus including last stage of polishing by 1 μm diamond suspension.

2.2 Characterisation of studied systems

2.2.1 Characterisation of microstructure

Coating thickness

The thickness of the coatings was determined using a BAQ calotester (spherical cap grinder) KaloMax® and by the image analysis of cross-sections using Nikon

Microphot-FX optical microscope and digital imaging and image analysis system Buehler Omnimet 3.0.

The meticulous measurements of the spherical gap diameter in perpendicular directions were carried out, followed by averaging. The statistical sample size was equal to 10 for each type of the experiment, i.e. for the fixed ball speed and grinding period.

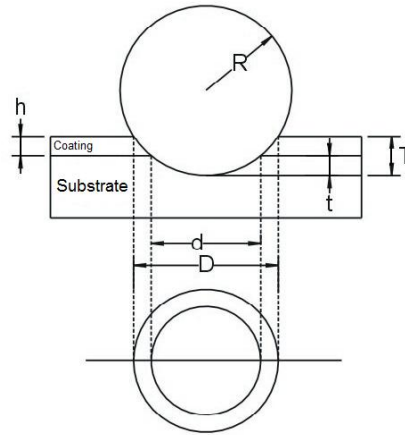


Figure 2.2. Measurement principle of spherical cap grinder: h – desired layer thickness, R – radius of the grinding ball, T – total penetration depth of the ball, t – depth of penetration in the base material, D – diameter of the spherical cap at the surface of the sample, d – diameter of the limit between coating and base material.

The total penetration depth of the grinding ball amounts to:

$$T = R - \sqrt{R^2 - \frac{D^2}{4}} \quad (2.1)$$

The depth of penetration in the base material is:

$$t = R - \sqrt{R^2 - \frac{d^2}{4}} \quad (2.2)$$

The thickness of the layer results from the difference:

$$h = T - t; \quad h = \sqrt{R^2 - \frac{d^2}{4}} - \sqrt{R^2 - \frac{D^2}{4}} \quad (2.3)$$

Microstructure characterisation

Cross-sections of PVD coated specimens; being dipped into a bowl filled with liquid nitrogen for few minutes; were fractured then and used to study the microstructure by the optical microscope and scanning electron microscope (SEM).

Energy Dispersive X-ray Spectroscopy (EDS) provided rapid quantitative analysis of elemental composition within the specimen of depth of 5 – 9 μm .

Surface roughness

Optical interferometer microscope Wyko NT-2000 from Veeco Instruments Inc. was used to evaluate the surface roughness of the coated specimens. The Wyko NT-2000 measures surface heights from 0.1 nm to several mm with a roughness measurement resolution better than 1 \AA . Innovative template software facilitates customized head analysis, without time-consuming set-up (Figure 2.3).

The coatings and substrate materials surface roughness were measured by profilometer Perthometer Concept from Mahr GmbH. The coatings mechanical properties (nanohardness and elastic modulus) were obtained by using MTS Nano Indenter XP® and Micromaterials Nano Test system pendulum-type nanohardness tester. The nanoindentation was performed in a depth mode, a target depth of 150 nm was chosen. A standard Berkovich indenter with tip radius of 100–200 nm was used for all experiments. The thickness of coatings was constant and measured by BAQ calotester KaloMax®.

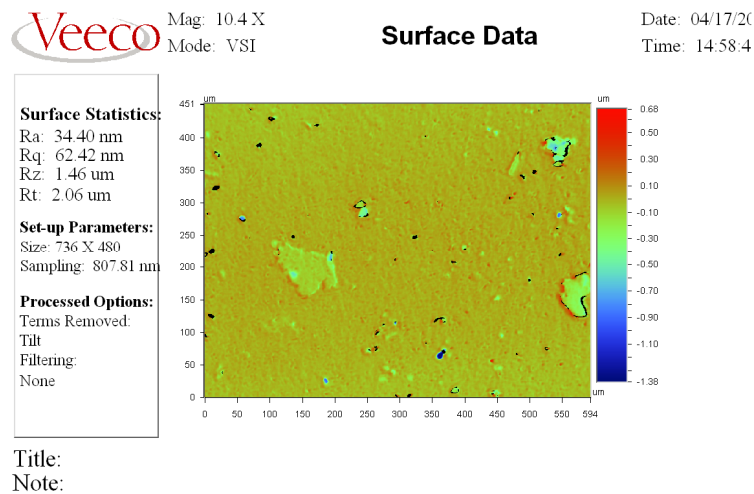


Figure 2.3. Veeco processed image of surface roughness of TiN surface.

Hardness measurement

Hardness measurements of the substrates were carried out using the microhardness tester Micromet 2001. Microhardness values of the substrates were measured using the Vickers pyramid indentation method at 0.1 – 3 N (0.01 – 0.3 kgf) load. Specimens were polished to a mirror finish before the measurement.

Nanohardness measurements of the coatings were carried out using MTS Nano Indenter XP[®] (Uppsala University, Ångström Laboratory, Sweden) nano-indentation system (Figure 2.4) with standard Berkovich indenter having tip radius of 100–200 nm. Fused silica (quartz – SiO₂) was used as a standard material in nanoindentation calibration tests because it has very high purity and extremely homogeneous distribution of mechanical properties. For each specimen, a matrix of 5 x 4 indentations were produced. Indentations with different depths were necessary, but after several trials a target indentation depth of 150 nm was chosen as giving most confident values, hence being deep enough to be free from the influence of the roughness profile, being below the 10% coating thickness depth, hence free from substrate influences [134]. Chosen indentation depth resulted an average indentation load of 9 – 15 mN, being dependant on the nanohardness of the coatings. After the load vs. depth data was collected, the resulting curves were first visually observed, and some problematic indents due to absence of microdroplets on the surface and due to the various extrinsic process parameters, such as external vibrations or fluctuations in the input voltage etc., were removed. Once the indentation cycle was completed and the corresponding load vs. depth data was logged, the raw data was analysed by the computer program to determine the hardness and modulus values.

Comparison test were conducted on pendulum-type nanohardness Micromaterials Nano Test platform at TTU using also a standard Berkovich indenter having tip radius of 100–200 nm [134]. Indentations of 1, 5, 10, 20, 30, 50, 75, 150 and 300 mN were performed on the sample. The initial load was 0.03 mN, and then the indentation load was applied as a ramp that reached the full load in 20 s. After a 10-s dwell time, the load was relieved in another 20 s. For each load, seven different locations were indented [134].



Figure 2.4. The nanoindentation platform that was used to evaluate nanohardness of selected PVD coatings at Uppsala University.

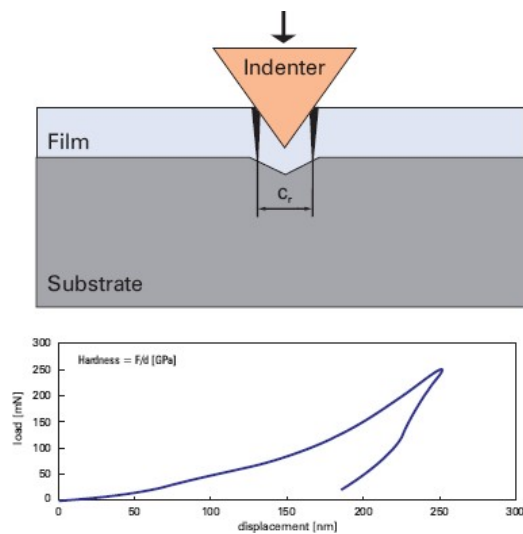


Figure 2.5. Representative image of an indenting principle and graph.

2.2.2 Characterisation of “substrate – coating” system properties

For study of adhesion two tests methods (Scratch test and Rockwell “C” test) were used

Scratch test

Adhesion is the best parameter for a measure of the chemical bonding across the interface. However, most adhesion tests do not measure this basic adhesion but produce a practical adhesion measurement conflating basic adhesion with other factors, which can be specific to a given material pair or test method [101]. However, scratch test method is widely used by the coating industry and coating development laboratories, as well as in research for evaluating the adhesion properties of coatings [99].

The scratch test consists of pulling a rigid diamond indenter over the surface of a sample under a normal force, which is increased either stepwise or continuously until failure is observed, as shown in Figure 2.7 [96, 97, 98, 99, 100, 101, 102]. It is generally accepted that the test is suitable for coatings of thickness ranging from 0.1 to 20 μm . The rigid diamond indenter (stylus) has Rockwell C geometry with a 120° cone and a 200 μm radius spherical tip defined in the EN 10109-2. Indentation loading rate of 0 – 100 N/min and the indenter transverse speed of 10 mm/min was used [101]. The scratch test procedure is described in the suggestion prEN 1071-3 [96]. The material loading and response conditions have been divided into three independent phases as shown in Figure 2.6 [96].

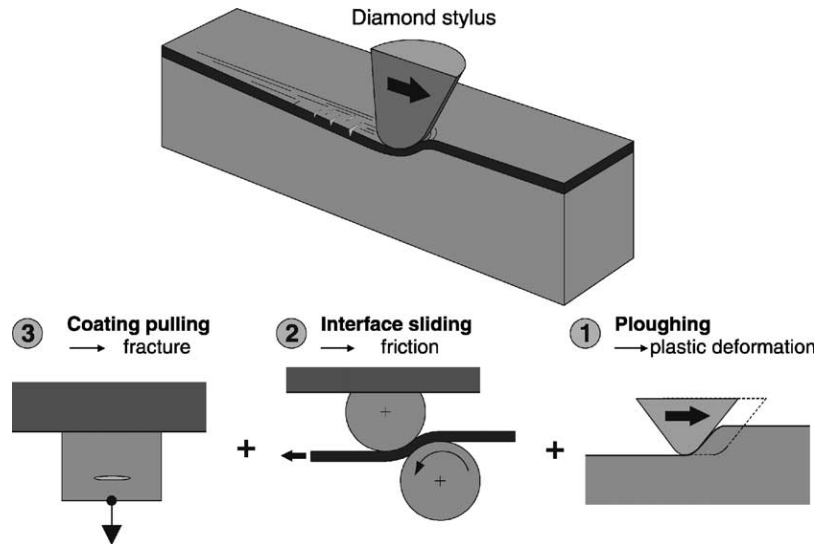


Figure 2.6. Schematic illustration of the indenter drawn along the coated sample showing the loading and response phases as follows: 1 – ploughing; 2 – interface sliding; and 3 – pulling a freestanding coating [96].

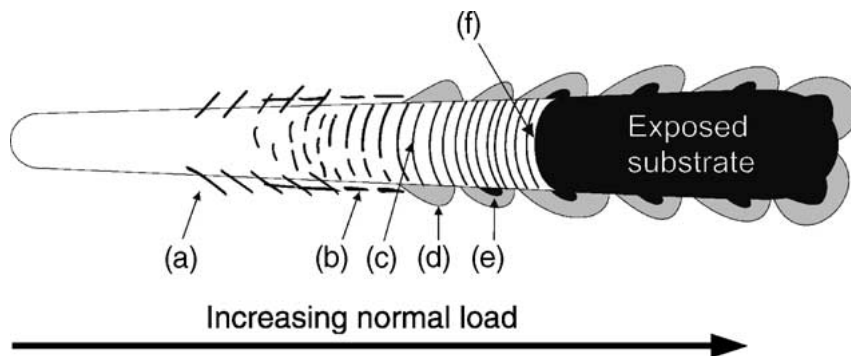


Figure 2.7. Schematic illustration of surface cracks generated during scratch test [93, 96].

The surface cracks generated in a scratch test track (Figure 2.7) can be classified as (a) angular (forward and transverse) Chevron cracks at the border of scratch track (Lc1), (b) parallel cracks (Lc1), (c) transverse semi-circular cracks (Lc1), (d) coating cohesive chipping (buckling) at the track edges (Lc2), (e) coating spallation at the track edges (Lc3), and (f) coating breakthrough spallation [96, 97].

In the normal configuration of the test a rigid diamond stylus is drawn across the coated surface under an increasing load until some well-defined failure occurs at a load, which is often termed the critical load, L_c [96, 97, 98, 99, 101]. Generally,

critical load L_c is a load at which a failure mode first occurs; delaminations increase almost linearly with coating thickness [100].

The adhesion related failures [100, 101], which are the basis of the scratch adhesion test for hard coatings are:

- Cracking (Lc1) - angular type (Chevron cracks) cracks in forward and transverse direction, parallel cracks at the border of scratch track and transverse semi-circular cracks in the bottom of the scratch track.
- Cohesive chipping *i.e.* buckling (Lc2) at the track edges of the coating
- Spallation (Lc3) of the coating at the track edges and gross interfacial shell-shaped spallation from the bottom of the scratch track.

In buckling, failure occurs in response to the compressive stresses generated ahead of the moving indenter as shown in Figure 2.6, phase 1. Localised regions containing interfacial defects allow the coating to buckle in response to the stresses and individual buckles will then spread laterally by the propagation of an interfacial crack (Lc1) [101, 102]. Buckling failures (Lc2) typically appear as curved cracks or patches of damage extending to the edge of the scratch track or beyond. They are often delineated by considerable coating fragmentation and have major crack planes perpendicular to the coating/substrate interface. In most cases buckles form in the region of plastic pile-up ahead of the moving indenter.

In spallation, failure occurs when through-thickness cracks form in regions of high tensile stress within the coating. Once the buckle (Lc2) has occurred the scratch stylus passes over the failed region crushing the coating into the surface of the scratch track formed in the substrate. Coating removal (Lc3) can be enhanced at this point or the failure may disappear completely depending on its size and the toughness of the coating [101].

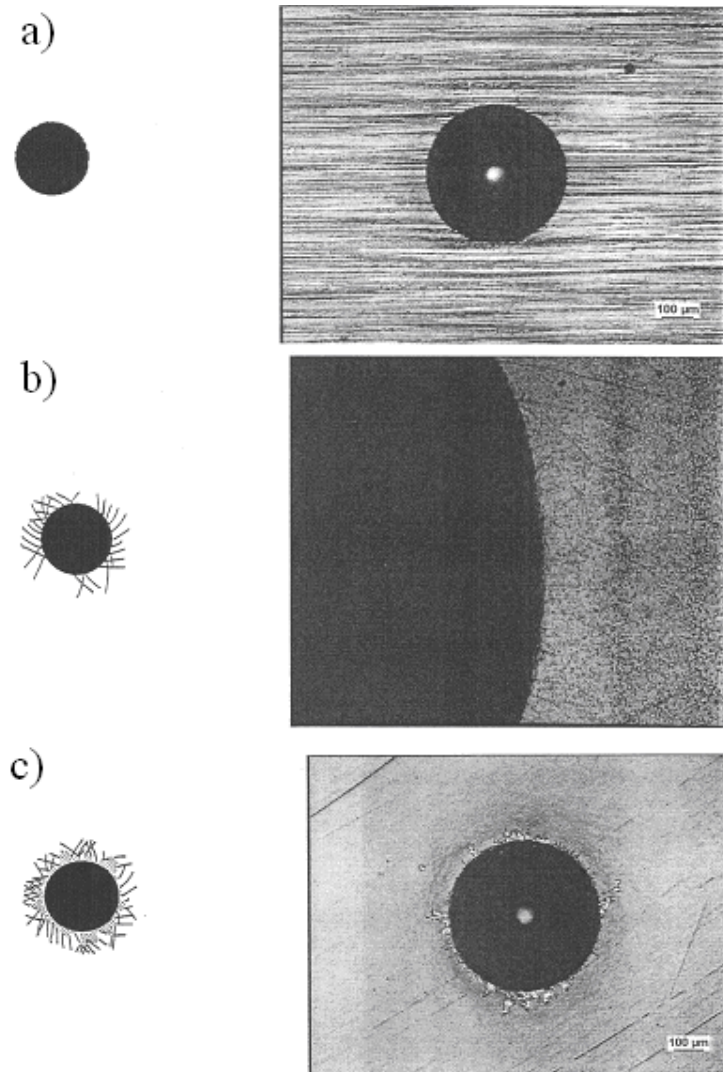
Rockwell “C” test

A well-known Rockwell adhesion test (Rockwell “C” indentation test) method was used in order to verify the adhesion quality of the coatings, [103, 104]. The test procedures are described elsewhere [103, 104] and follows the EN ISO 6508-1 and VDI 3198 (1992) standard. Sample surfaces were free from dust, oil, and other contaminations. Tests were performed on Zwick/ZHR 8150. A load of 1471 N (150 kgf) *i.e.* Rockwell C scale, were used in order to conform to the relevant standards [103, 104]. A conical diamond indenter with a 120° tip angle penetrates into the surface of a coated specimen inducing severe plastic deformation to the substrate and fracture (cracking, chipping, debonding) of the coating. Each sample was indented at four different representative locations as a minimum. Indentations were made in a direction perpendicular to the specimen surface. The indented samples were then analysed with an optical microscope at a magnification of 100 X and 500 X and results were classified into the categories given in the CEN/TS 1071-8

standards [103] as shown in Table 2.3. A pictorial representation and sample photographs of these classes can be found in Figure 2.8.

Table 2.3. Classes and observation of results of Rockwell indentation test.

Class	Observation
Class 0	no cracks nor adhesive delamination
Class 1	cracking without adhesive delamination of the coating
Class 2	partial adhesive delamination with or without cracking
Class 3	complete adhesive delamination



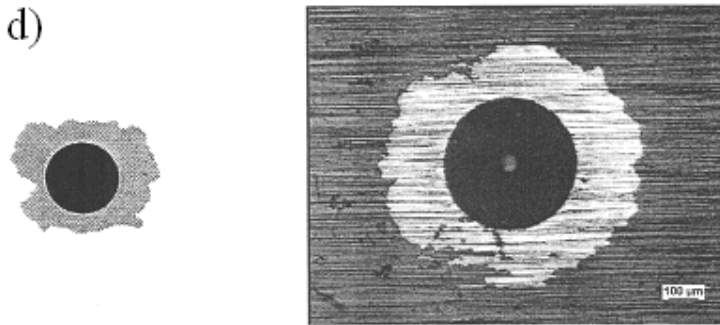


Figure 2.8. Pictorial representations and sample photos of classified cracks: a – class 0, exposing any cracks or adhesive delamination of the coating; b – class 1, exposing cracking without adhesive delamination of the coating; c – class 2, exposing partial adhesive delamination with or without cracking; d – class 3, exposing complete adhesive delamination of the coating.

Cracking resistance

An indentation at a single point method (Figure 2.9) was used to evaluate the cracking of the coatings. In the indentation experiment Vickers diamond indenter pyramid and Instron 8800 servo-hydraulic fatigue test system were exploited (Figure 2.10). The number of indentation cycles varied from 1 up to 10 000 and total indenting load of 500 N (mean compressive load of 275 N, alternating load 225 N) was applied with stress ratio $R = 0.1$, sinusoidal loading pattern and loading frequency of 0.5 – 15 Hz was applied. The optical microscope Axiovert 25 (Zeiss) with magnifications of 100 X and 500 X and Buehler Omnimet Image Analysis System 5.40 including the package for crack length measurement (Palmqvist method, [105]) was used.

The qualitative criteria's (from 0 to VI – from weak cracks formation, propagation to delamination of the coating) of coatings' cracking evaluation (Table 2.4) was considered and examined by optical microscopy and SEM investigations. The increase of the average length of radial cracks at the corners of the indenter impression depending on the number of indentation cycles was offered as a quantitative analysis criterion for coatings cracking resistance assessment.

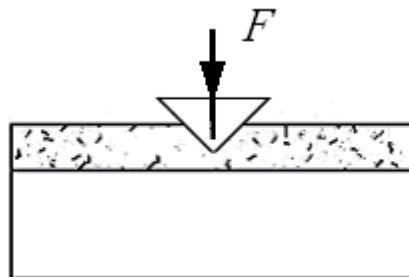
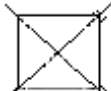
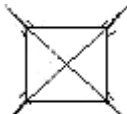
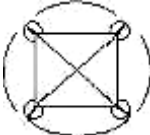
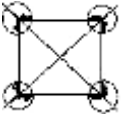


Figure 2.9. Schematic of single point surface fatigue testing principle.

Table 2.4. Crack types and crack evaluation criteria.

Evaluation criteria	Crack type	Crack type description
0		Very weak secondary radial cracks, which emanate from the edge and around the corners of the imprint.
I		Weak secondary radial cracks.
II		Medium secondary radial cracks and weak radial cracks – beginning of radial cracks formation.
III		Medium secondary radial cracks and medium radial cracks – propagation of weak radial cracks.
IV		Medium secondary radial cracks and strong radial cracks.
V		Medium radial cracks, delamination of coating in the corners of the contact impression and cone (ring) cracks at the periphery of the imprint.
VI		Strong radial cracks and delamination of the coating around the corners of the indent impression.

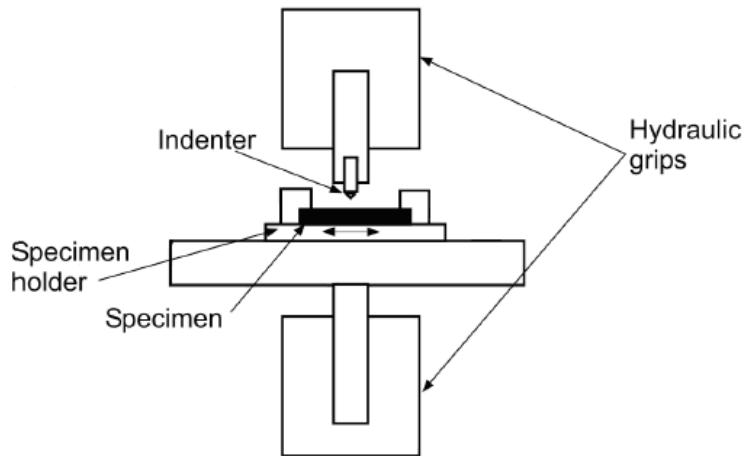


Figure 2.10. The schematic of impact tester.

Residual stresses

The AIP method means to make high energy state with accelerated Ti, Al, C, or N ions with non-equilibrium state, and deposited on the substrate material. Ti, Al, C or N ions were attracted to the substrate by an effect of bias voltage. Attractive forces can be amplified by increasing the bias voltage that is considered to be the major factor affecting the residual stresses [106]. Macroscopic residual stresses σ of the coatings was evaluated using curvature measurement method. The curvature method uses known Stoney equation [107, 108, 109, 110, 111, 112, 113] (Eq 2.4) and applies in cases where the thickness ratio of the thickness of the coating (h_1) to that of the substrate (h_2), h_1/h_2 , is less than about 5 %. Stress was measured on Ni-alloy plates (Figure 2.11), steel and brass stripes (Figure 2.12) and according to following Table 2.5.

Table 2.5. Substrate material type, and geometry.

Substrate material	Thickness, mm	Usable length, mm	Width, mm
Steel stripe	0.35 ± 0.05	29.40	3.75 ± 0.25
Brass stripe	0.80 ± 0.01	28.40	7.60 ± 0.30
Nickel alloy plate	0.241 – 0.248	20 ± 1	20 ± 1

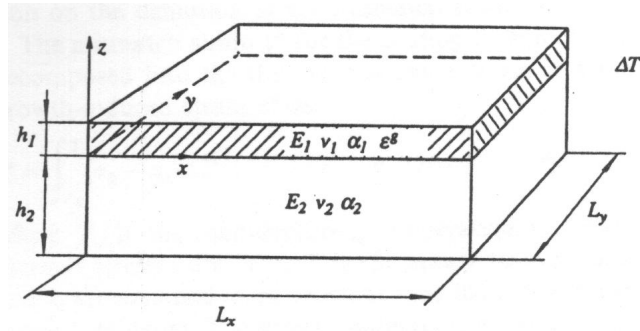


Figure 2.11. Schematic representing the coated steel plate for determination of residual stresses.

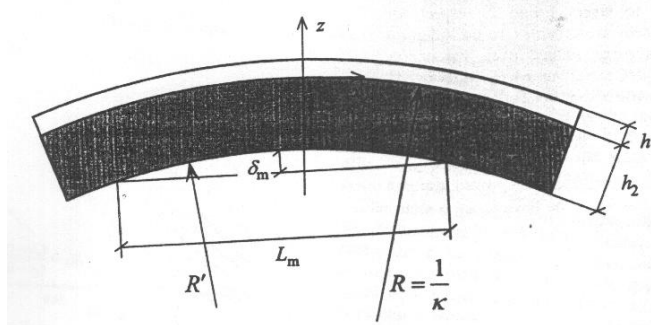


Figure 2.12. Schematic representing the coated steel stripe under residual stress for determination of residual stresses.

Stoney equation for stress calculation is following:

$$\sigma^* = \frac{E_1}{1-\nu_1} \varepsilon^* \quad (2.4)$$

where

$$\varepsilon^* = -\frac{1}{6} \frac{1}{m_r t_r} h_2 k, \quad (2.5)$$

$$t_r = \frac{h_1}{h_2} \text{ and} \quad (2.6)$$

$$m_r = \frac{E_1(1-\nu_2)}{E_2(1-\nu_1)} \quad (2.7)$$

resulting film residual stress calculation formula for steel stripes:

$$\sigma_f = -\frac{E_2}{3L^2(1-\nu_2)} \frac{h_2^2}{h_1} k, \quad (2.8)$$

and film residual stress calculation formula for steel plates:

$$\sigma_f = -\frac{4}{3} \frac{E_2}{L^2(1-\nu_2)} \frac{h_2^2}{h_1} k, \quad (2.9)$$

where

σ_f – film residual stress; k – alteration of the curvature; E_1 – Young's modulus of film; E_2 – Young's modulus of substrate; h_1 – film thickness; h_2 – substrate thickness; ν_1 – Poisson's ratio of film; ν_2 – Poisson's ratio of substrate; L – length of the substrate; ε^* – mismatch strain; t_r – ratio of thickness; m_r – ratio of biaxial moduli;

2.2.3 Characterisation of friction and wear

Coefficient of friction

The pin-on-disc configuration (Figure 2.13) was included as the most simple and generally used model test in tribology research. Experiments were conducted in Uppsala University. The tribological properties of the PVD coatings were evaluated under unlubricated sliding conditions using pin-on-disc equipment. Test pins with spherical shape ($d = 6$ mm) were made of bearing steel to measure friction coefficient of coatings against it. In order to reduce the number of tests and specimens all coatings were investigated at constant normal load of 5 N and constant line speed of 0.1 m/s, corresponding to substrate rotational speed of 306 rpm. All tests were performed at 21 ± 1 °C in laboratory air (35 – 40% relative humidity). A new spot on the pin was used every new friction test and the pin surface was cleaned with acetone and alcohol before each test [128].

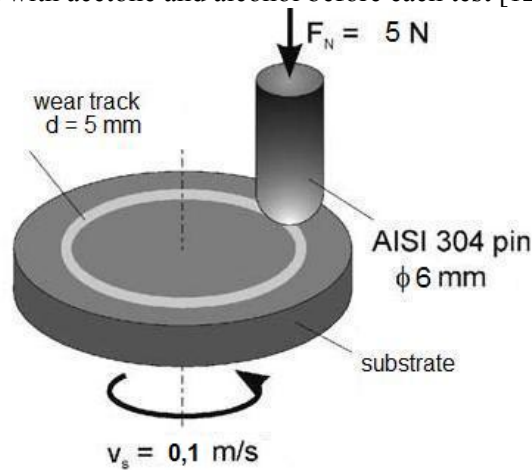


Figure 2.13. The schematic of pin-on-disc tester.
Abrasion

The resistance to abrasion was studied according to ASTM G65-94 dry sand / rubber wheel test scheme with test conditions given in Table 2.6. The rubber disk with diameter 80 mm for testing of 5×15×25 mm sized samples was used. The mean size of sand particles was 0.1 mm.

To quantify the weight loss during abrasion and erosion experiments, the specimens were ultrasonically cleaned in acetone and weighed before and after the tests to the nearest of 0.01 mg. For the abrasion and erosion test results the weight loss is given with respect to the weight of abrasive and the sliding distance correspondingly. The volumetric loss was not calculated due to the gradient structure of the coatings.

Table 2.6. Abrasion wear test conditions.

Parameter / Description	Description
Scheme	Block-on-wheel
Description of wheel	Steel with rim made of chlorobutyl rubber, diameter 80 mm, width 8 mm
Abrasive	SiO ₂ with mean size of 0.1 mm, HV=11 GPa, feed rate 300 g min ⁻¹
Circumferential velocity	2 m/s
Linear abrasion	60 – 200 m, depending on the preliminary tests of wear resistance without reaching the substrate
Force against specimen	18.65 N that results in 20% lower contact pressure between specimen and rubber disk compared to standard test configuration (calculated according to standard Hertz equation).
Atmosphere	Air, 23±2 °C, relative humidity 45±5 %

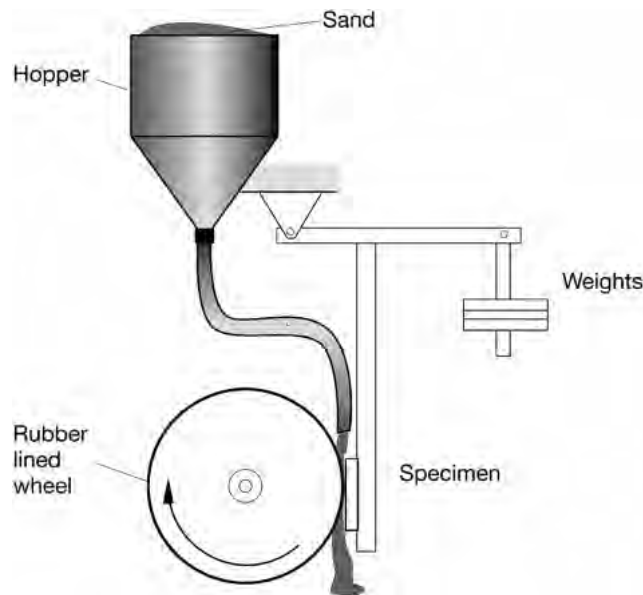


Figure 2.14. The schematic of the dry sand rubber wheel abrasion tester [90].

Unlubricated sliding wear tests were carried out using BAQ spherical cap grinder KaloMax. The diameter of the ball was 30 mm. The ball speed and grinding period were varied between 100–1000 rpm and 20–120 s, respectively.

Erosion

To study the erosion resistance of thin PVD coatings, a four-channel solid particle accelerator described in details elsewhere [114] has been used. This device (Figure 2.15) allows testing of 15 samples simultaneously that enables to test all coating types at the identical conditions. The test conditions are given in Table 2.7.

Table 2.7. Erosion testing conditions.

Parameter	Description
Abrasive	SiO ₂ with mean size of 0.1 mm, HV=11 GPa
Impact velocity	20 m/s
Impact angle 30°	30°
Atmosphere	Air, 23±2 °C, relative humidity 45±5 %

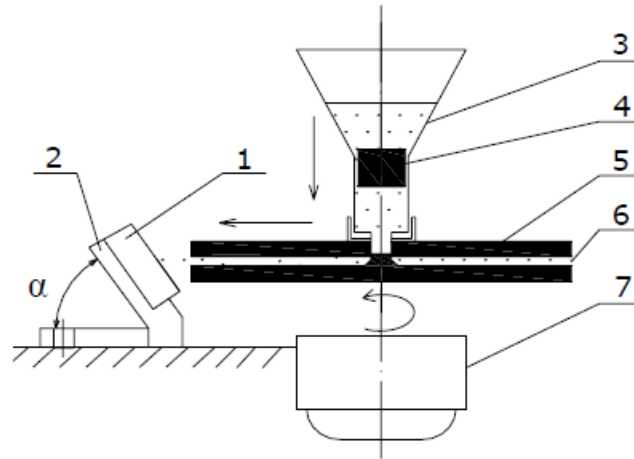


Figure 2.15. The schematic of erosive wear tester; 1- specimen, 2 – specimen holder, 3 - abrasive particles vessel, 4 – shield, 5 – rotor, 6 – hollow channel for particles 7 – drive motor.

Surface fatigue

The surface fatigue wear testing was performed on impact wear tester (Figure 2.17) designed and produced at TUT (see details in Table 2.8) [115]. The special design using ball indenters (Figure 2.16) up to 30 mm in diameter enables to study the behaviour of coatings under conditions of dynamic compressive stresses (flat-to-flat contact) that are characteristic to blanking. Tests with soft (steel) substrate are suitable for promoting of the impulsive strain with the maximum near the edges of imprint that is crucial for rolling bearings or gear applications. These conditions are close to that generated by smaller size indent balls used for impact tests done by other authors [116, 117].

The dynamic load is transferred from the hammers that are connected to, and accelerated by the rotating disk. The transferred energy depends on speed and mass of hammers and can be adjusted. Hammers fastened on the periphery of the disk allow increasing the frequency at least up to 100 Hz. The affordable frequency of the impact is higher than that of hydraulic or electromagnetic testers and the energy is higher than that of pneumatic ones [116, 117, 118, 119]. To minimize the wear of moving parts and its effect on the change of contact conditions during testing the arm type construction was applied. The force measurement system (force sensor) with the protection from overloading was used for monitoring of the contact parameters.

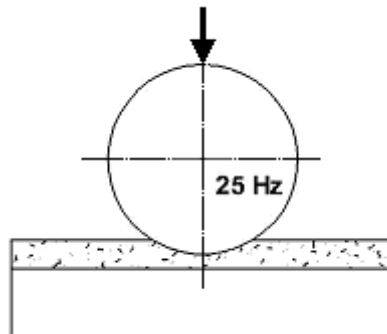


Figure 2.16. Schematic of impact wear testing principle.

The surface fatigue testing parameters (impact force, frequency of impacts) were chosen to be comparable to that of blanking of grooves in the 0.5 mm thick electro-technical sheet steel with use of a three-position die mounted on an automatic press studied previously [120, 121, 122].

Table 2.8. Impact wear testing conditions.

Feature / Parameter	Description	
	Available	Tested
Distance from centre of the disk to the point of impact of hammer, mm	210	
Number of hammers, pcs.	1 – 12	12
Mass of hammer / mass that impacts the specimen, g	10 – 100	49
Frequency of disk rotation, Hz	1 – 20	2.08
Frequency of the impacts, Hz	12 – 240	25
Speed of the hammer in the impacting point, m/s	1.3 – 25.0	2.75
Energy of the impact, mJ	3 – 500	180
Ball (indenter) diameter, mm	3 – 30	12
Material of indenter	WC-6Co	

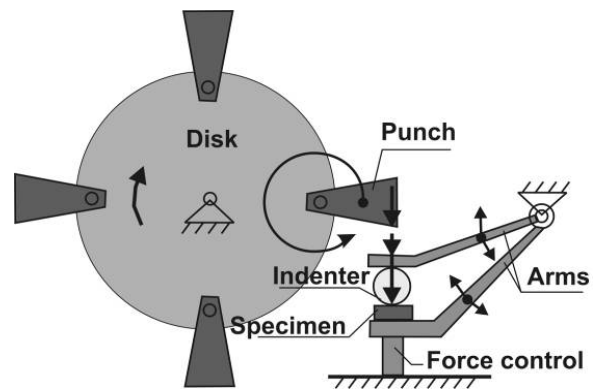


Figure 2.17. Schematic of impact tester.

3 TECHNOLOGY AND PROPERTIES OF COATINGS

3.1 Study of commercial coatings

3.1.1. Coating deposition process parameters

Five different PVD coatings among them monolayer, multilayer, microlaminates, gradient – TiN-TiCN-TiAlN-AlTiN and nanocomposite coatings (multilayers and microlaminate) nACo® (nc-(Al_{1-x}Ti_xN)/a-Si₃N₄) on different substrates were studied. Mechanical properties of substrates are given in Table 2.2.

The specimens were heated up in a vacuum chamber to a temperature of 450 °C (temperature was measured with a K-type thermocouple) and were kept there for one hour in a vacuum better than 1×10^{-4} mbar (the pressure in the vacuum chamber was measured with the Baratron and Pirani vacuum gauges). Then all samples were cleaned in a pulsed Ar glow discharge at 425 °C, with a bias of – 850 V at a pressure of 4×10^{-3} mbar to reduce contaminants and oxides on the surfaces of the samples. Ti cathode was cleaned in argon plasma at arc current of 60 A, and had a virtual shutter in an “ON” mode. After that, a thin metallic pure Ti layer (Ti etching) was deposited in an argon environment at a temperature of 430 °C, at pressure of 4×10^{-3} mbar and with a bias of – 850 V. During this step Ti cathode arc current was reduced to value of 52 A. Later on, the substrate bias voltage was increased to a value of – 900 to – 1000V to create a valuable adhesion layer on a surface of the substrate. It was done as to be effective and to prevent delamination of thin coatings an adhesion interlayer is desirable [123]. The substrate table had a rotational speed of 12 rpm. The main parameters of the deposition process have been collected in Table 3.1 with reference to coating system.

Table 3.1. Deposition parameters after etching process.

Coating	Bias voltage, V	Pressure, mbar	Ti /Al/AlSi cathode arc current, A	Temperature, °C	Ar / N ₂ ; C ₂ H ₂ flow, sccm
TiN	(– 75) – (– 120)	8×10^{-3}	100 – 125	450	6/200
TiCN	(– 60) – (– 120)	$(5-7) \times 10^{-3}$	120 – 130	450	6/ 165 – 180; 7 – 39
TiAlN	(– 60) – (– 150)	8×10^{-3} – 1.5×10^{-2}	85 – 125/ 65 – 115	475	6/200
AlTiN	(– 60) – (– 150)	4×10^{-3} – 1.2×10^{-2}	60 – 125 / 52 – 130	430 – 450	6/150 – 200
nc-AlTiN/a-Si ₃ N ₄	(– 75) – (– 150)	9×10^{-3} – 1.2×10^{-2}	82 – 125/ 65 – 100	435 – 475	6/200

All samples were removed from the vacuum chamber after the temperature decreased to a value of around 100 °C.

TiN and **TiCN** were deposited as a gradient layer. The cathode arc current, arc tracking coil current, vacuum chamber pressure, substrate temperature and substrate bias voltage were changed simultaneously during the process of the deposition (Table 3.1).

Since **TiAlN** coatings (monolayer and microlaminate) has both Ti and Al content; two different high purity (99.9 %) Ti and Al cathode were used. Ti content in the coating structure can be increased or reduced by manipulating the cathode arc current and cathode arc tracking coil current. During the beginning of the deposition only Ti cathode was used and TiN layer was formed on top of the Ti interlayer. After that Al cathode was activated and its current was increased step-by-step. Substrate bias was held in a range of – 120 to – 60 V having higher values in the beginning of the new layer, which led to a fine crystalline structure of the condensed film (Table 3.1).

AlTiN was deposited as a gradient multilayer coating. In the beginning of the first layer (TiN), substrate bias voltage was decreased from – 120 to – 75 V to relieve the stresses and led to larger domain size in the layer. Later on the Ti cathode current was decreased to 120 A, and the bias was held constantly at – 75 V. Ar and N₂ flow were held at a stable 6 and 200 sccm region accordingly. The following step was made to increase the adhesion of the next layer. The next steps characterization is given in Table 3.1.

The final coatings of the series of the experiments were nanocomposite coatings (gradient – nACo hardgrad, microlaminate – nACo MLH and multiplayer nACo Gold) **nACo®** or **nc-(Ti_{1-x}Al_xN)/a-Si₃N₄**. During the coating process two different cathodes AlSi (18 wt% of Si) and Ti cathode and two different gases – Ar, N₂ were used. After Ar and Ti etching a TiN layer was formed at a pressure of 9×10^{-3} mbar and Ti cathode arc current of 125 A. Bias was held at a level of – 120 V. After that, several gradient layers were deposited. Ti cathode arc current and bias was dropped to 120 A and – 75 V. Pressure was decreased to 8×10^{-3} mbar (Table 3.1).

3.1.1 Characterisation of studied systems

Microstructure and mechanical properties of coatings and substrates

Coating thickness

Different coating types represented in Table 3.1 were measured for thickness and roughness and are shown in Table 3.2. Coating thickness results from the ball crater test were verified with the SEM cross-section pictures and image analysis.

SEM image results are consistently about 1 – 10% lower than the ball crater test results. This is related to the slightly inclined positioning of the samples on the specimen stub. If the inclination angle is θ deg, the measured thickness is t_m and the real thickness is t_r , then the relationship between the three can be expressed as

$$t_r = t_m / \cos \theta, \quad (3.1)$$

which explains consistent difference between the SEM image and the ball crater test results.

Table 3.2. Average thickness of coatings.

Coating type	Thickness h_1 , μm
TiN	2.3 – 3.0
TiCN	2.3 – 3.0
TiAlN	2.3 – 3.0
AlTiN	2.3 – 3.0
nc-AlTiN/a-Si ₃ N ₄	2.3 – 3.0

Microstructure of the substrates

A chromium-molybdenum-vanadium alloyed SF Weartec™ and PM CWTS Vanadis 6 produced by Uddeholm were used as substrates for coating deposition. For Weartec and Vanadis 6 samples (plates) with sizes of 20x20x5 mm were prepared and heat-treated to a hardness of 64 HRC.

According to the manufacturer, high carbide content, size and distribution of carbides of the studied tool steels gives them an excellent friction wear (Weartec™) and chipping/cracking resistance (Vanadis 6). Powder steels, such as Vanadis 6 (Figure 3.1 b), have smaller carbide size than spray formed steels. Smaller grain size and carbides give a more uniform structure resulting in more homogenous PM steel and better fracture and fatigue properties

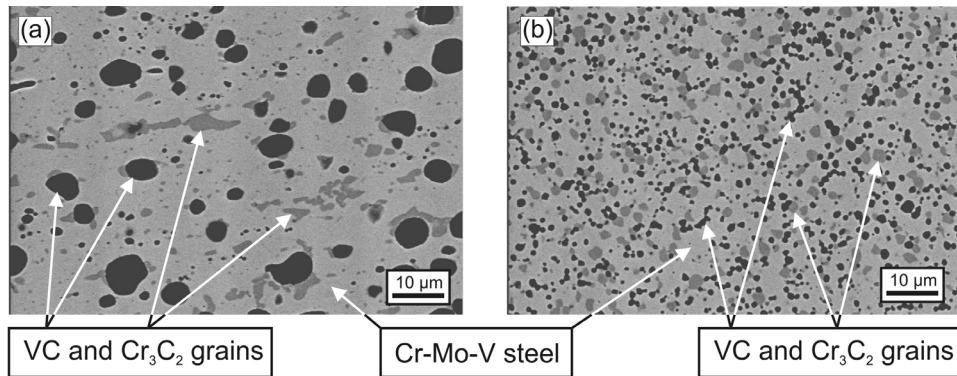


Figure 3.1. SEM images of steels microstructures: a – Weartec™ (SF), and b – Vanadis 6 (PM).

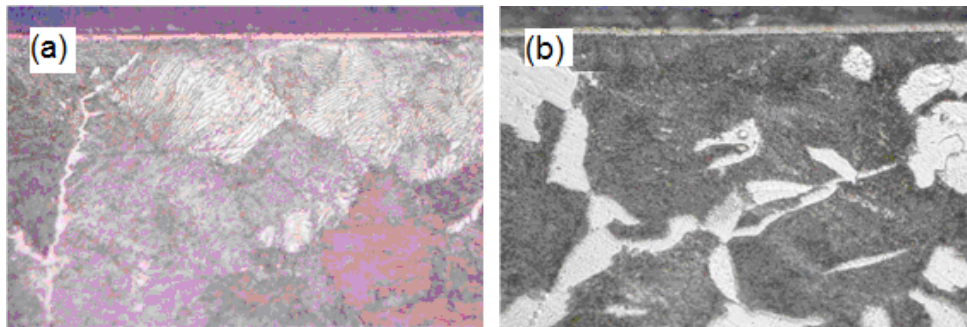


Figure 3.2. Microstructure of steels: a – carbonised steel C22E coated with TiCN, and b – steel C45 coated with TiN.

Nitriding steel 38CrMoAl8 round plate substrates were used for gas nitriding at temperature of 500 – 520 °C. As a result of this process surface hardness of 850 HV0.2 and case depth of 0.3 mm was achieved. Thereafter, subsequent deposition of hard coatings was performed. Microstructure of specimens were analysed using SEM microscope (Figure 3.3). SEM image, showing the grey austenite structure and embedded black Cr_2N phase taken from the crater of the spherical gas grinder sledge is shown in Figure 3.3 a. Cross-section of nitrided steel 38CrMoAl8 with intense dark Cr_2N phase below the TiCN hard coating is shown in Figure 3.3 b.

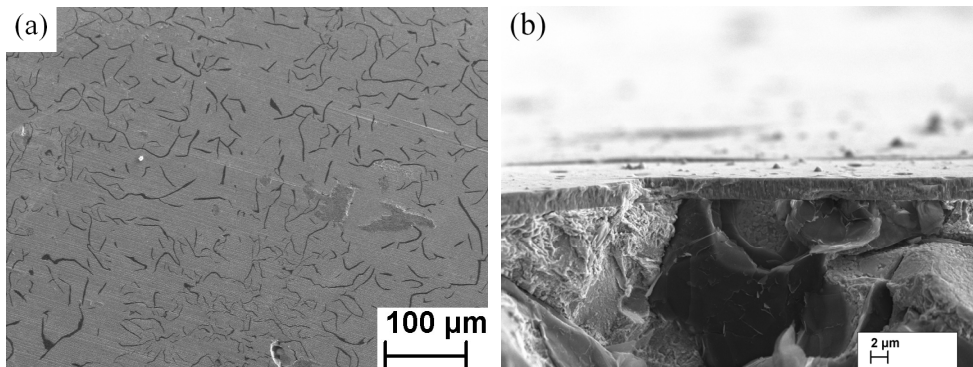


Figure 3.3. SEM images of microstructure of nitrided steels: a – top view of nitrided surface at magnification of 80X, and b – cross-section of TiCN coating on top of nitrided steel 38CrMoAl8 at magnification of 2000X.

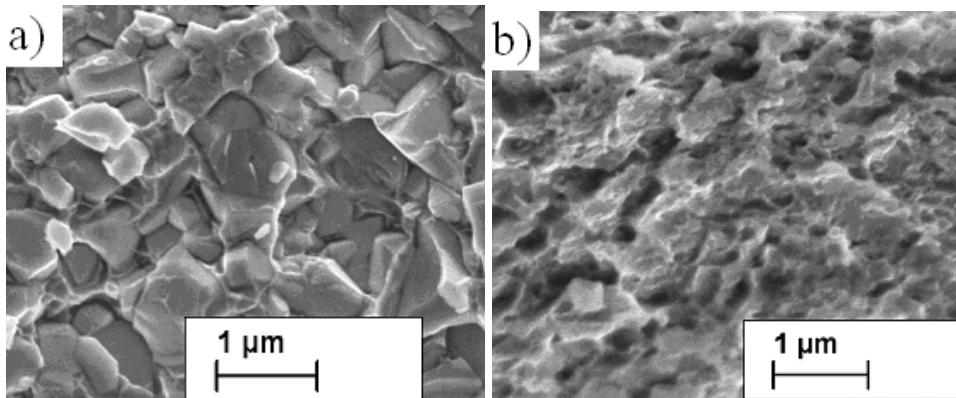


Figure 3.4. Comparison SEM micrographs of fractured substrates: a – H10 carbide composite, and b – cross-section of fractured nitrided steel 38CrMoAl8.

Three different grades of cermets were selected for testing, as they are prospective wear resistant composites (grade T70/14) and conventionally used (grade H15 and H10) as metal forming tool materials [121, 122, 124]. Specimens, plates with dimensions of 23x15x5 mm were produced through conventional press and sinter powder metallurgy routine by Laboratory of Powder Metallurgy of TUT. Test specimens were grinded and polished to the surface roughness of $Ra=0.2 \mu\text{m}$. Specimens of grade H10 were purchased from Pramet Tools s.r.o under the product name of HF10. Composition, microstructural parameters and main mechanical properties of tested WC- and TiC-based cermets are listed in Table 2.1 and Table 2.2. The microstructures of investigated WC-Co (H15 grade) and TiC-FeNiSi composites are presented in Figure 3.5. There is a distinct difference in the shapes of carbide grains as TiC-grains are more spherical (rounded) (Figure 3.5 b) compared with the angular shape of tungsten carbide (Figure 3.5 a). On a closer examination a core-rim structure of TiC-grains can be observed [125, 126] in Figure 3.5 b.

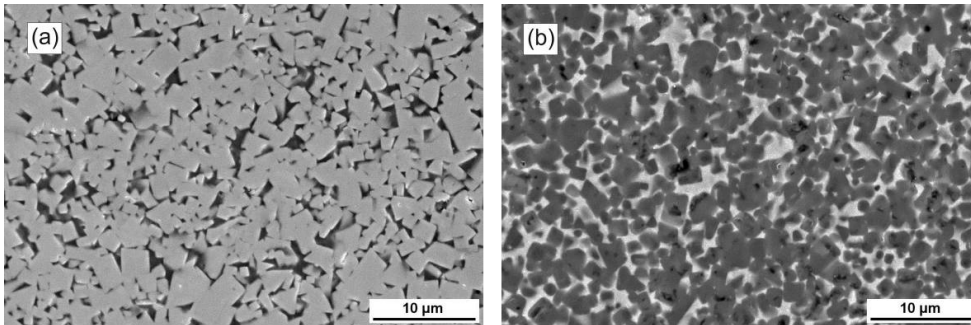


Figure 3.5. SEM micrographs of tested (a) H15 and (b) T70/14 carbide composites.

Microstructure of the coatings

Five different PVD coatings, among them monolayer TiN and multilayer gradient TiCN, multilayer and microlaminate nanocomposite coating nACo® (nc- $\text{AlTiN/a-Si}_3\text{N}_4$), microlaminate TiAlN and AlTiN were studied in this work. TiAlN and AlTiN coatings were deposited only on Weartec™ substrate in order to reduce the number of experiments.

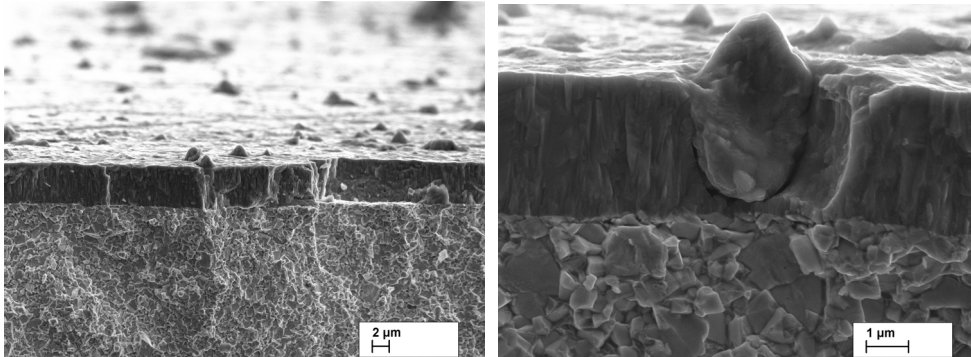


Figure 3.6. SEM images of a surfaces: a – gradient TiCN-MP coating covered with a number of macrodroplets, and b – TiN coating showing both the macrodroplets and the pinhole in front of it.

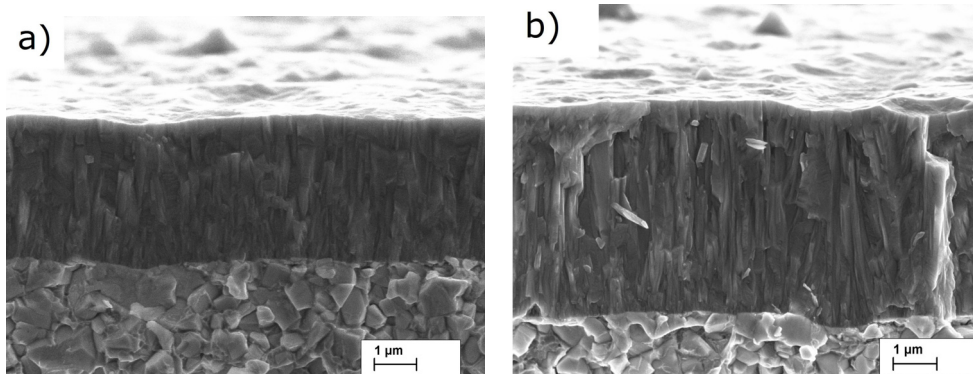


Figure 3.7. SEM images of fractured surface of hard PVD coatings on WC-10Co substrate: a – TiN and b – gradient TiCN-MP.

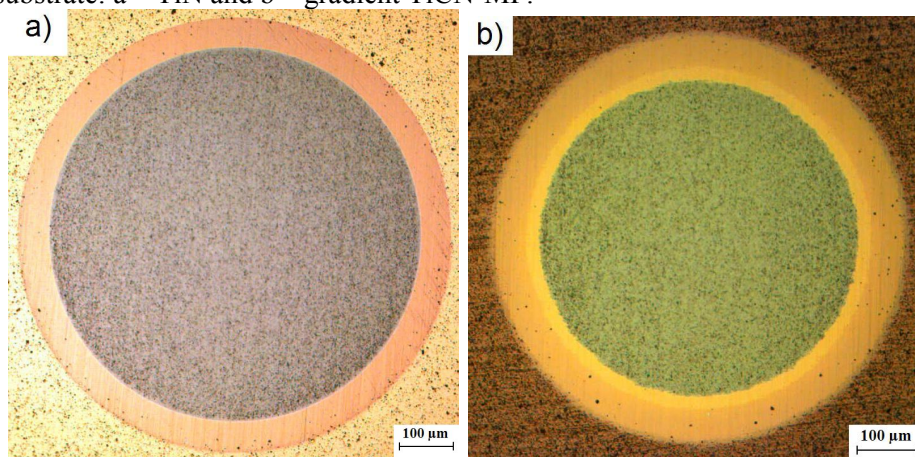


Figure 3.8. Optical microscope images of surface of hard PVD coatings on WC-10Co substrate after being treated with KaloMax: a – TiN, and b – TiCN-MP.

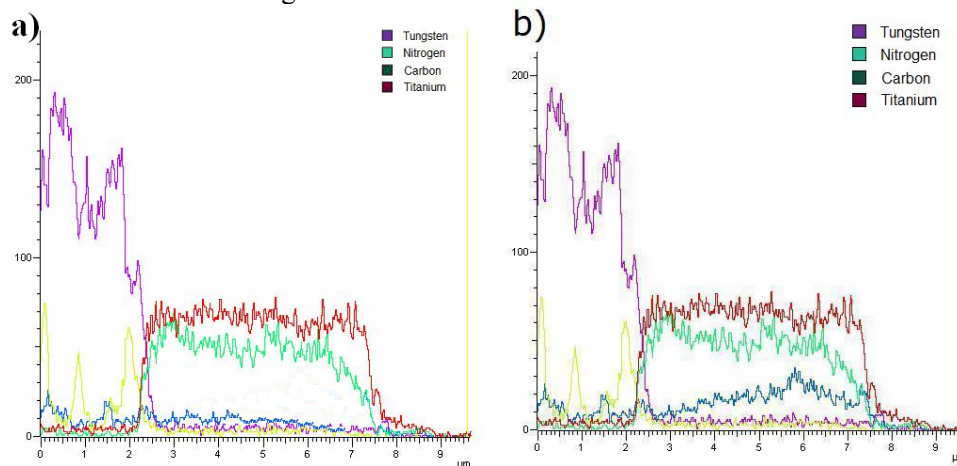


Figure 3.9. EDS images of the cross-sections of hard PVD coatings on WC-10Co substrate: a – TiN, and b – TiCN.

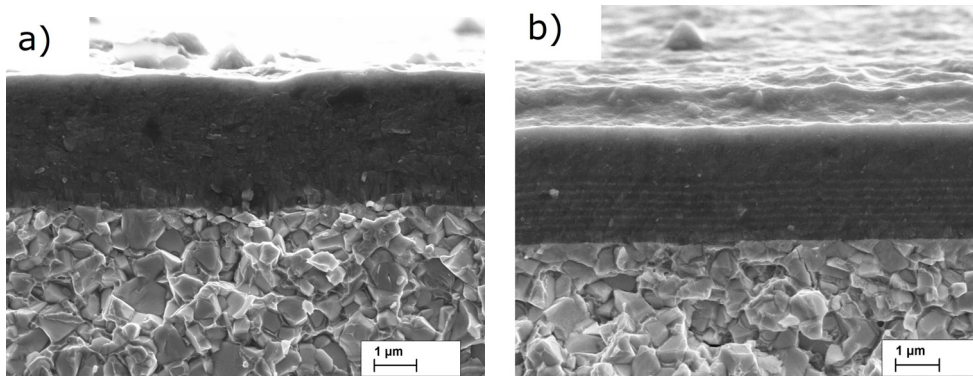


Figure 3.10. SEM images of fractured surface of a hard PVD coatings on WC-10Co substrate: a – gradient AlTiN - G, and b – microlaminate TiAlN-ML.

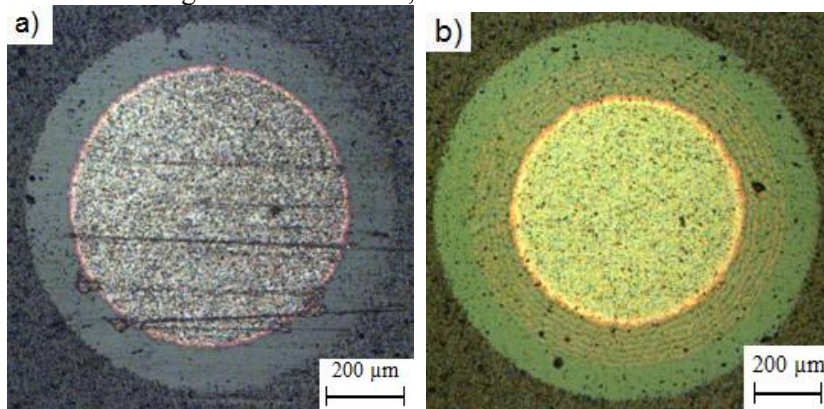


Figure 3.11. Optical microscope images of surface of hard PVD coatings on WC-10Co substrate after being treated with KaloMax: a – AlTiN, and b – TiAlN - ML.

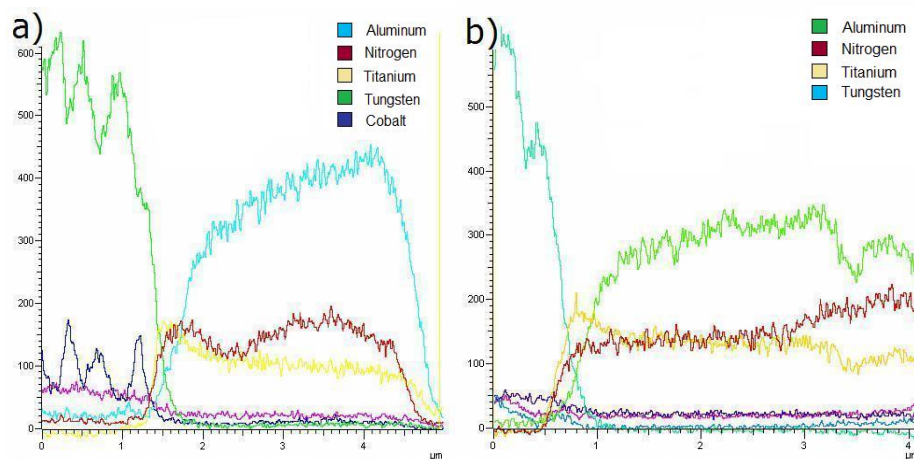


Figure 3.12. EDS images of the cross-sections of hard PVD coatings on WC-10Co substrate: a – gradient AlTiN-G, and b – microlaminate TiAlN.

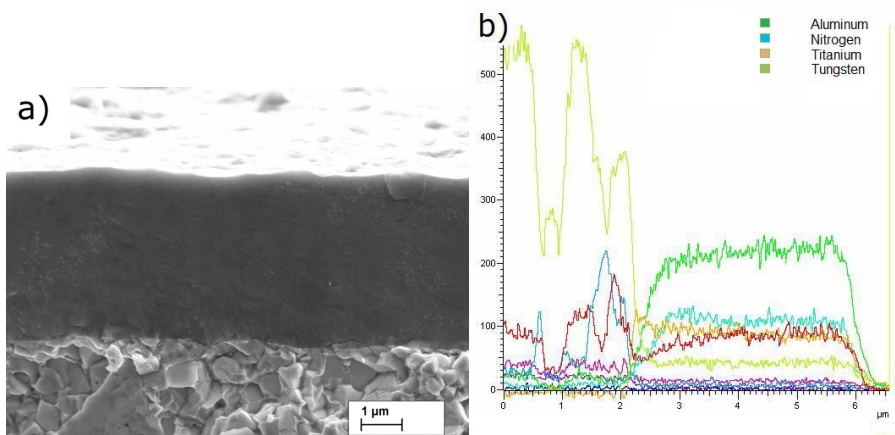


Figure 3.13. nc-(AlTi)N/a-Si₃N₄ hard PVD coating on WC-10Co substrate: a – SEM image of fractured surface, and b – EDS image of the chemical composition of the coating.

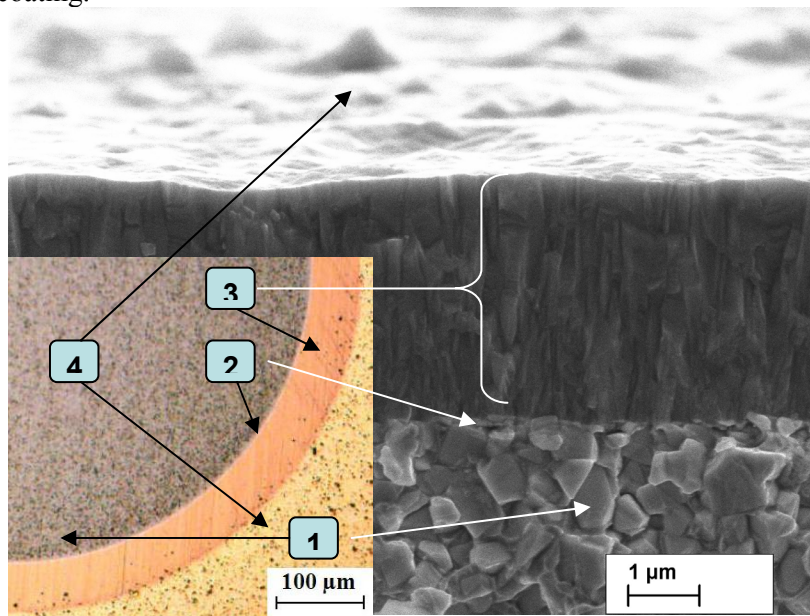


Figure 3.14. SEM and optical microscope images showing a architecture of TiN coating system having columnar structure accordingly: 1 – WC-10Co substrate; 2 – Ti adhesion layer; 3 – TiN coating, zone II, and 4 – coating surface with microdroplets.

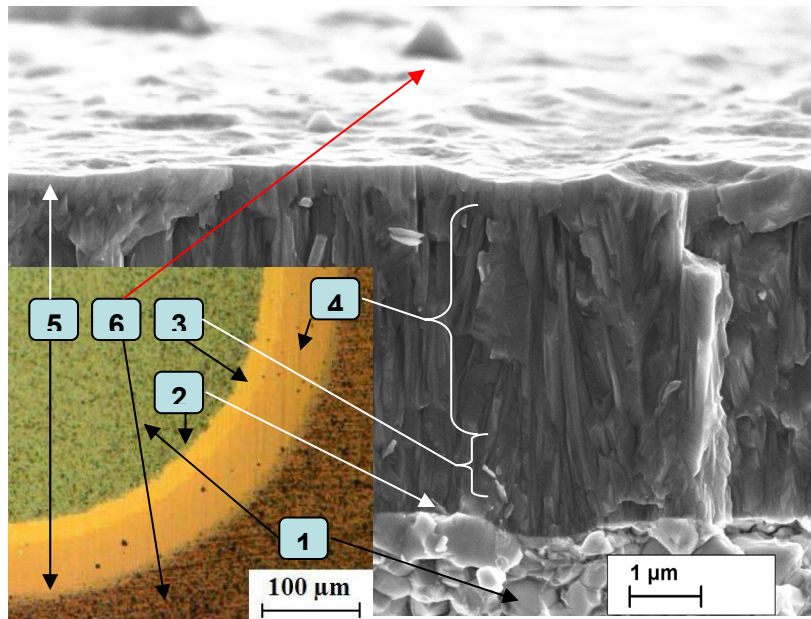


Figure 3.15. SEM and optical microscope images showing an architecture of TiCN-MP coating system: 1- WC-10Co substrate; 2 – Ti adhesion layer; 3 – TiN coating, zone II; 4 –TiCN gradient coating, zone II; 5 – C-rich TiCN top coating, and 6 – coating surface with microdroplets.

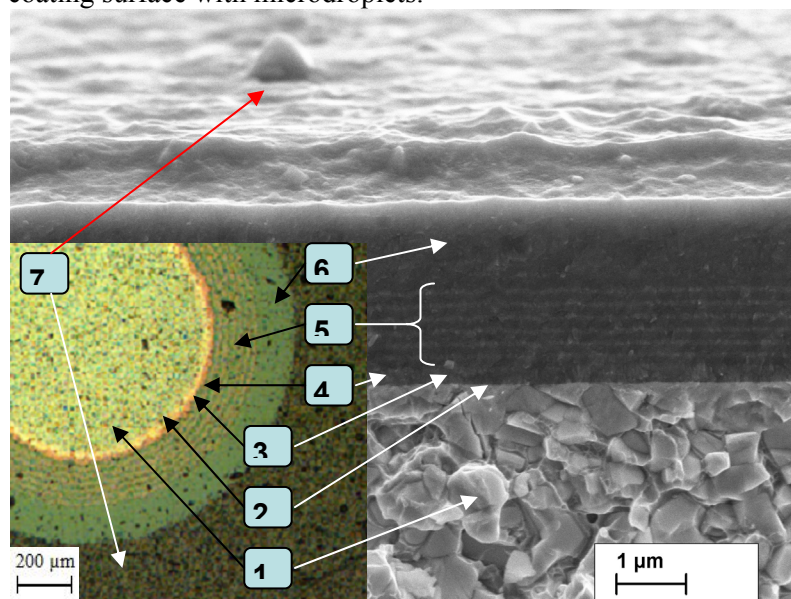


Figure 3.16. SEM and optical microscope images showing an architecture of a microlaminate TiAlN-ML coating system: 1 – WC-10Co substrate; 2 – Ti adhesion layer; 3 – TiN layer; 4 – TiAlN layer; 5 – TiAlN/AlTiN microlaminate coating; 6AlTiN coating, zone T (dense arrays of fibrous grains), and 7 –microdroplets.

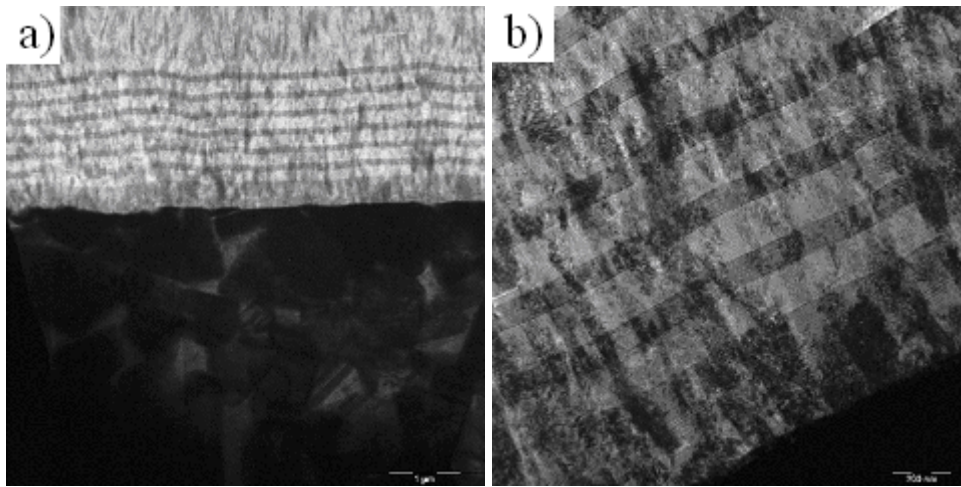


Figure 3.17. TEM images of microlaminate TiAlN-ML coating on hardmetal where the individual layers have higher and lower Ti/Al ratios: a – at magnification of 10000 x, and b – at magnification of 50000 x. Dark layers in (b) are TiAlN and light layers are AlTiN. The top light layer in (a) is AlTiN with small Ti content.

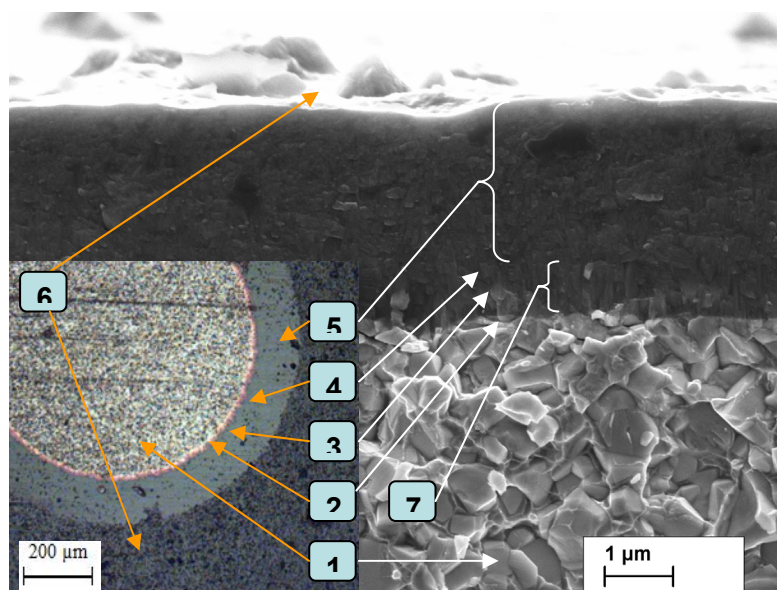


Figure 3.18. SEM and optical microscope images showing an architecture of AlTiN: 1- WC-10Co substrate; 2 - Ti adhesion layer; 3 - TiN layer; 4 - TiAlN gradient layer + AlTiN gradient layer; 5 - AlTiN gradient coating, zone T; 6 - coating surface with microdroplets, and 7 - columnar structure, zone II.

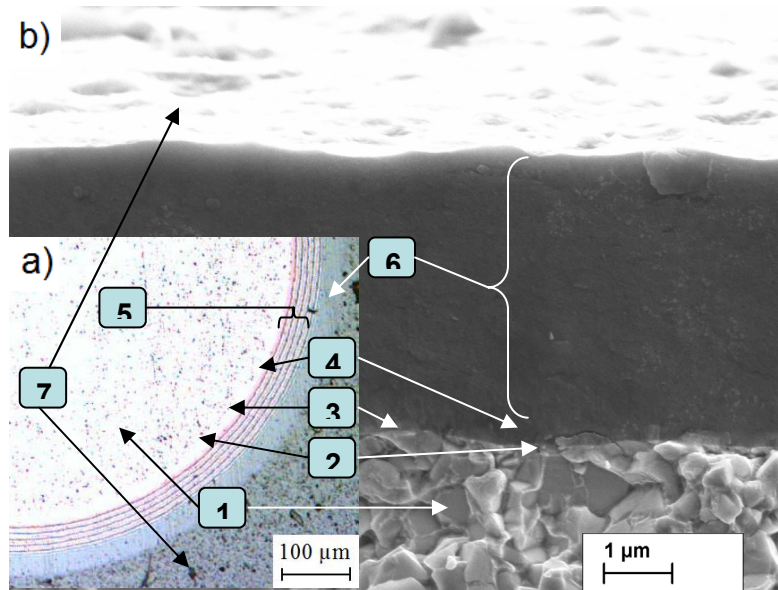


Figure 3.19. SEM and optical microscope images of nACo: a – microlaminate nACo-MLH, and b – multilayer nc-AlTiN/a-Si₃N₄ referred as nACo-hardgrad-HSS. 1- WC-10Co substrate; 2 – Ti adhesion layer; 3 – TiN layer, zone II; 4 – TiAlN gradient layer + AlTiN gradient layer; 5 – nc-TiAlN/a-Si₃N₄ - nc-AlN/a-Si₃N₄ microlaminate coating; 6 – nc-AlTiN/a-Si₃N₄ gradient coating, zone T, and 7 – coating surface with microdroplets.

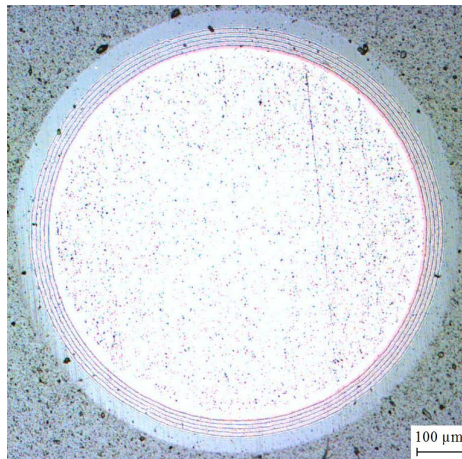


Figure 3.20. Optical microscope image of surface of microlaminate nc-AlTiN/a-Si₃N₄ hard PVD coating on WC-10Co substrate after being treated with spherical cap grinder.

Surface roughness

Coatings represent a key opportunity for cutting tool performance enhancement. The advanced coatings increase tool hardness, toughness, and wear and heat resistance. The key problem facing the tools market is the increasing lifetime of the tools. To reach this goal two main trends exist in hard coatings technology: increase in hardness and reduction in the friction coefficient [127]. The friction coefficient depends on many parameters, including roughness, hardness, adhesion (cohesion), etc [90].

The surface roughness of the CWTS Weartec™ substrate, and TiN and nanocomposite (nc-Ti_{1-x}Al_xN)/(a-Si₃N₄) (nACo) hard coatings was investigated by using AFM and profilometers.

The AFM study revealed that the TiN has lower surface roughness compared to nACo. The RMS roughness values both for TiN and nACo degraded with the size of scanned area. The RMS roughness value for TiN was calculated between 135 nm to 5 nm at different scan areas. However, nACo showed somewhat higher RMS roughness values from 160 nm down to 7 – 8 nm. A comparative study of root mean square (RMS) roughness of TiN and nACo revealed differences in growth modes of coatings [127]. The higher roughness of nACo in contrast to TiN is likely due to the cellular mode of nACo growth [127].

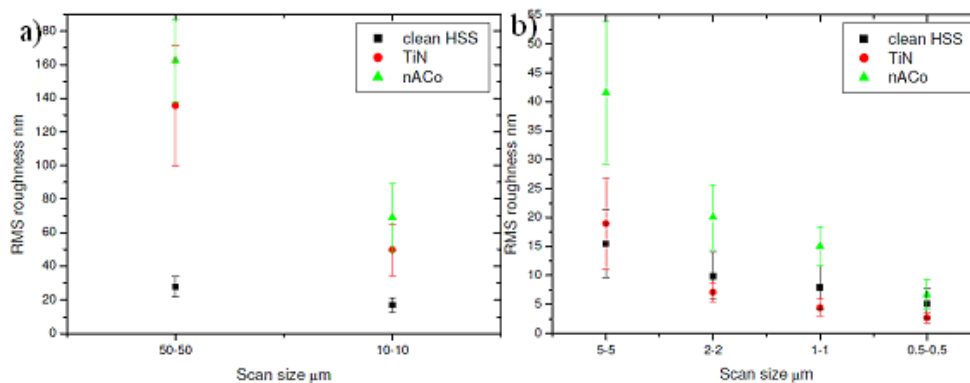


Figure 3.21. The RMS roughness results of AFM images recorded from the clean CWTS substrate, TiN and nACo from different scan areas: a – 50 μm² and 100 μm², and b – 25; 4; 1; 0.25 μm² [127].

The coatings were subjected also to a careful examination using SEM (shown in Figure 3.23 – Figure 3.28) and optical microscope (Figure 3.29) and optical, non contact) surface profilometry in order to investigate the tribological behaviour of the coatings investigated [128]. From each analysed area, the average roughness, R_a , was obtained. The surface roughness of as-deposited coatings is given in Table 3.3 and Table 3.4 [128].

Most of the as-deposited coatings had relatively smooth surface and relatively low number of defects on top surface. Surface roughness is hardly being avoided because of droplets that are characteristic to AIP process. The best surface morphology was found for as-deposited coatings of TiN and nACo [Figure 3.23 and Figure 3.28 b] resulting an average RMS roughness value of 26.6 nm and 30.9 nm accordingly. However, for coatings consisting aluminium, higher rates of droplet formation were observed. The melting temperature of aluminium is lower than that of the other components in the coating and the substrate, and because of this property, aluminium cathodes are more susceptible to droplet formation. Therefore, with increasing Al content the roughness of the surface increases. The melting point of Al is relatively low, in comparison with Ti; therefore it will enhance droplet formation [Figure 3.28 a]. Therefore, the as-deposited AlTiN has the highest number of droplets on the surface, resulting a RMS roughness value of 65.1 nm. An increase in the number of defects on top of the coatings could activate localized corrosion and therefore the corrosion resistance of AlTiN could suffer from it to a great extent than the other selected coatings. Other as-deposited coatings like TiCN and TiAlN (Figure 3.24 and Figure 3.26) showed moderate RMS roughness values of 55.5 nm and 46.4 nm accordingly. The optical profiler images of the wear tracks are given in Figure 3.30. The results of the optical profilometer study are given in Table 3.3.

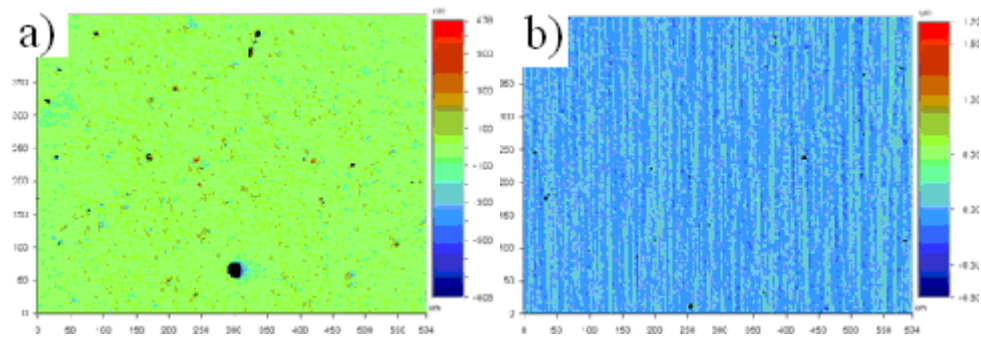


Figure 3.22. Optical interferometer images of surface roughness: a – TiN, and b – TiCN.

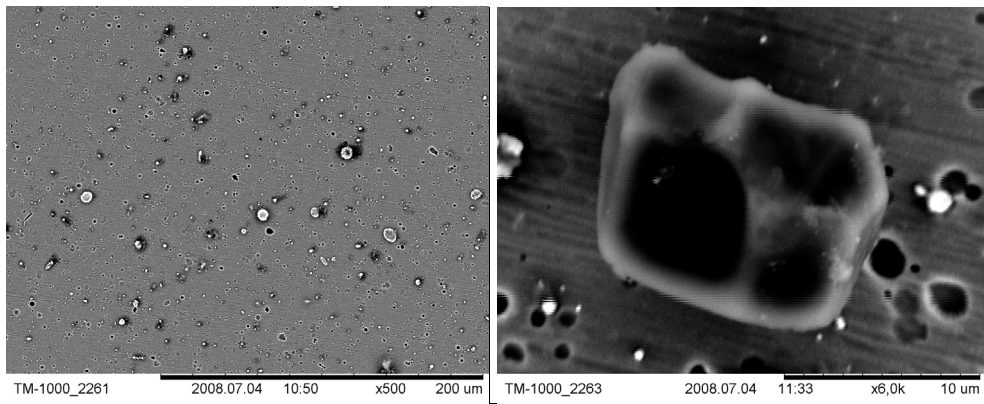


Figure 3.23. SEM images of the surface of TiN coating at different magnifications.

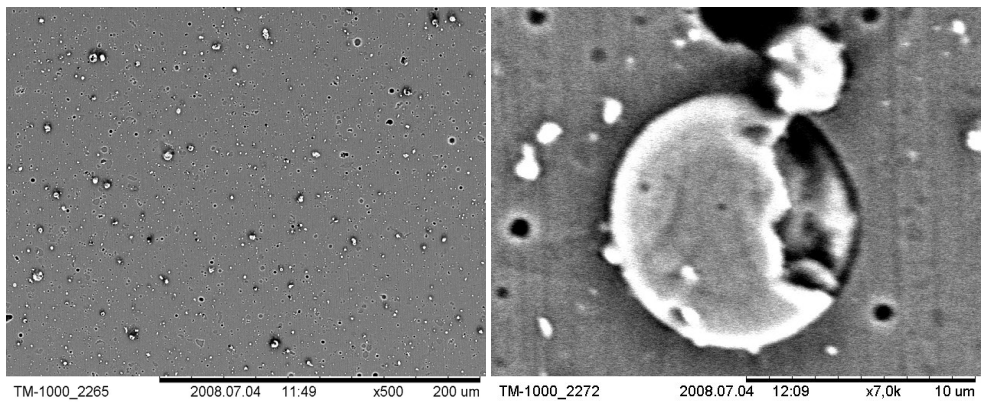


Figure 3.24. SEM images of the surface of TiCN coating at different magnifications.

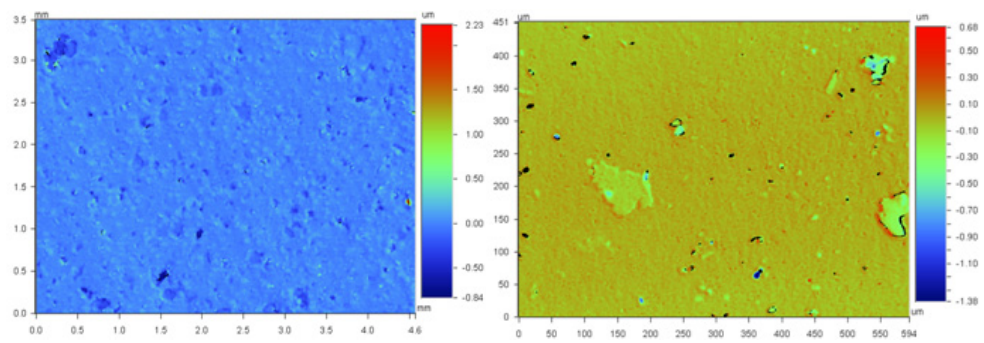


Figure 3.25. Profilometer images of surface roughness: a – TiAlN-G, and b – nc-AlTiN/a-Si₃N₄ (nACo) coating.

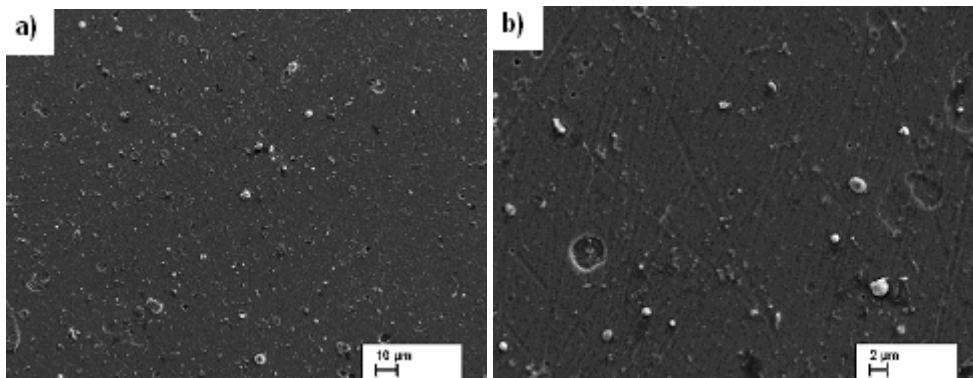


Figure 3.26. SEM images of the surface of TiAlN coating at different magnifications.

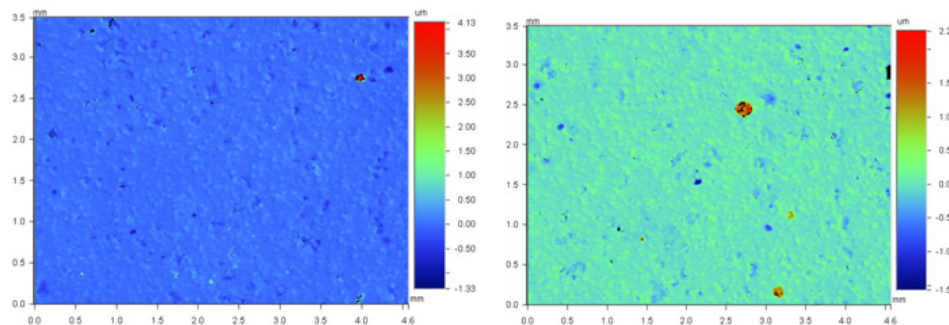


Figure 3.27. Profilometer images of surface roughness of AlTiN-G at different magnifications.

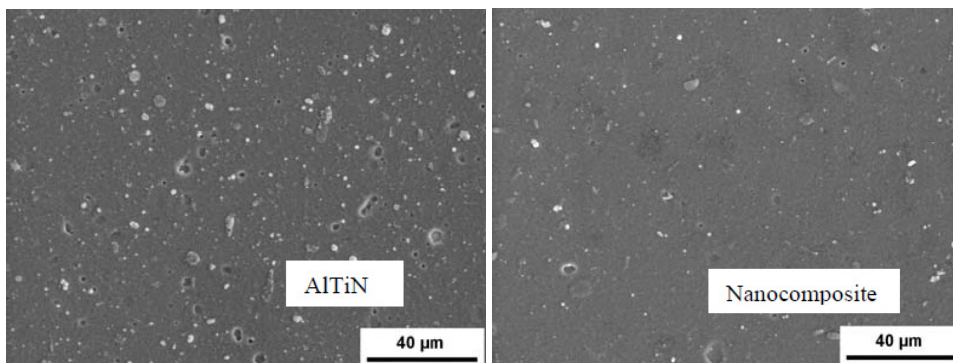


Figure 3.28. SEM images of the surface: a – AlTiN, and b – nAlCo coating.

Table 3.3. Surface roughness values of as deposited coatings obtained by optical profilometer.

Coating	R_a , nm	R_q , nm	R_z , μm	R_t , μm	RMS, nm
TiN	27.3	40.7	1.05	2.02	26.6
TiCN-MP	55.5	71.5	0.91	1.87	55.4
TiAlN	46.4	76.5	1.87	3.17	46.3
AlTiN-G	65.0	111.2	2.94	4.65	65.1
nc-AlTiN/a-Si ₃ N ₄	30.7	54.4	1.42	2.35	30.9

All of the worn coatings (worn during the pin-on-disc test) had circular shape wear track ($d = 5 \text{ mm}$) with relatively rough surface morphology surrounded by relatively smooth as-deposited surface area (Table 3.3).

The circular wear zone of the pin-on-disc test wear track affected by the contact with hard spherical tip of the pin is causing coating failure, which can be accelerated by presence of defects such as, for example local microdroplets. Micro cracking, partial layer removal, chipping of small segments of coating material are revealed and shown in Figure 3.29 and Figure 3.30. Those processes may be induced by coating wear debris that was not removed from the wear zone due to the shape of the crater (circular, hollow crater), resulting further adhesive, cohesive and abrasive wear of the coating, as well as an increase of R-values of the surface (Table 3.4).

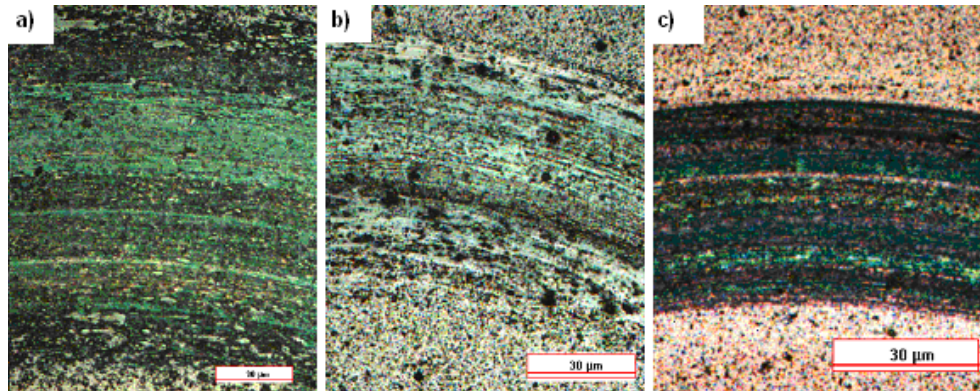


Figure 3.29. Optical microscope images of a sector of a circular wear track: multilayer TiAlN; b - gradient AlTiN-G, and c – multilayer TiCN coating

The best surface morphology was found for worn coatings of TiN and nAlCo again, resulting an average RMS roughness value of 32.3 nm and 42.8 nm accordingly. Other three worn coatings – TiCN, TiAlN and AlTiN-G showed higher surface roughness values of 82.2 nm, 81.6 and 81.4 nm respectively. The optical profiler and SEM images of the surfaces and are given in Figure 3.29. The optical profiler images of the wear tracks are given in Figure 3.29. The results of the optical profilometer study of worn coatings are given in and Table 3.4.

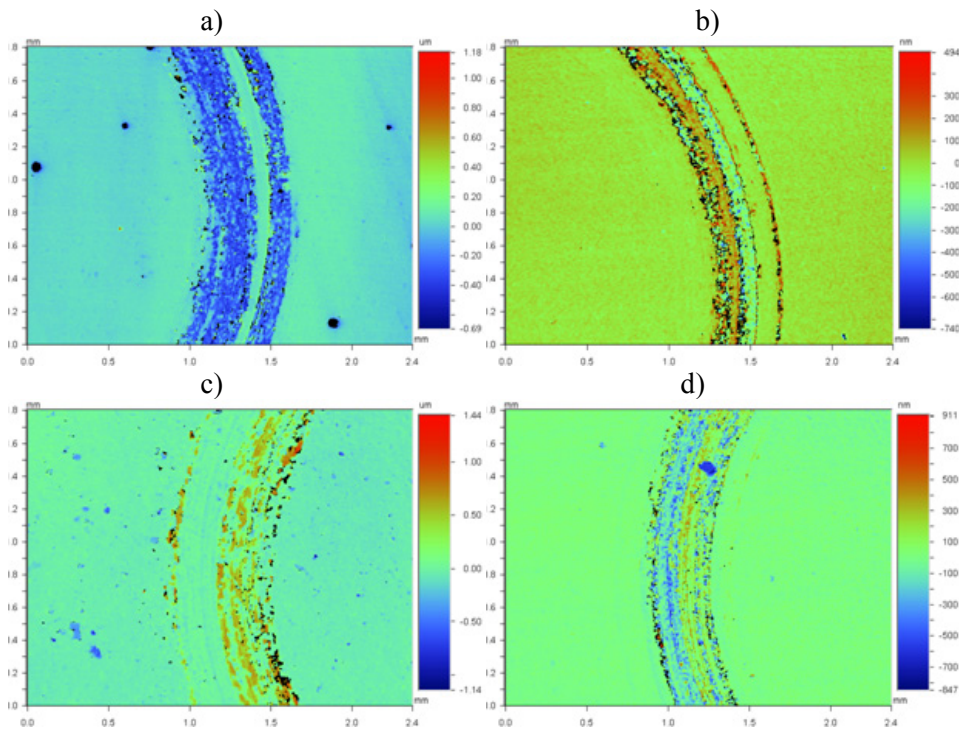


Figure 3.30. Optical interferometer images of wear track after CoF measurement: a – TiN; b – TiCN; c – TiAlN and d - nAlCo

Table 3.4. Surface roughness values of worn coatings obtained by optical profilometer.

Coating	R_a , nm	R_q , nm	R_z , μm	R_t , μm	RMS, nm
TiN	32.3	58.8	1.10	1.23	32.3
TiCN-MP	82.2	124.5	1.42	1.87	82.2
TiAlN	81.6	150.2	2.00	2.58	81.6
AlTiN-G	81.4	147.7	2.66	2.92	81.4
nc-AlTiN/a-Si ₃ N ₄	42.8	86.1	1.46	1.76	42.8

Hardness of coatings and substrates

Three different substrate types (carbon, low-alloyed and high-alloyed steels and hardmetals), see Table 2.2 and five different coatings were used in this study. Mechanical properties of the selected coatings were obtained using Buehler microhardness tester Micromet 2001. Results of the measurements are given in Table 3.5.

Table 3.5. Nanohardness values of selected coatings obtained by using Micromaterials Nano Test platform at average indentation load of 20 mN.

Coating	Type	Hardness, GPa	Young's modulus E , GPa
TiN	Monolayer, gradient	25.86±1.55	357±21.4
TiCN-MP	Gradient	31.04±2.82	345±31.3
TiAlN	Multilayer, microlaminate, gradient	30.17±1.52	342±17.2
AlTiN	Multilayer, gradient	29.00±3.51	325±39.3
nACo®	Nano-composite, multilayer, microlaminate, gradient	46.18±4.95	320±34.3

From the cermets as the most widely used materials for different wear applications owing to their excellent combination of high wear resistance and good strength-toughness WC-hardmetals with 10 and 15wt% Co-binder (grades H10 and H15) and TiC-base cermets with 70wt% TiC cemented with Fe and Ni (25.35wt% Fe and 4.2wt% Ni in binder) grade T70/14 were used in this study [129]. Hardness distribution through the specimen cross-section is shown in Figure 3.31.

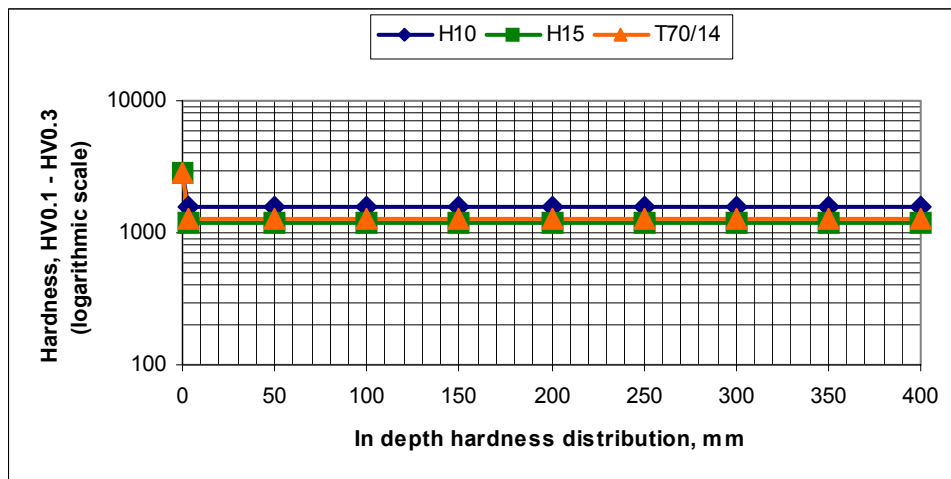


Figure 3.31. The hardness distribution of hardmetals coated with TiN

Selected CWTS Vanadis 6 and SF Weartec are both suited for PVD coating deposition due to their high tempering temperature. Vanadis 6 and Weartec both were case hardened to hardness of 64 HRC and have high tempering temperature of ca. 500 – 525 °C. This means that the PVD process temperature used should not exceed 500 – 525 °C to avoid decrease in hardness of the substrate. Since the process temperature during deposition of PVD coatings is below the tempering temperature – the hardness of the substrates remains to high values of 64 HRC. Nitriding could result in a hard surface layer, which is very resistant to wear and galling. The surface could achieve hardness of approximately 1250 HV0.2 after the

nitriding. Nitriding was not chosen for those substrates during this study because substrates retain its high hardness (850 HV0.01). Hardness distribution through the specimen cross-section is shown in Figure 3.32.

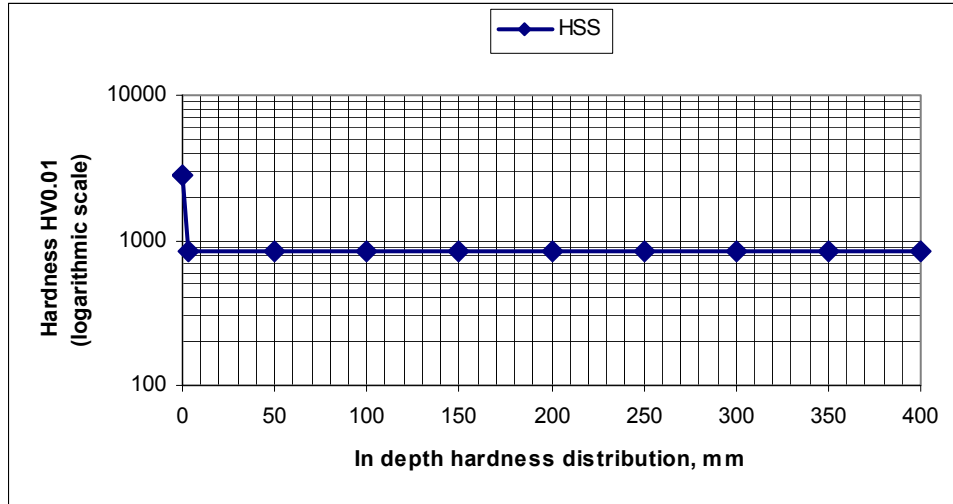


Figure 3.32. The hardness distribution of CWTS steel Vanadis coated with TiN

Table 3.6. Main mechanical properties of the studied coatings. Nanohardness obtained by using MTS Nano Indenter XP® nanohardness tester at target depth of 150 nm resulting average indentation load of 12 – 15 mN.

Coating	Type	Young's modulus E , GPa	Hardness, GPa	Poisson ratio	Thickness, μm (Ball-crater)	Surface roughness R_a , μm
TiN	Monolayer, gradient	438±80	28.5±0.6	0.22	2.3 – 3.0	0.08±0.01
TiCN	Multilayer, gradient	500±90	26.6±1.4	0.22	2.3 – 3.0	0.10±0.04
TiAlN	Multilayer, microlaminate, gradient	301±90	19.9±1.2	0.22	2.3 – 3.0	0.10±0.04
AlTiN	Multilayer, gradient	336±13	23.8±1.0	0.22	2.3 – 3.0	0.05±0.01
nACo®	Nano-composite, microlaminate, gradient	323±13	29.0±1.5	0.22	2.3 – 3.0	0.10±0.04

For duplex coatings plasma nitriding of substrates at temperature of 500 – 520 °C was performed. After plasma nitriding the specimens were re-polished to a mirror finish prior coating deposition. Hardness distribution of in case depth of nitrided steel given in Figure 3.33 shows that the core microhardness of the plasma nitrided substrate is 350 HV0.01 and the microhardness of the nitrided surface, having case

depth of 300 μm , is around 850 HV0.01 e.g. the surface hardness is increased by a factor of 2.4. The surface hardness did not achieve the hardness specified by the plasma nitriding service provider (1000 HV0.2). However, surface hardness of 850 HV0.01 was measured. Case depth of the nitrided structure was approximately 0.3 mm. Hardness distribution through the specimen cross-section is shown in Figure 3.33.

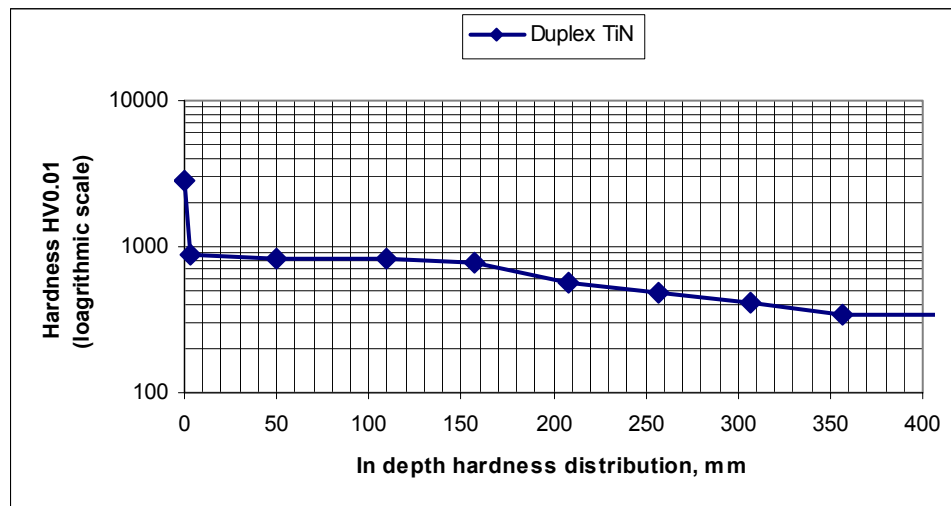


Figure 3.33. The hardness distribution of nitrided steel coated with TiN

The results of the nanohardness and Young's modulus values are given in Table 3.5 and Figure 3.34 demonstrates that at low load ranges 1–15 mN, corresponding to plastic indentation depths up to 3 – 5% of the total coating thickness, the nanohardness results are consistently lower than at higher loads of 20 mN. As shown in Table 3.5 and Figure 3.34, nanocomposite nACo[®] (nc-(Ti_{1-x}Al_x)N/Si₃N₄) showed the highest average hardness value of 46 GPa, that is similar to that what is reported by the other authors [7, 130, 131, 132, 133]. Hardness of coatings that were measured at Uppsala University showed less hardness due to the fact that no further polishing was done on the coated samples, and the effects of the roughness profile were very pronounced at the lower load regions. Depending on the part of the roughness profile the indenter hits a particular value (i.e. peak, valley or in-between); usually the results tend to be lower than the actual values. With the increasing load (*ca.* 20 mN at TUT), the effects of the roughness profile diminish due to the increased indenter depth, and the hardness values increase. After passing 10% of the thickness limit as the plastic indentation depth, the influence of the substrate starts to affect hardness measurements, and hardness starts dropping [134]. As a rule of thumb for healthy hardness measurements, the plastic indentation depth should not be higher than 10% of the coating thickness in order to avoid the influence of the relatively softer substrate [134]. To quantify the core hardness of the coatings, measurements with 20 mN were chosen as the most suitable ones. Because the resulting indent is deep enough to be free from the

influence of the roughness profile, but still below the 10% coating thickness depth, influence of the substrate is eliminated [134].

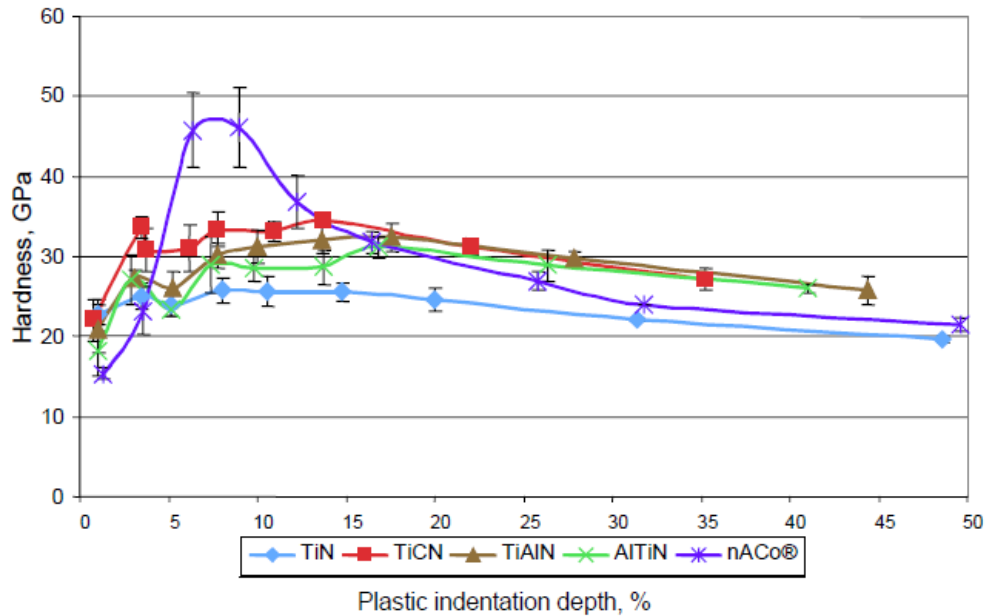


Figure 3.34. Nanohardness values at different indentation depth (given as a percentage of a coating thickness) [134].

Characterization of “substrate–coating” system properties

Adhesion

The coating adhesion was evaluated with a scratch tester equipped with a 200 μm radius Rockwell-C rigid conical diamond indenter, that was drawn across a coating, deposited onto a case hardened tool steel Weartec SF surface, at loading rate of 10 N/mm with increasing normal load from 0 – 100 N, loading time of 1 min was used. The failure events were detected by examination of the scratch track after scratching using an optical microscope. The critical load modes (L_c) for coating failure as cracking or spallation were determined by analysis using an optical microscope and the results of that study are given in Table 3.7.

A general rule of thumb says that a critical load of 30 N in scratch testing with a Rockwell C diamond tip is sufficient for sliding contact applications. It should be pointed out that the critical load usually increases with substrate hardness and coating thickness, and decreases with increasing surface roughness [98].

All failures investigated (Figure 3.35 – Figure 3.40) were brittle failures, which propagated along or near to the interface, causing flaking of the coatings inside and at the edges of the scratch track.

TiN

The surface in scratch test track of TiN coating in Figure 3.35, b shows relatively few (irregular) coating spallation spots (mode *Lc3*) at both sides of the track borders. There is a complex failure mode developing at the end of the track tip i.e. cracks being generated along the track borders and wedge crack formed some way ahead of the moving indenter coating chipping i.e. cohesive buckling (mode *Lc2* in Figure 3.35, c) from both sides, but is more visible in the lower part of the track border, as well as spallation of the coating at the track edges (dark areas) and gross interfacial shell-shaped spallation from the bottom of the scratch track is visible as multiple dark areas in Figure 3.35, c. Tip is moving from left to right. The critical load *Lc* is considered to be 32 N, i.e. normal load at which first coating failure mode – as irregular coating through-thickness spallation (*Lc3*) takes place.

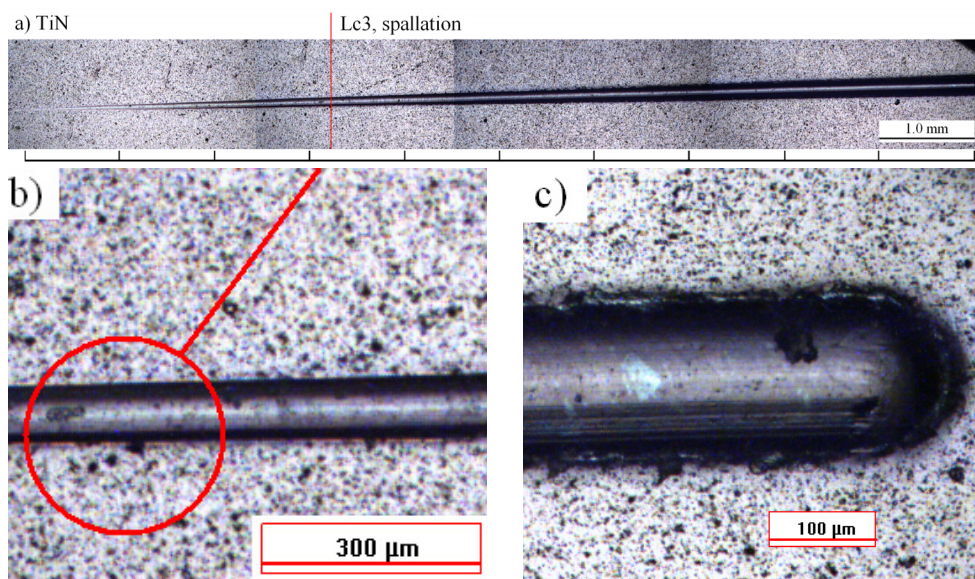


Figure 3.35. Surface cracks generated in scratch test track of TiN: a – sledge of the scratch test track, b – irregular coating spallation at lower track edge (*Lc3*), and c – a close-up look of the track end tip showing complex failure modes.

TiCN

The surface cracks and crack track generated in TiCN coating is shown in Figure 3.36, a. Figure 3.36, b shows relatively few (irregular) coating spallation spots (mode $Lc3$) at lower side of the track border. There are angular forward type Chevron cracks developing along the track borders and wedge cracks formed some way ahead of the moving indenter coating chipping i.e. cohesive buckling (mode $Lc2$ in Figure 3.36, c, white dots) from both sides, as well as spallation of the coating at the track edges (dark areas) and gross interfacial shell-shaped spallation from the bottom of the scratch track is visible as multiple dark areas in Figure 3.36, c. Tip is moving from left to right. The critical load Lc is considered to be 21 N, i.e. normal load at which first coating failure mode – as irregular through-thickness spallation ($Lc3$) takes place.

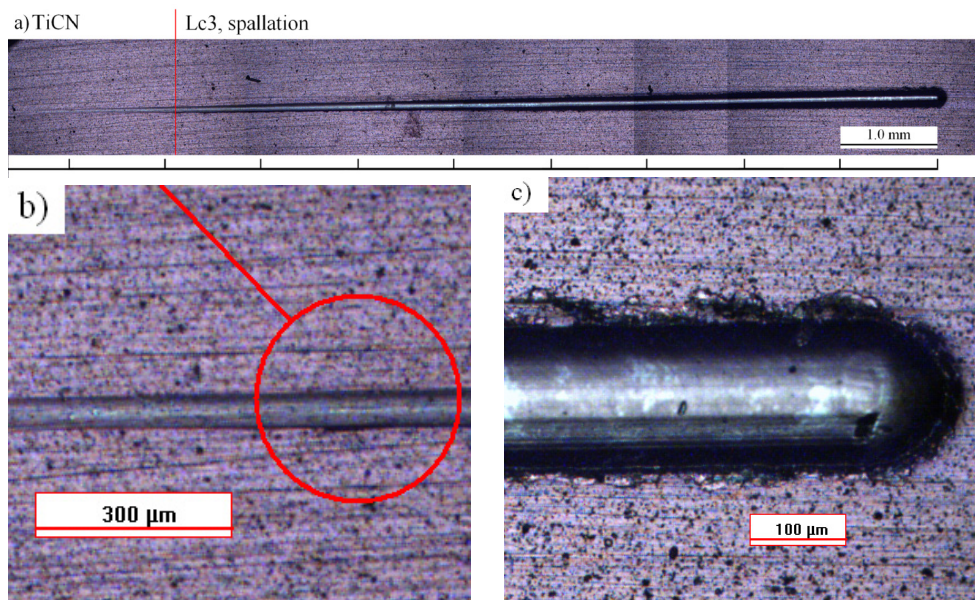


Figure 3.36. Surface cracks generated in scratch test track of TiCN: a – sledge of the scratch test track, b – irregular coating spallation at lower track edge ($Lc3$), and c – a close-up look of the track end tip showing complex failure modes.

TiAlN - ML

The surface cracks generated in microlaminate TiAlN coating are shown in Figure 3.37, a. Figure 3.37, b shows relatively moderate interfacial coating chipping (buckling, mode $Lc2$) and spallation spots (mode $Lc3$) at both side of the track border generated in response to stresses and individual buckles. There are angular transverse type Chevron cracks that have developed along with the track borders as can be see in Figure 3.37, b. Also spallation of the coating at the track end and sides (dark areas) can be seen (see Figure 3.37, c). The critical load Lc is considered to be 24 N, i.e. normal load at which first coating failure mode – as

moderate buckling ($Lc2$) and most probably layer – thickness spallation ($Lc3$) takes place.

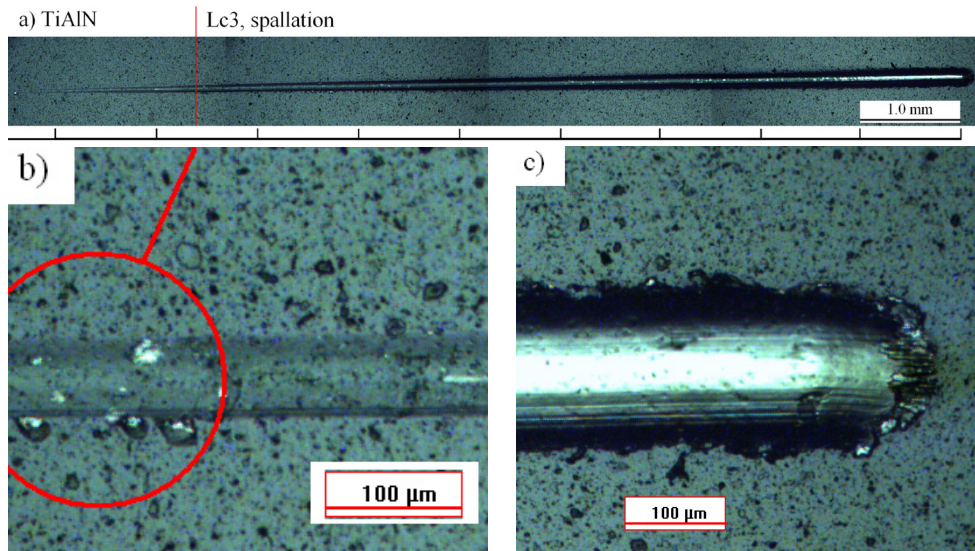


Figure 3.37. Surface cracks generated in scratch test track of TiAlN: a – sledge of the scratch test track, b – irregular coating chipping and spallation at both side of the track edge ($Lc2$ and $Lc3$), and c – a close-up look of the track end tip showing complex failure modes.

AlTiN - G

The surface cracks generated in gradient AlTiN coating are shown in Figure 3.38, a. Figure 3.38, b shows relatively irregular interfacial coating spallation spots (mode $Lc3$) at lower side of the track border. There are angular forward type Chevron cracks that have developed along with the track borders as can be see in Figure 3.38, c. Also chipping spallation of the coating at the track end and sides (white areas) can be seen in Figure 3.38, c. The critical load Lc is considered to be 15 N, i.e. normal load at which first coating failure mode – as through-thickness spallation ($Lc3$) takes place.

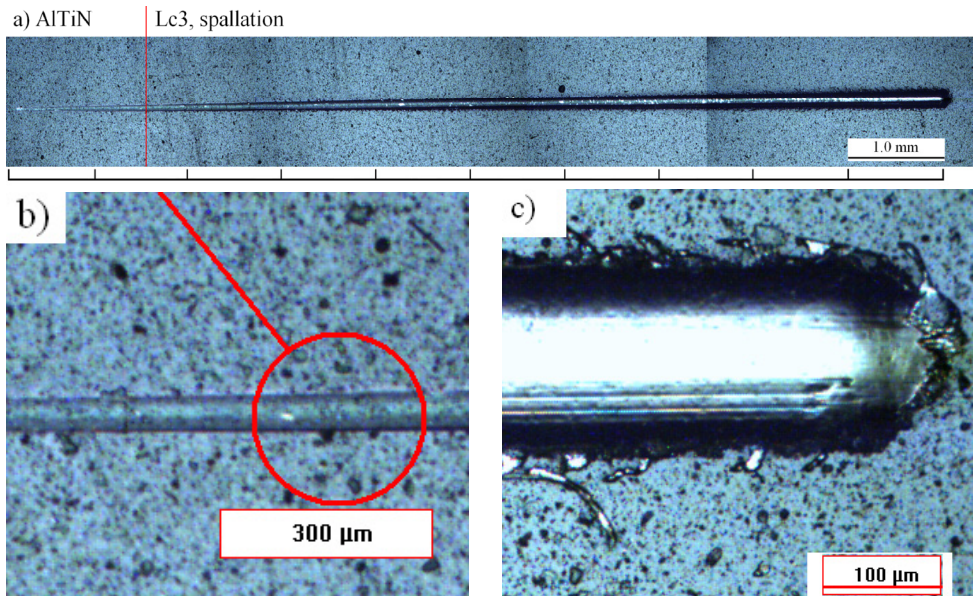


Figure 3.38. Surface cracks generated in scratch test track of AlTiN: a – sledge of the scratch test track, b – irregular coating chipping and spallation at one side of the track edge (*Lc2* and *Lc3*), and c – a close-up look of the track end tip showing complex failure modes.

nACo

In Figure 3.39, a optical microscope images of surface cracks of *nACo* coating are given. Figure 3.39, b shows regular forward direction angular Chevron-type and forward semi-circular type cracks (mode *Lc1*) at both sides of the track borders and in the bottom of the scratch track. Figure 3.39, c shows the further development of angular and semi-circular cracks and start of coating cohesive chipping (buckling) at the track edges (mode *Lc2*). Figure 3.39, d shows the process of semi-circular cracks formation into angular forward-direction Chevron-type cracks as the increasing normal load, directed into the bottom of the crack, divides the semi-circular crack into two parts. Some chipping (buckling) and minor spallation of the coating is also visible at the track edges. In Figure 3.39, e substrate is irregularly exposed (white dots) as the coating is spallating in the bottom of the crack track. The spallation forms after the stylus passes over the failed buckled region, crushing the coating into the surface of the scratched track.

A sledge represented in Figure 3.40 shows the forward-type angular Chevron-type cracks approaching from both sides of the track borders and some parallel cracks being generated along the track borders and wedge crack formed some way ahead of the moving indenter (mode *Lc1*), coating chipping i.e. cohesive buckling (mode *Lc2*) from both sides of the track border is visible. Spallation (mode *Lc3*) of the coating at the track edges (light areas) and gross interfacial shell-shaped spallation

from the bottom of the scratch track is visible as multiple light areas in Figure 3.40. Tip of the stylus is moving from left to right.

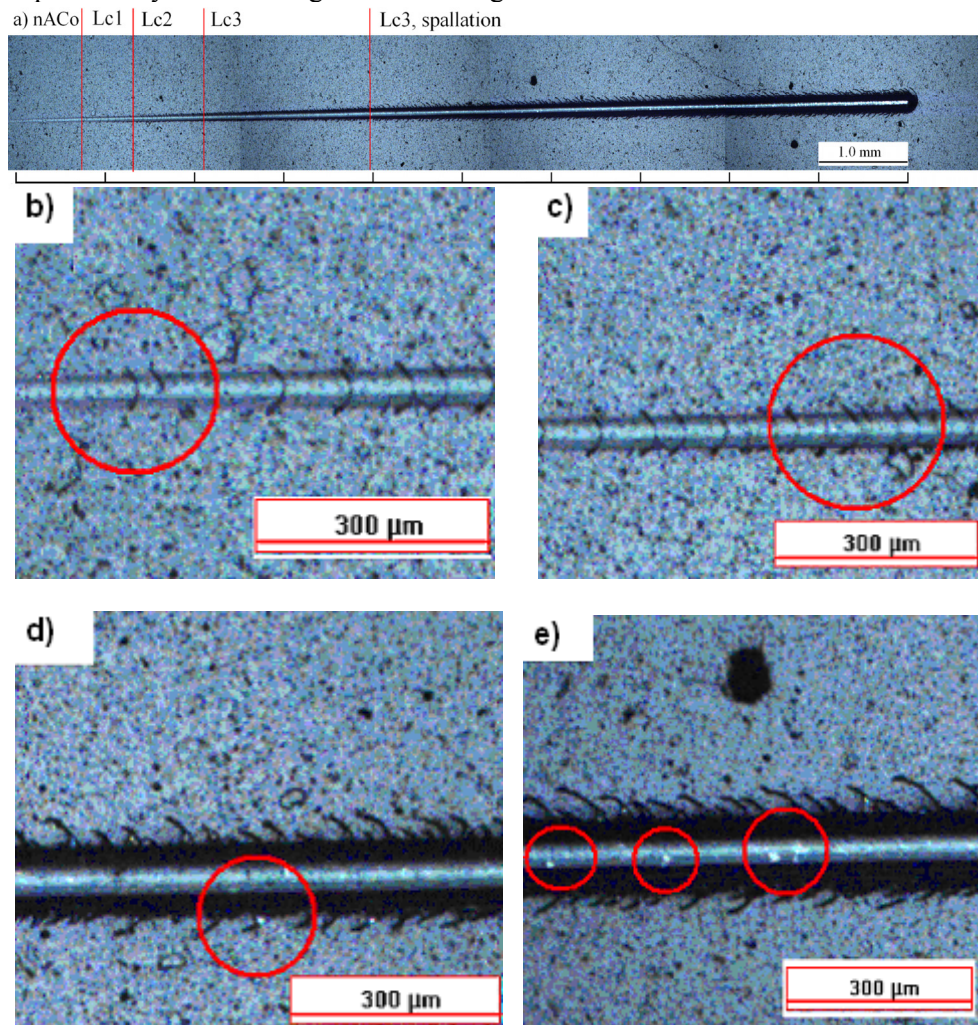


Figure 3.39. Surface cracks generated in scratch test track of nACo coating: a - optical microscope images of surface cracks of nACo coating; b – regular forward-direction angular (Chevron-type) and forward semi-circular type cracks (mode *Lc1*) at both sides of the track borders and in the bottom of the scratch track; c – further development of angular and semi-circular cracks and start of coating cohesive chipping (buckling) at the track edges (mode *Lc2*); d – process of semi-circular cracks formation into angular forward-direction Chevron-type cracks, as the increasing normal load, directed into the bottom of the crack, divides the semi-circular crack into two parts; e – substrate being irregularly exposed (white dots) as the coating is spalling in the bottom of the crack track.

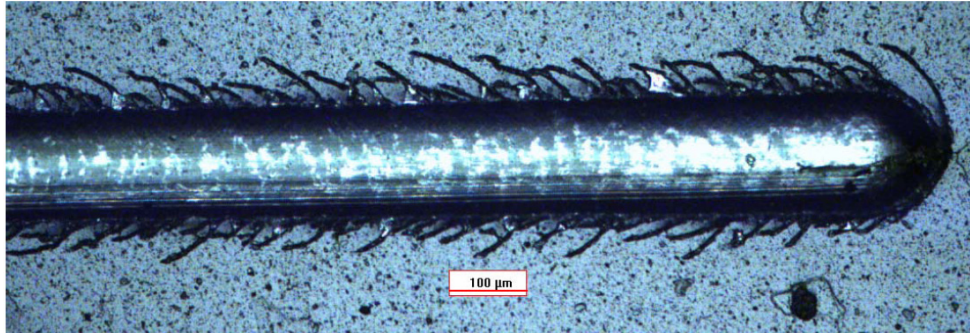


Figure 3.40. A close-up look image of the sledge of the indenter at the end of the scratch test of nACo[®] coating.

Table 3.7. The results of the examination of the scratch track after scratching using an optical microscope

Coating type	Failure modes			
	<i>Lc1</i> , N	<i>Lc2</i> , N	<i>Lc3</i> , N	<i>Lc3</i> spallation, N
TiN	-	-	-	32
TiCN	-	-	-	22
TiAlN	-	-	-	24
AlTiN	-	-	-	15
nACo	8	13	21	39

In response to the compressive stresses generated in front of the moving indenter (ploughing phase), in most cases minor (TiN, TiCN, AlTiN) or moderate cracks (TiAlN, nACo) are formed either on one side or at both side of the track border, also buckling (chipping) occurs. Buckling (plastic pile-up) ahead of the stylus that was recognised as adhesion failure mode, generated adhesion failures inside the track. Buckling failures typically appear as curved cracks, either in transverse or forward angular – Chevron type (TiN, TiCN, TiAlN and AlTiN) or semi-circular type (nACo) extends to the edge of the scratch track and beyond that. As the normal force increases together with the linear movement of stylus, spallation failure mode occurs in all coatings as the scratch stylus passes over the failed region, crushing the coating into the surface of the scratch track [101]. Coatings of lower hardness and higher Young's modulus (lower H/E ratio) withstand the crack propagation without nucleation of long angular – Chevron or semi-circular type cracks (TiN, TiCN, TiAlN and AlTiN), but with some buckling and chipping at track borders and some shorter Chevron cracks. Coatings with high E/H ratio (nACo), having high hardness and low elastic modulus have little resistance to nucleation of long semi-circular cracks, that are into semi-circular cracks as the increasing normal load, directs the stylus into the bottom of the crack. Also, reduced surface roughness tends to decrease to the nucleation of chipping and buckling at track borders.

Adhesion evaluated by Rockwell C - scale test

The results of the indentation test of coatings deposited onto tool steels are presented by micrographs in Figure 3.41 to Figure 3.43. The micrographs of higher magnification are placed aside the main figures to indicate and specify coating cracking according to Table 2.3. The type and the volume of a failure zone indicate to film adhesion and its brittleness, which correspond to the microstructure and the mechanical properties of the coatings. Coatings of higher hardness and lower Young's modulus (high H/E ratio) withstand the load without nucleation of long conical cracks (nACo and TiCN). Higher ratio of H/E means higher elastic recovery ability of a coating [135, 136, 139,]. However, considerable amount of long radial cracks of 10 – 50 μm were generated, causing the exfoliation of coating layers [136, 139] (Class 2). The longest radial cracks are indicated in the TiN coating and numerous enfold and larger in size exfoliations of the coating layer are observed (Figure 3.41 a). It is obvious that radial cracks predispose that kind of coating failure. The same features are seen in the case of TiAlN coating (Class 2) with only difference - the conical cracks are also present (Figure 3.42 a). It seems that short radial cracks accelerate chipping on the bordering area of coating-indenter contact. Emerged chips tend to make connections with the closest on the sides forming the ring or conical crack. The structural defects presented on the surface, such as pores and non-metallic inclusions, simplify this action. Finally, the most drastically fractured case – nACo[®] coating (Class II, Figure 3.43). The worst performance of this coating was indicated by the numerous short radial and closed conical cracks. First, the very brittle structure collapses around the indenter and then starts to take up (absorb) fracture energy by the formation of radial cracks. Eventually those are blunted by the perpendicularly formed conical cracks and are not reaching the last "ring".

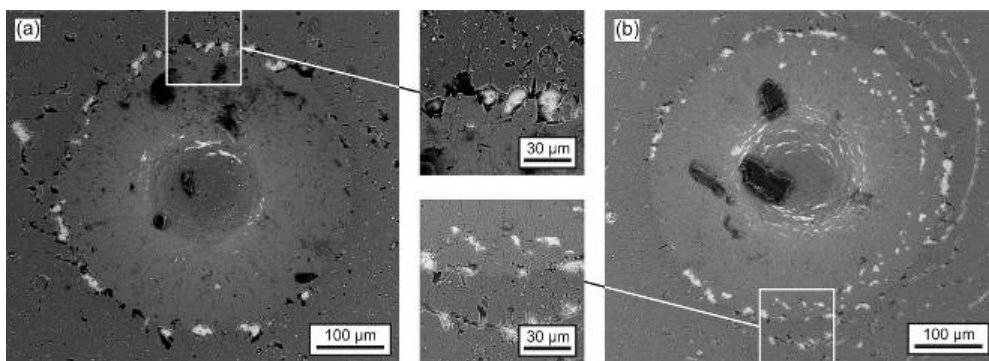


Figure 3.41. SEM micrographs of the imprints of the adhesion test of coatings: a – TiN, and b – TiCN.

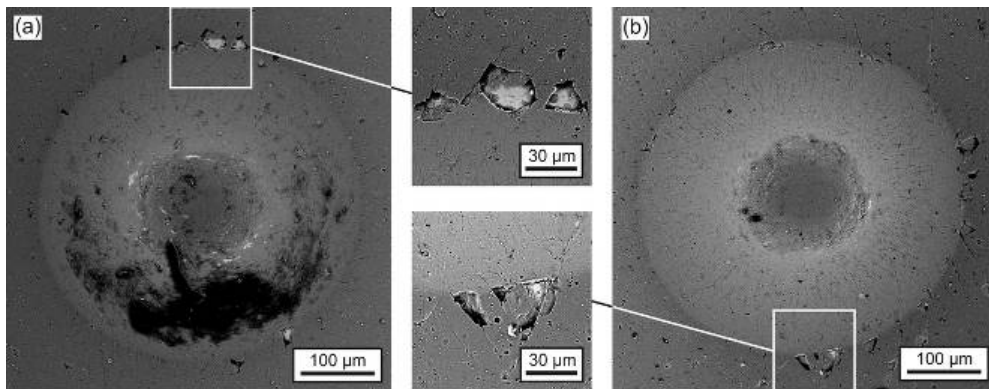


Figure 3.42. SEM micrographs of the imprints of the adhesion test of coatings: a – TiAlN, and b – AlTiN.

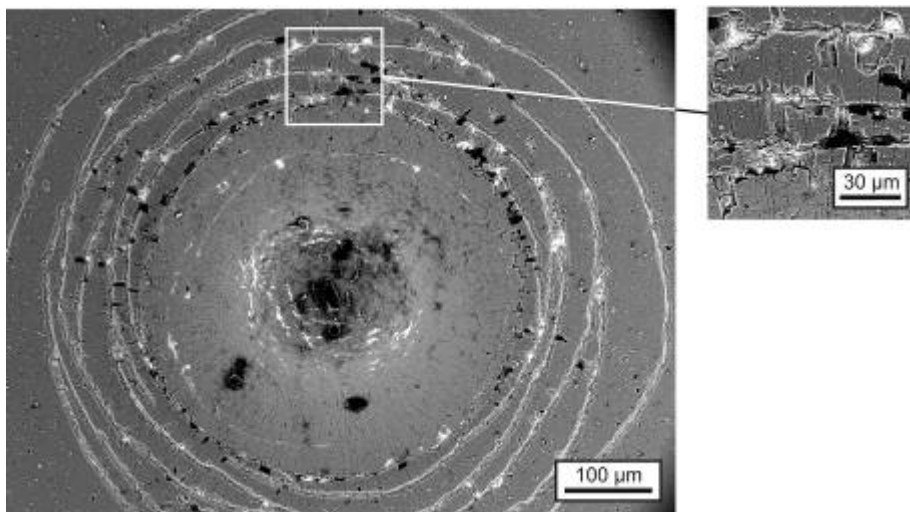


Figure 3.43. SEM micrographs of the imprints of the adhesion test of nACo[®] PVD coating.

PVD coatings deposited onto nitrided steel (Table 2.1), forming a duplex coating system – were also studied. The nitrided layer has a hardness of *ca.* 850 HV0.01 and case depth of approximately 0.3 mm (Figure 3.33). As mechanical properties of substrate play essential role in service condition of tools, especially at high loads, duplex systems behave differently from the case hardened tools steel substrates. As the core hardness of Vanadis 6 or Weartec is much higher than the core hardness of nitrided steel, then severe plastic deformations are expected at higher normal loads. The results of the adhesion tests are presented by micrographs in Figure 3.44. The type and the volume of a failure zone indicate to film adhesion and its brittleness, which correspond to the microstructure and the mechanical properties of the coatings. Higher ratio of H/E means higher elastic recovery ability of a coating [137, 136, 139,].

Again, coatings of higher hardness and lower Young's modulus (higher E/H ratio - TiCN, TiAlN-ML, AlTiN-G, nACo) tend to withstand the load without major adhesive delamination of the coating, but with nucleation of considerable amount of long (100 – 150 μm) radial cracks (Class 1, Figure 3.44 b). However, TiN, having lowest H/E ratio of 0.072, showed nucleation of lot of small conical cracks, causing the partial adhesive delamination of coating that is a typical behavior of TiN coating under loading (Class 2) [138, 139]. It seems that short radial cracks accelerate chipping on the bordering area of coating-indenter contact. Emerged chips tend to make connections with the closest on the sides forming the ring or conical crack. The structural defects presented on the surface, such as pores and non-metallic inclusions, simplify this action.

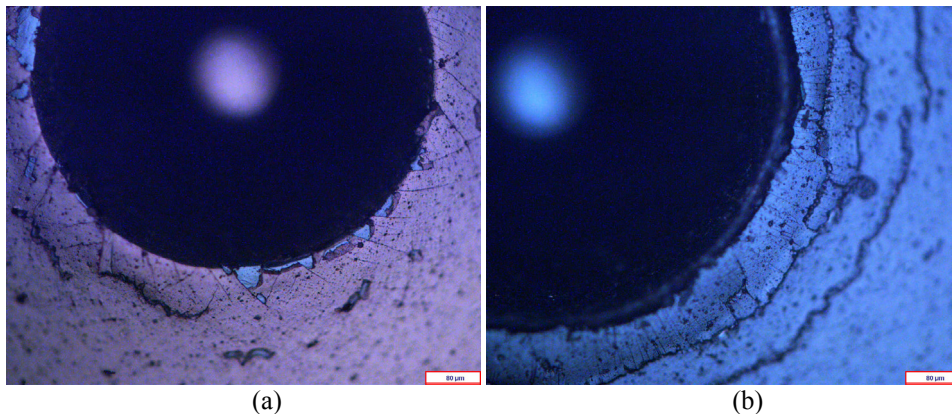


Figure 3.44. Micrographs of the imprints of the adhesion test of PVD coatings on nitrided steel 38CrMoAl8 substrate at 20 x magnification: a – TiN , b – TiAlN

Among all the tested coatings, the TiCN (Figure 3.41 b) seems to be most durable. The mixed failure modes are characteristic of the studied coated system. Most widely presented are cohesive (chipping caused by the normal component of a stress tensor) and the delamination with buckling and fracture mode (decohesion of a coating with the formation of microcracks, caused by a combination of shear and normal stresses).

Cracking resistance and surface fatigue

Cracking resistance and fatigue properties of five hard PVD coatings - TiN, TiCN, TiAlN-ML, AlTiN-G and nanocomposite nACo® (nc-AlTiN/a-Si₃N₄) on tool steels Weartec™ and Vanadis 6 are evaluated by means of the cyclic Vickers indentation and dynamic compressive stresses method. The analytical part covers an evaluation of damage evolution of the coated system versus the number of cycles. The effect of mechanical response – ratio E/H on the crack propagation is described in the form of a diagram with various curves, each one associated with a certain number of indentation cycles. The comparative adhesion testing was

conducted with the use of the Rockwell C technique (above). It was found that the type of cracks formed in the coated systems under cyclic loading is dependant on the H/E ratio values. The data obtained enable the cracking and fatigue resistance of the coated system to be compared and an optimal coating for metal forming tools applications to be selected.

The results of cyclic indentation are given in Table 3.8. At indentation after the first indentation cycle, mostly contact region model of coating deformation was presented due to the high indenting load of 500 N applied. With TiCN, no cracks at all or weak secondary radial cracks were observed in the corners of the impression (Figure 3.46 a). To estimate the cracking resistance of the coated system, a quantitative analysis of the samples was performed. The lengths of radial cracks from the impression corner were measured and presented on graphs (Figure 3.45) vs. the number of indentation cycles. The error bars show the standard deviation of 2.3 μm .

Table 3.8. Crack types and crack evaluation criteria for coatings deposited on CWTS steels, based on cyclic Vickers indentation.

Coating / Substrate	Number of indentation cycles					
	1	10	50	100	1000	10000
TiN / Weartec™	I	I	I	I, II	II	IV
TiN / Vanadis 6	I	I	I	I	II	IV
TiCN / Weartec™	0, I	0, I	0, I	I	I	III
TiCN / Vanadis 6	0	0	0	0, I	0, I	II
nACo® / Weartec™	I	I, II Starting delamination	II Starting delamination	II Starting delamination	V  Cone crack	V  Cone crack
nACo® / Vanadis 6	0	I Starting delamination	V  Cone crack	V  Cone crack	V  Cone crack	V  Cone crack
TiAlN / Weartec™	0, I	I	I	I, II	II, III	VI
AlTiN / Weartec™	I	I	I	I	II	VI

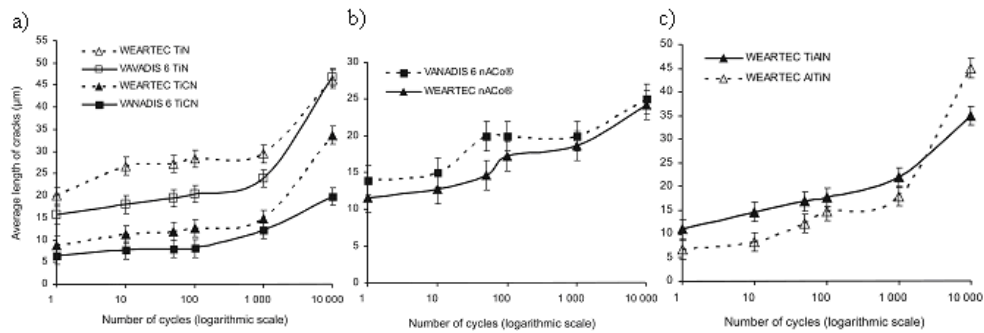


Figure 3.45. Dependence of average length of radial cracks on Weartec and Vanadis 6 substrates on the number of indentation cycles: a – TiN and TiCN; b – nACo, and c – dependence of average length of radial cracks on the number of indentation cycles of TiAlN and AlTiN on Weartec substrate.

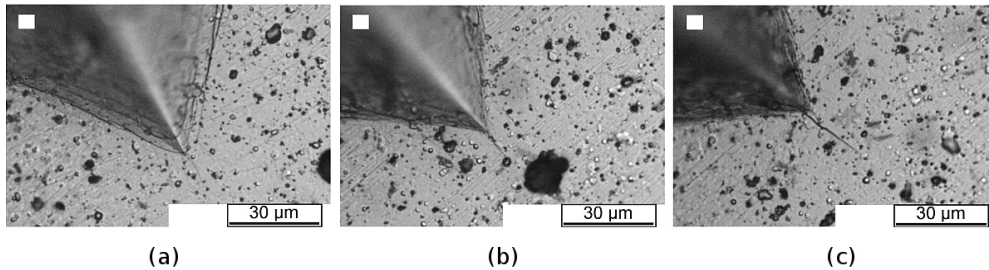


Figure 3.46. Impression corner of TiCN coating on Vanadis 6 substrate with the appearance of: a – 0 criteria after 1 cycle; b – I criteria after 1000 cycles, and c – II criteria after 10 000 cycles.

Similarly to the single loading of the adhesion test, TiCN-MP coating on both substrates had the best cracking resistance at all cycle values (Figure 3.45). TiCN on Vanadis 6 showed radial cracks with length a of 20 µm and crack evaluation criteria II (Figure 3.45, a; Figure 3.46, a). On the contrary, microlaminate nACo® on both substrates had the lowest cracking resistance (Figure 3.47, c). The cracking of this coating differed from others with the formation of cone cracks around the impression, in addition to radial cracks and delamination of the coating at indent impression corners validating the results of the adhesion test (Figure 3.43).

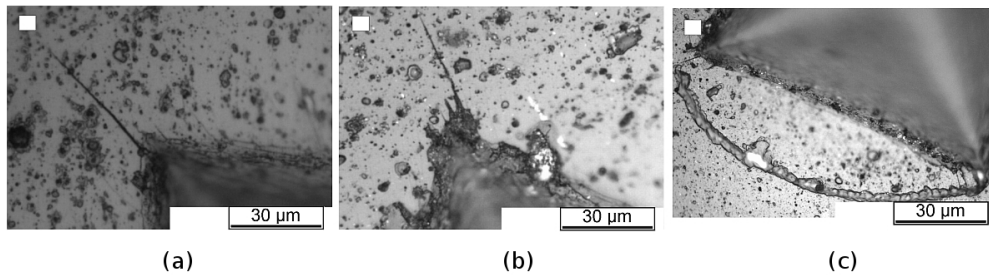


Figure 3.47. Impression corner of coatings on Wearthec™ after 10 000 cycles with the appearance of: a – IV criteria by TiN; b – VI criteria by AlTiN, and c – V criteria by microlaminate nACo®.

The above given allows us to make a hypothesis that the crack type and cracking resistance of a cyclic loaded coated system is in dependence on the coating E/H ratio. Radial cracking without delamination was observed in coatings with the highest E/H ratio (TiCN and TiN) and the lowest values of E/H (nACo®) showed cone cracking and delamination. The dependence between radial cracking sequence and E/H ratio values was described in the form of a diagram (Figure 3.48). Each curve on the diagram is associated with a certain number of indentation cycles. According to the diagram curves, TiAlN has medium and AlTiN strong radial cracks after 10 000 cycles. Both coatings showed delamination of the coating around the corners of the impression. TiAlN was less damaged and it had higher E/H ratio than AlTiN (Figure 3.47, b). In addition, cyclic indentation test revealed that multilayer coatings are preferable over monolayer TiN coating with one of the lowest cracking resistance and the formation of strong radial cracks with the length of about 47 µm despite high E/H ratio of TiN (Figure 3.47, a).

The "quasi-plastic" damage mode prevailed as the Vickers diamond pyramid was used in the indentation test. In contrast to spherical indenters, a sharp indenter penetrates easily into the coating surface and cone-cracking formation is suppressed by the radial cracks nucleation.

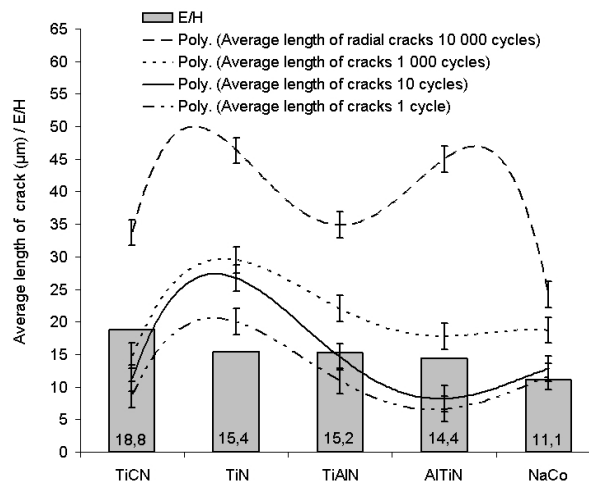


Figure 3.48. The effect of the E/H ratio on the radial crack propagation (substrate – Weartec™).

Radial cracks become the dominant mode of indentation fracture and lead to accelerate cracking resistance degradation of the coating. Fracture analysis revealed that apart from other coatings, in nAlCo® the "brittle" damage mode occurred with the formation of cone cracks, driven by tensile stresses in addition to "quasi-plastic". On the other hand, the obscured subsurface damage and the formation of radial cracks could be found below cone cracks.

The best cracking resistance of TiCN can be also explained by good adhesion due to the presence of the carbides in both substrates. Crystallographic similarity of the substrate and the coating seem to have an effect, ensuring strong bonding between them. The observations of both substrates coated with TiCN expose the advantages of PM CWTS Vanadis 6 over Weartec™, as it has higher Young's module. It is assumed that Vanadis 6 works like a spring under the coating, allowing it to bend and deform (fracture) according to the contact region wear model described above.

In addition, smaller carbide size in Vanadis 6 and more uniform carbides distribution hampers the nucleation and propagation of cracks and delamination of the coating. However, Vanadis 6 as a substrate for TiN and nAlCo® did not show benefits over Weartec®.

Thin hard PVD coatings often are not able to work in conditions of high loads on a relatively soft substrate material. To wide the application areas (not only applied on substrates as cermets and high-speed steels), one of the prospective ways is to use ion nitriding technique (also referred as plasma nitriding) with following hard PVD coatings (duplex coatings) on nitriding steels [139]. Ion nitrided nitriding steel 38CrMoAl8 is used as substrate in following study. Hardness distribution in case

depth of this steel given in Figure 3.33 shows that the core microhardness of the plasma nitrided substrate is 350 HV0.01 and the microhardness of the nitrided surface layer, having case depth of 300 μm , is around 850 HV0.01. The number of indentation cycles and total applied indenting load remain the same as it was used for the previous study with CWTS. Similarly, the optical microscope Axiovert 25 (Zeiss) with magnifications of 100 X and 500 X and Buehler Omnimet Image Analysis System 5.40 including the package for crack length measurement (Palmqvist method, [140]) was used.

Cracking resistance and fatigue properties of eight different hard PVD coatings - TiN, TiCN-MP, mono - and microlaminate TiAlN, gradient AlTiN, microlaminate nanocomposite nACo® (nc-AlTiN/a-Si₃N₄), and multilayer nanocomposite nACo® (nc-AlTiN/a-Si₃N₄) plus TiN coating on top of nitrided steel and uncoated nitrided steel 38CrMoAl8 are evaluated by means of the cyclic Vickers indentation method. The analytical part covers an evaluation of damage evolution of the coated system vs. the number of cycles. The effect of mechanical response - Young's modulus/Hardness ratio (E/H ratio or H/E ratio) of the coating on the crack propagation is described in the form of a diagram with various curves, each one associated with a certain number of indentation cycles. It was found that the type of cracks formed in the coated systems under cyclic loading is dependant on the H/E ratio. At indentation after the first indentation cycle, mostly contact region model of coating deformation was presented due to the high indenting load of 500 N applied. The increase of indentation cycles leads mostly to mixed failure mode.

With uncoated nitrided steel 38CrMoAl8, where the hard nitrided layer has hardness gradient increasing from the microhardness of the core material of 350 HV0.01 to a maximum microhardness of 850 HV0.01 of the top nitrided layer (Figure 3.33), no cracks at all appeared before indentation cycle of 50 (Figure 3.49 a). After the number of indentation cycles reached a sum in between 50 – 100 cycles, a hard brittle nitrided layer formed on a upper surface (at depth of maximum of ca. 300 μm) of the soft material, a formation of strong radial cracks with length of 50 – 100 μm started to propagate (Figure 3.49 b to Figure 3.49 d) along the corners of the indentation imprint. Such radial fatigue cracks are common to “quasi-plastic” damage mode, which is typical for low H/E ratio coatings, resulting low elastic recovery ability [135]. The H/E ratio for nitrided steel is 0.008 (Table 3.9).

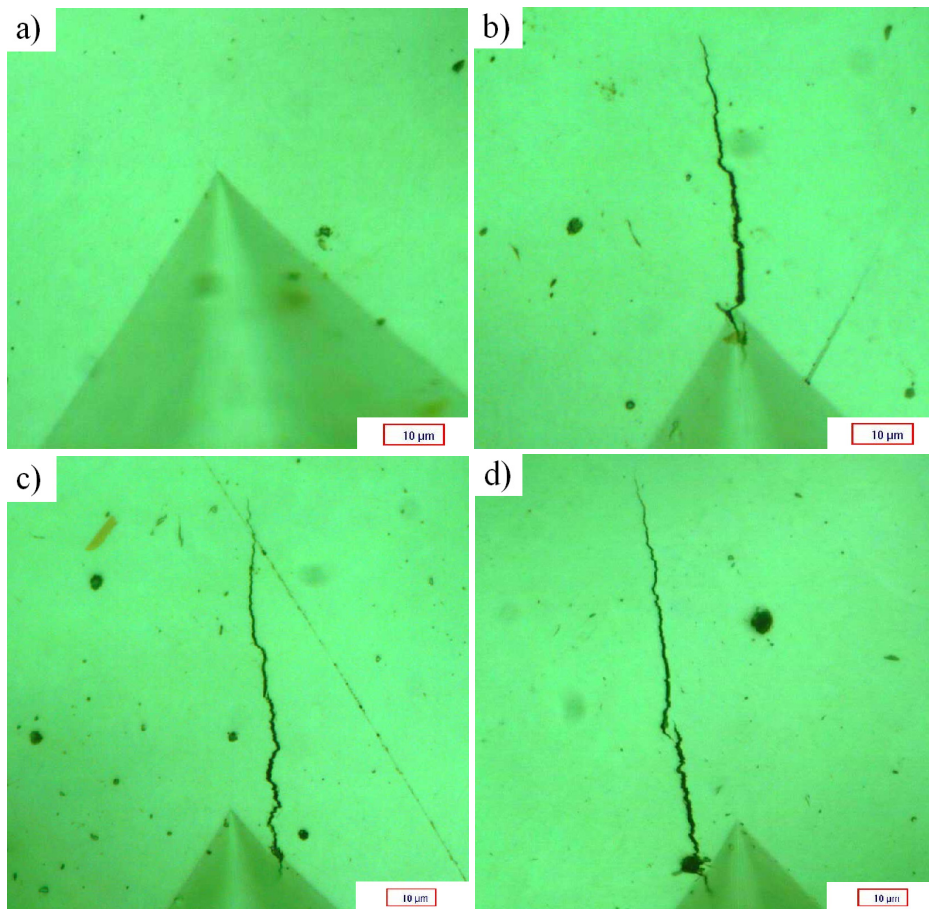


Figure 3.49. Impression corner of the surface of nitrided steel substrate with the appearance of: a – 0 criteria after 50 cycles, and b – IV criteria after 100 cycles; c – IV criteria after 1000 cycles, and d – IV criteria after 10000

TiN coating, deposited on nitrided steel 38CrMoAl8 (Figure 3.50), withstand the loads without nucleation of long radial cracks, resulting crack evaluation criteria II (Table 2.4). TiN has the lowest H/E ratio of the deposited coatings, which result in poor elastic recovery ability of the coating. The H/E ratio of TiN is 0.072 (Table 3.9). However, only considerable amount of radial cracks with length of 20 – 50 µm (Figure 3.50 a - Figure 3.50 f) were formed and caused numerous exfoliation and enfolds of the coating layers (Figure 3.50 e and Figure 3.50 f), which is typical to TiN coating. Indentations at lower normal loads (normal load at 100N) results less plastic deformation in substrate; fewer and smaller cracks; less exfoliation and enfolds of the coating layers (Figure 3.50 g, h).

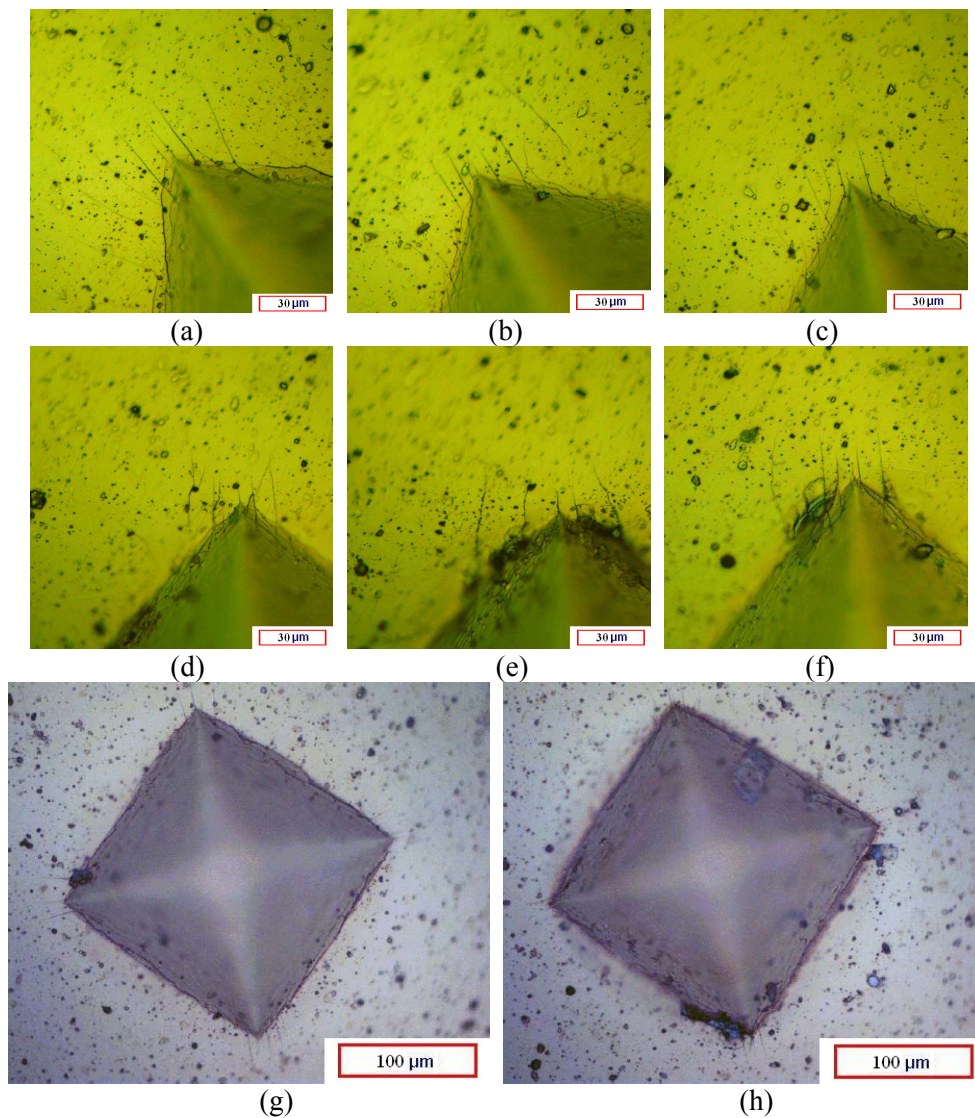


Figure 3.50. Impression corner of the surface of nitrided steel substrate coated with TiN with the appearance of: a – II criteria after 1 cycle; b – II criteria after 10 cycles; c – II criteria after 50 cycles; d – II criteria after 100 cycles; e – II criteria after 1000 cycles, and f – II criteria after 10000 cycles; g – I, II criteria after 1000 cycles at indentation load of 100N; h – II criteria after 1000 cycles at indentation load of 100N.

The TiCN coatings have the second highest hardness (Table 3.5) and second highest surface roughness value (Table 3.3), but exhibited poor adhesion qualities. The poor adhesion quality is can be related to the higher inherent residual stresses of TiCN coatings (Table 3.12). Few short radial cracks and small number of exfoliation and enfolds of the coating layers appeared along the corners of the

indentation imprint during the first indentation (Figure 3.51 a). After the number of indentation cycles the length of the cracks reached a length in between 30 – 50 μm (Figure 3.51 b - Figure 3.51 d). Such radial fatigue cracks, without total delamination of the coating is observed in “quasi-plastic” damage mode.

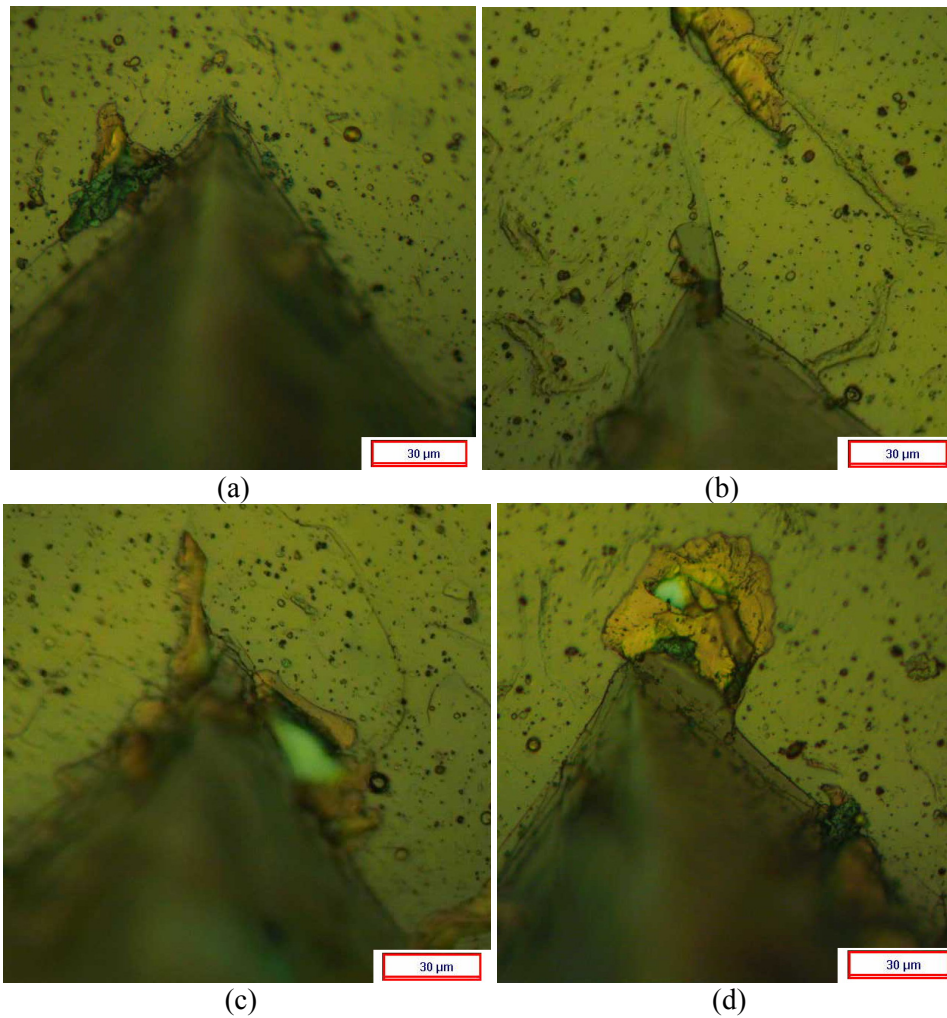
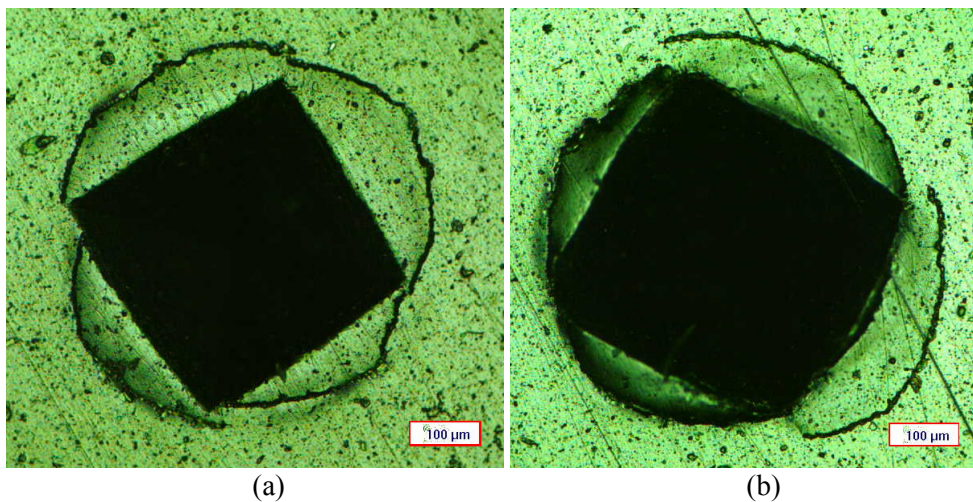


Figure 3.51. Impression corner of the surface of nitrided steel substrate coated with TiCN with the appearance of: a – I and II criteria after 1 cycle; b – I and II criteria after 50 cycles; c – III criteria after 1000 cycles; d – VI criteria after 10000 cycles;

Nitriding treatment causes compressive subsurface stresses, that in combination with compressive residual stresses within the coating, cause lower tensile stresses in the indenter-loaded area. TiCN have the second highest H/E ratio, which result in greater elastic recovery ability of the coating at low loads. The H/E ratio of TiCN is 0.090 (Table 3.9). Despite the high H/E ratio of TiCN, that would

normally cause the nucleation of cone cracks and cause partial delamination of the coating, cone cracks formation was suppressed by the radial cracks nucleation with minor delamination around the impression, resulting lower elastic recovery ability of TiCN.

TiAlN microlaminate coating has the second lowest nanohardness value (Table 3.5), but exhibited different crack propagation mode (Figure 3.58). From the first indentation till the high number of indents (10^4) – “brittle” damage mode was revealed with the formation of cone and small number of radial cracks (Figure 3.52 a and Figure 3.52 b). The depths of the imprints of low and high cycle indents are different – high cycle indents are mostly characterized with deeper imprints due to the increased plastic deformation of the substrate (Figure 3.52 d). Such cone cracks are common to “brittle” damage mode, which is typical for high H/E ratio coatings. The H/E ratio of TiAlN is 0.088 (Table 3.9). Indentation at lower loads (*e.g.* 100 N) results different crack propagation mode (Figure 3.52 e, f). The “brittle” damage mode is changed to a “quasi-plastic” damage mode. Now, the coating can withstand indentation loads without nucleation of conical cracks, resulting only small amount of secondary radial and weak radial cracks with length of 20 – 40 μm (Figure 3.52 e). However, the nucleation of numerous exfoliation and enfold of the coating layers at the corners of indentation imprints can be explored (Figure 3.52 f).



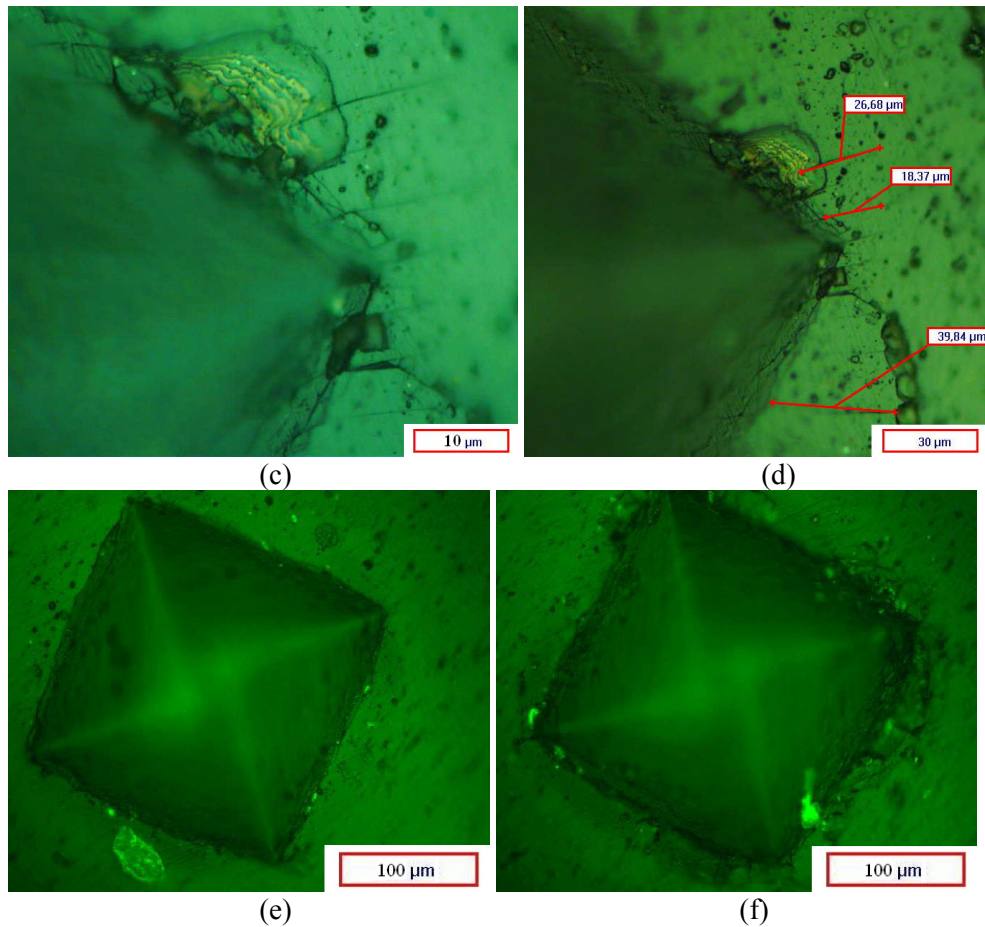
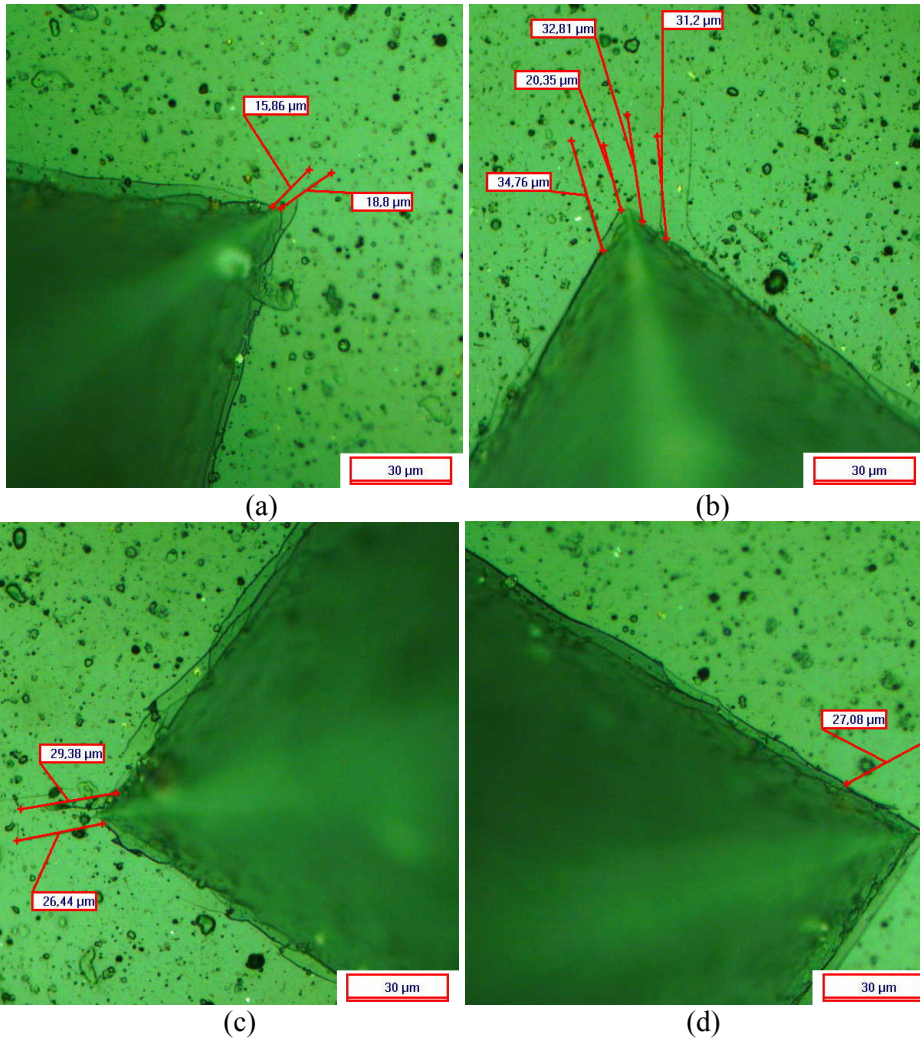


Figure 3.52. Impression corner of the surface of nitrided steel substrate coated with microlaminate TiAlN with the appearance of: a – V criteria after 1 cycle; b – V criteria after 10000 cycles; c and d – nucleation of a cone (ring – type) cracks at the periphery of the imprint and revealing the microlaminate architecture of the coating; e – II and III criteria after 1000 cycles at indentation load of 100 N; f – II and III criteria after 10000 cycles at indentation load of 100 N.

TiAlN monolayer coating has the second lowest nanohardness value (Table 3.5), but exhibited different crack propagation mode from the TiAlN microlaminate coating. Monolayer TiAlN can withstand the indentation loads without nucleation of conical cracks, resulting considerable amount of radial cracks with length of 20 – 40 μm (Figure 3.53 a - Figure 3.53 d), which is similar to crack evaluation criteria II (Table 2.4). Such radial fatigue cracks are common to “quasi-plastic” damage mode, which is typical for low H/E ratio coatings. TiAlN monolayer coating has the second lowest H/E ratio, which result in lower elastic recovery ability of the coating. The H/E ratio of TiAlN is 0.088 (Table 3.9). However, the elastic recovery ability can further be improved at lower indentation loads (*e.g.* 100

N), resulting only weak secondary radial cracks with length of 10 – 15 μm (Figure 3.53 e, f).



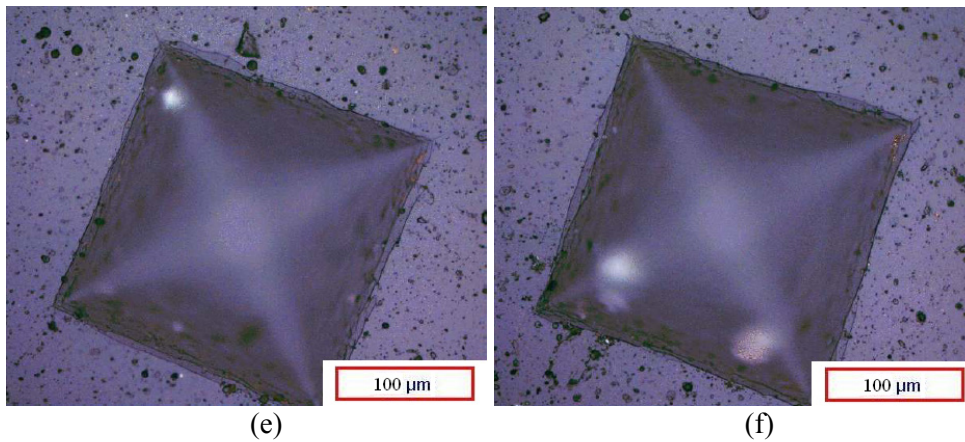
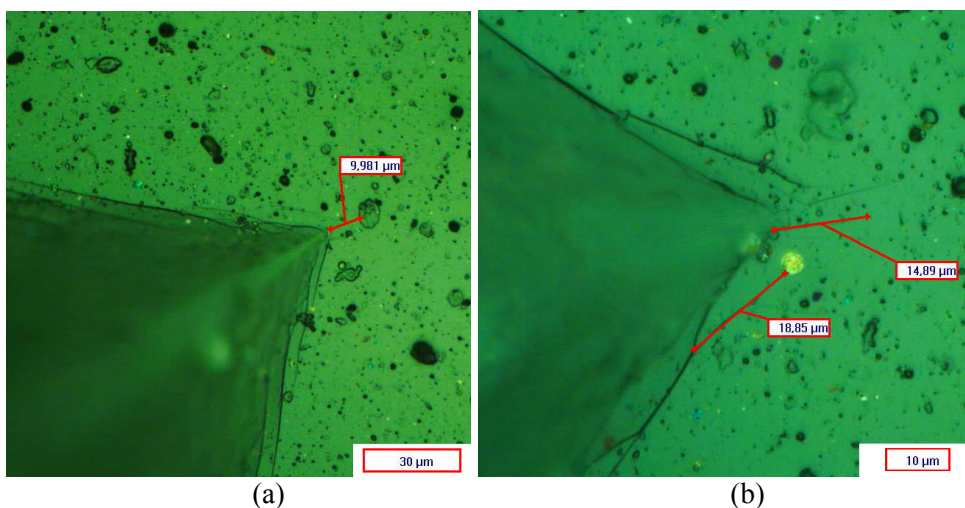


Figure 3.53. Impression corner of the surface of nitrided steel substrate coated with monolayer TiAlN with the appearance of: a – 0 and I criteria after 1 cycle; b – II criteria after 100 cycles; c – II criteria after 1000 cycles; d – II criteria after 10000 cycles; e – 0 and I criteria after 1000 cycle at indentation load of 100N; f – 0 and I criteria after 10000 cycle at indentation load of 100 N.

Gradient AlTiN coating has the third lowest nanohardness value (Table 3.5), and has the highest surface roughness values (Table 3.3). Gradient AlTiN withstands the loads without nucleation of conical cracks, resulting considerable amount of radial cracks with length of 10 – 20 μm , which is similar to crack evaluation criteria III (Table 2.4). Such radial fatigue cracks are common to “quasi-plastic” damage mode, which is typical for low H/E ratio coatings. Gradient AlTiN coating has the third lowest H/E ratio, which result in low elastic recovery ability of the coating. The H/E ratio of TiAlN is 0.089 (Table 3.9).



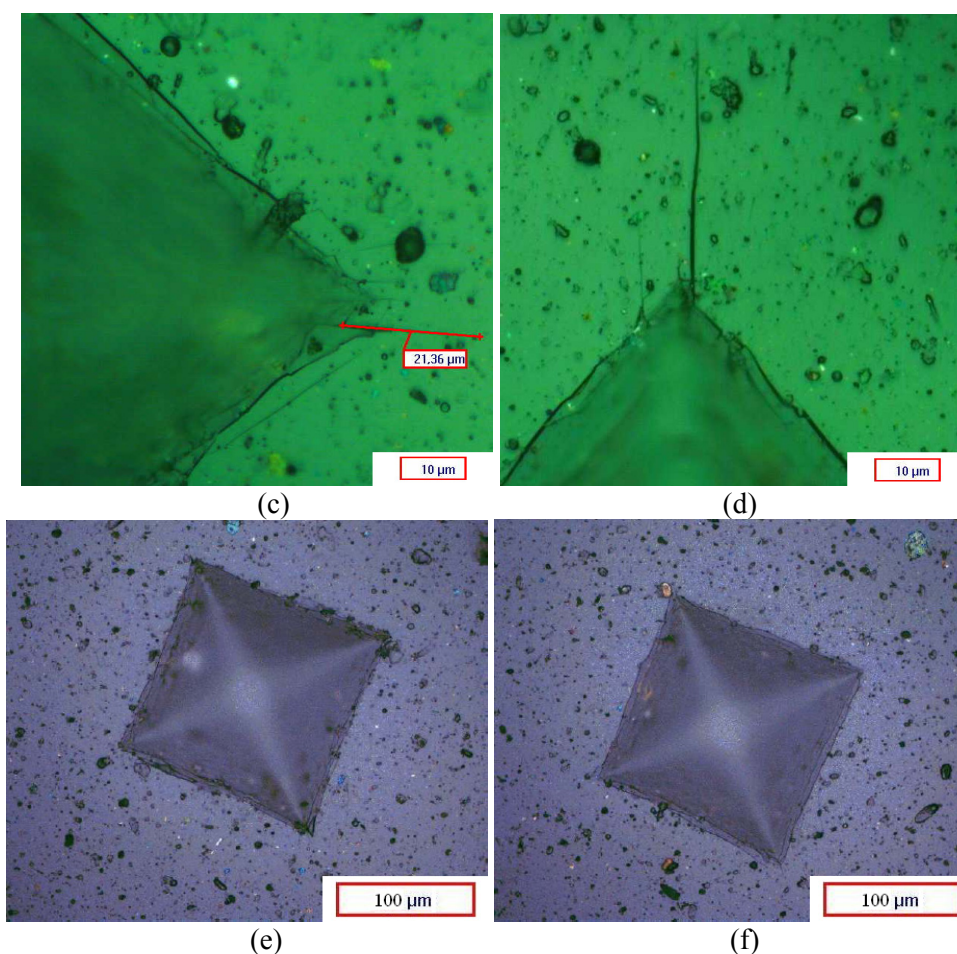


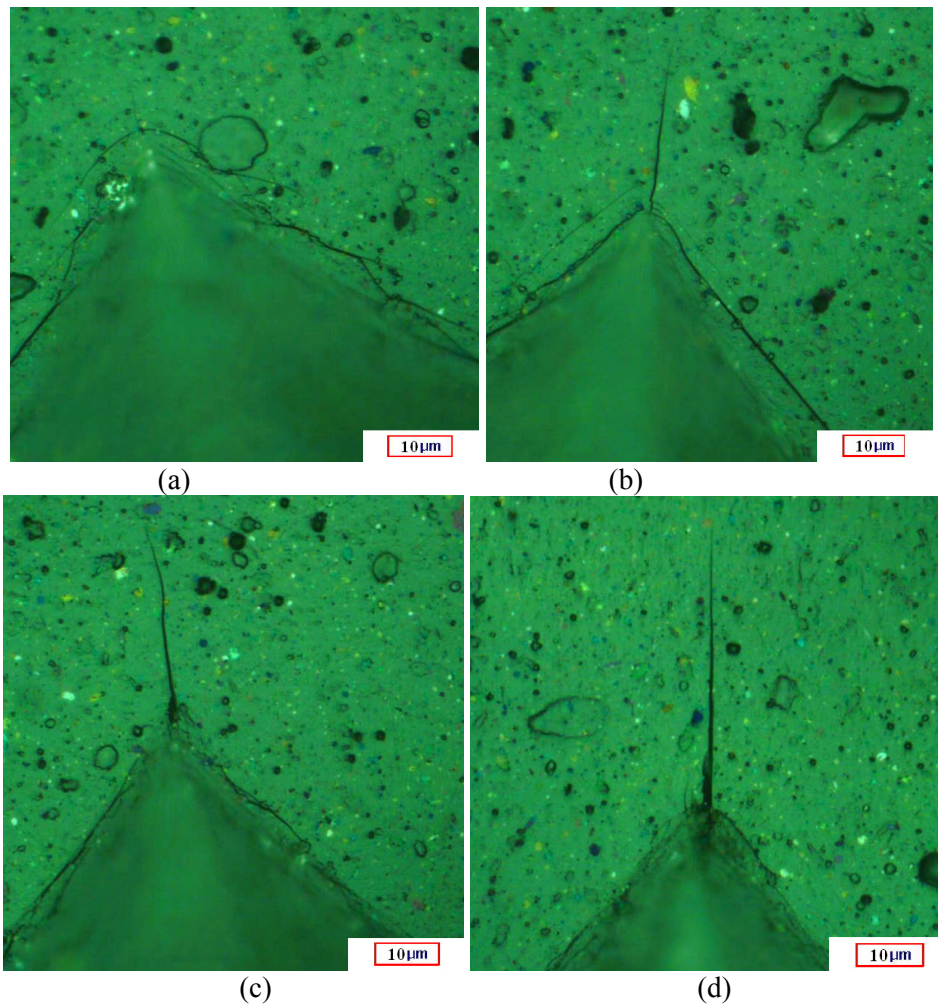
Figure 3.54. Impression of a corner of the surface of nitrided steel substrate coated with gradient AlTiN with the appearance of: a – 0 and I criteria after 1 cycle, b – II criteria after 100 cycles; c – II criteria after 1000 cycles; d – III criteria after 10000 cycle; e – I criteria after 1000 cycles at 100 N indentation load; f – II criteria after 10000 cycles at 100 N indentation load.

However, the elastic recovery ability of gradient AlTiN coating can further be improved using lower indentation loads (*e.g.* 100 N), resulting only weak secondary radial cracks with length of 5 – 10 μm (Figure 3.54 e, f), that are qualified to II crack propagation evaluation criteria.

Gradient nACo coating belongs to the set of nanocomposite coatings and has the highest nanohardness value (Table 3.5). All nACo® coatings showed the highest hardness values and also have a low modulus values, which makes them the best candidate for wear resistant applications. Gradient nACo withstands the loads without nucleation of conical cracks, resulting only few small to medium

secondary radial cracks and medium radial cracks with length of 10 – 30 μm , which is similar to crack evaluation criteria III (Table 2.4). Such radial fatigue cracks are common to “quasi-plastic” damage mode, which is typical for low H/E ratio coatings, however the gradient nACo coating has the highest H/E ratio, which result in high elastic recovery ability of the coating during. The H/E ratio of gradient nACo is 0.144 (Table 3.9).

However, the elastic recovery ability of gradient nACo coating can further be improved using lower indentation loads (*e.g.* 100 N), resulting only small number of secondary radial cracks and few weak radial cracks with length of 5 – 10 μm (Figure 3.55 e, f), that are qualified to II crack propagation evaluation criteria.



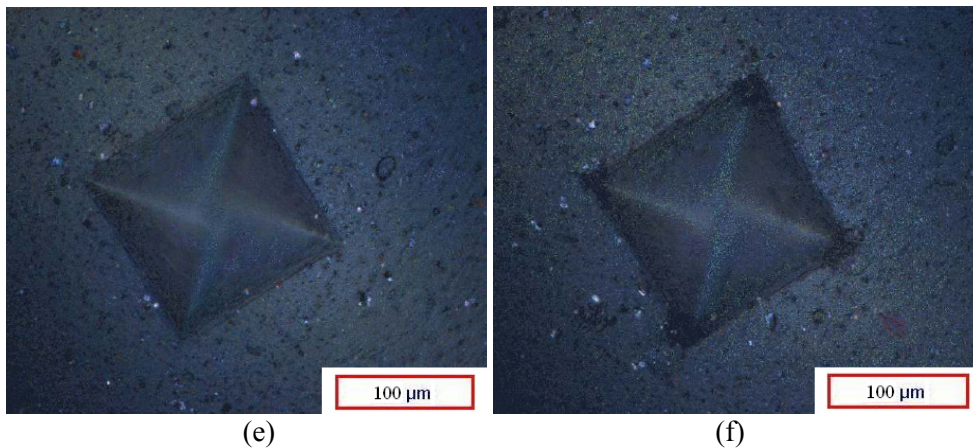


Figure 3.55. Impression of a corner of the surface of nitrided steel substrate coated with gradient nACo coating with the appearance of: a – 0 and I criteria after 1 cycle; b – I criteria after 10 cycles; c – II criteria after 1000 cycles, and d – III criteria after 10000 cycles; e – I criteria after 1000 cycles at 100 N indentation load; f – II criteria after 10000 cycles at 100 N indentation load.

Microlaminate nACo coating belongs to the set of nanocomposite coatings and has the highest nanohardness value (Table 3.5). All nACo® coatings showed the highest hardness values and also have a low modulus values, which makes them the best candidate for wear resistant applications. Microlaminate nACo shows radial cracking around the corners of the impression after 1st indentation (Figure 3.56 a), which accelerate chipping on the corners of the imprint at 100 indentations (Figure 3.56 b). At 1000 and 10000 the increase of the number of indentation cycles leads to partial delamination of the coating at the corners of the indent impression (Figure 3.56 c). In Figure 3.56 d, a nucleation of a strong radial crack under the delaminated coating has been exposed (similarly to Figure 3.49), also possibly being partially the cause of the delamination of the coating due to the substrate “quasi-plastic” deformation induced stresses. Such coatings radial fatigue cracks are common to “quasi-plastic” damage mode of the coating, which is typical for low H/E ratio coatings.

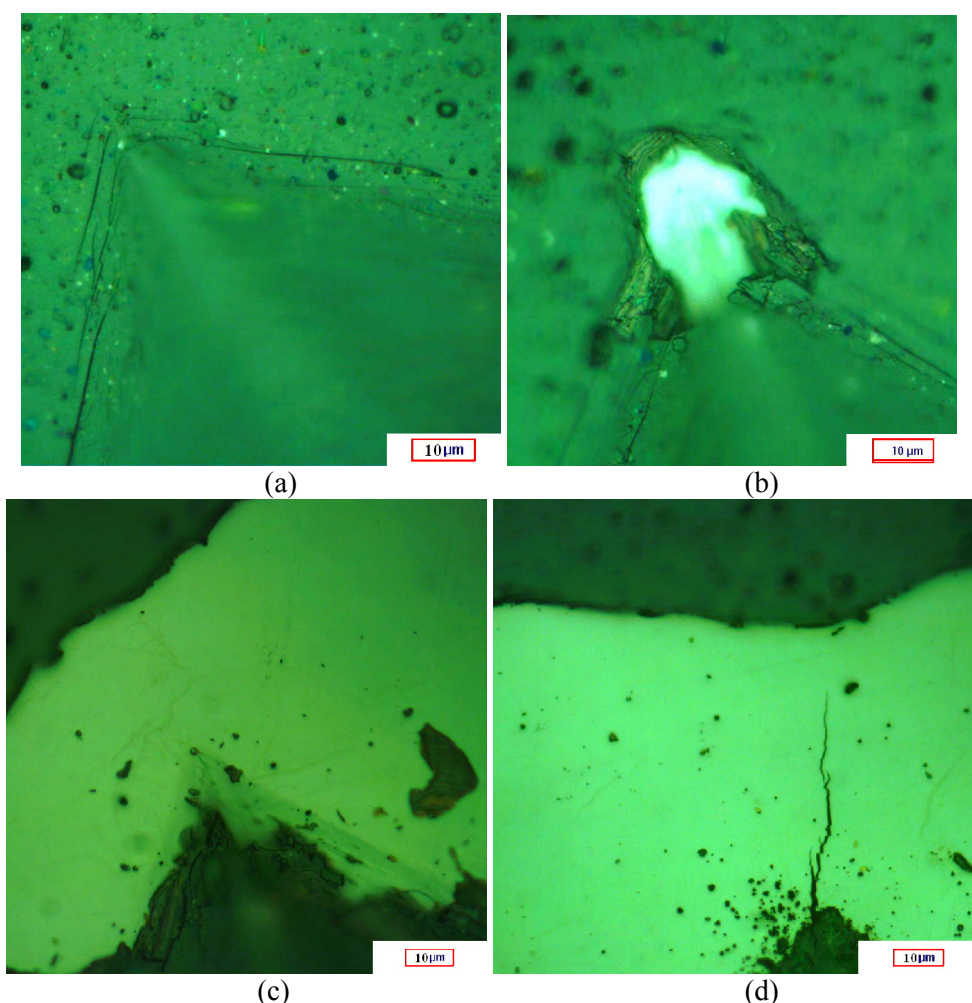
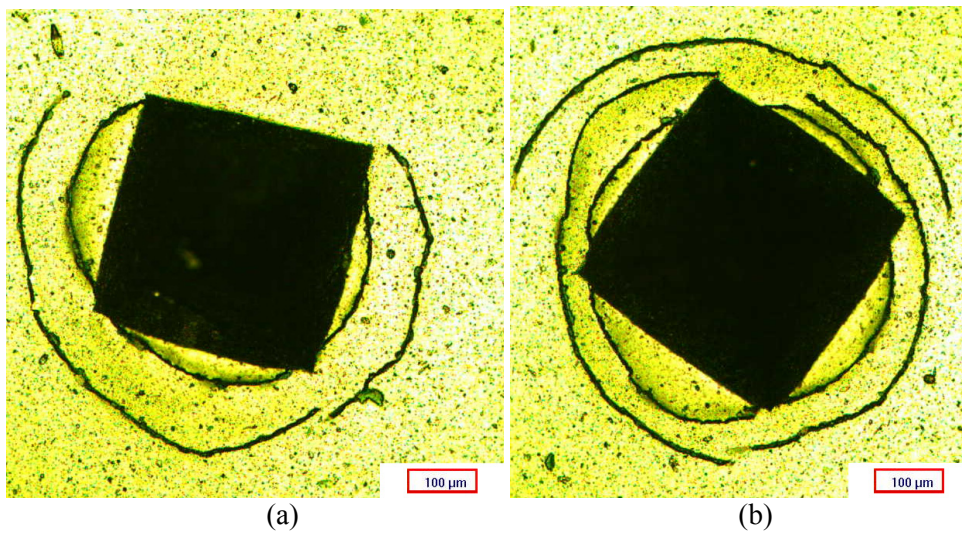


Figure 3.56. Impression of a corner of the surface of nitrided steel substrate coated with microlaminate nACo coating: a – 0 and I criteria after 1 cycle; b – VI criteria after 10 cycles; c – VI criteria after 100 cycles showing coating delamination; d – VI criteria after 1000 cycles showing coating delamination and substrate crack.

Gradient multilayer “nACo gold” coating has the composition of gradient nACo coating with the addition of TiN coating on top of the nACo coating, hence the appearance of TiN. When gradient nACo coating withstand the loads without the nucleation of conical cracks, resulting only few radial cracks with length of 10 – 30 μm , which were similar to crack evaluation criteria II (Table 2.4). Such radial fatigue cracks are common to “quasi-plastic” damage mode, which is typical for low H/E ratio coatings. With the addition of TiN layer to the top coating of gradient nACo the nucleation of conical cracks appeared. From the first indentation till the high number of indents (10^4) – “brittle” damage mode was revealed with the formation of cone cracks (Figure 3.57) and small number of radial cracks at the

corners of the imprints. The depths of the imprints of low and high cycle indents are different – high cycle indents cause severe plastic deformation of the substrate (Figure 3.57 c, d). Such cone cracks are common to “brittle” damage mode, which is typical for high H/E ratio coatings. TiN has the lowest H/E ratio, which should result in poor elastic recovery ability of the coating. The H/E ratio of TiN is 0.072. The H/E ratio of the gradient nACo is 0.144. Probably the addition of TiN layer must have changed the hardness and elastic modulus ratio closer to the region of TiAlN microlaminate (Figure 3.58) – i.e. to a 0.088, resulting the turn of nACo coating failure mechanism from “quasi-plastic” to “brittle” damage mode, resulting improved cracking resistance.

However, lower indentation loads (*e.g.* 100 N) result different crack propagation mode (Figure 3.57 e, f). The “brittle” damage mode is changed to a more common to “quasi-plastic” damage mode. Now, the coating can withstand indentation loads without nucleation of conical cracks, resulting only few number of secondary radial cracks with length of 10 μm (Figure 3.57 e). However, the nucleation of numerous exfoliation and enfold of the coating layers at the corners of indentation imprints can be explored (Figure 3.57 f).



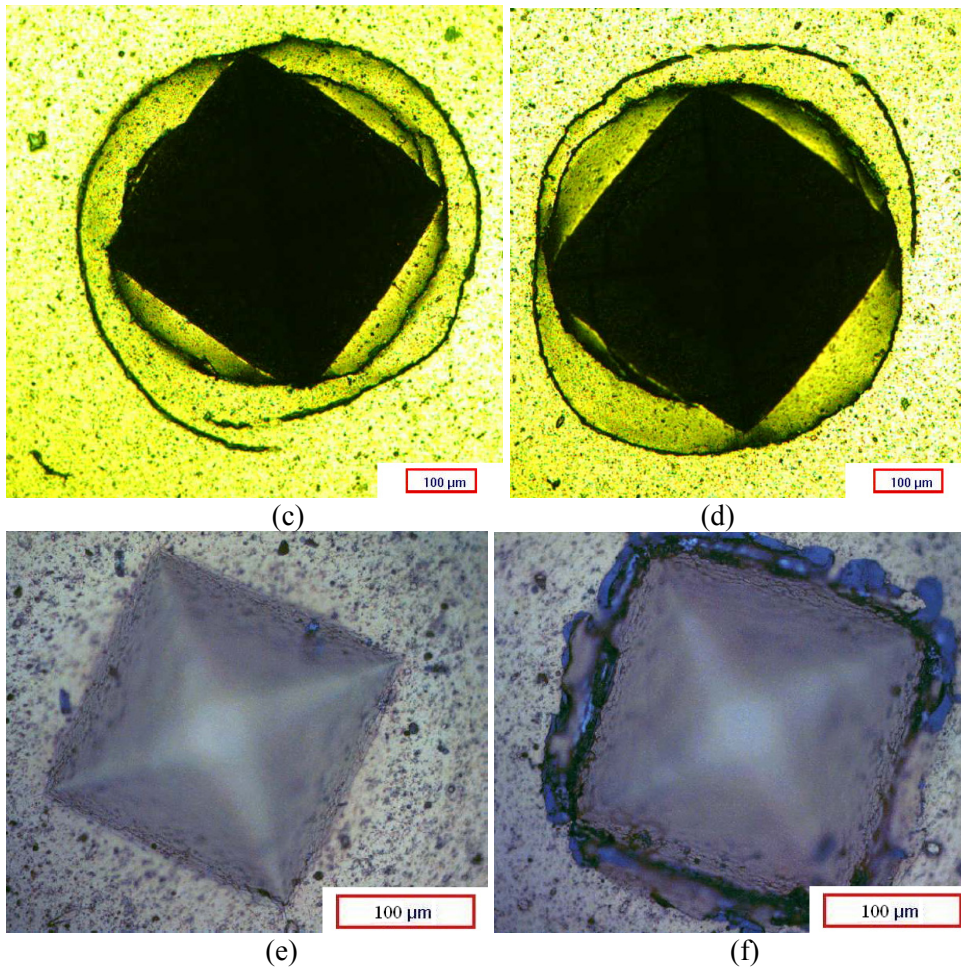


Figure 3.57. Impression corner of the surface of nitrided steel substrate coated with gradient nCo-gold with the appearance of: a – V criteria after 1 cycle; b – V criteria after 100 cycles; c – V criteria after 1000 cycles; d – V criteria after 10000 cycles; e – 0, I criteria after 1000 cycle at indentation load of 100 N; f – V and VI criteria after 10000 cycles at indentation load of 100 N.

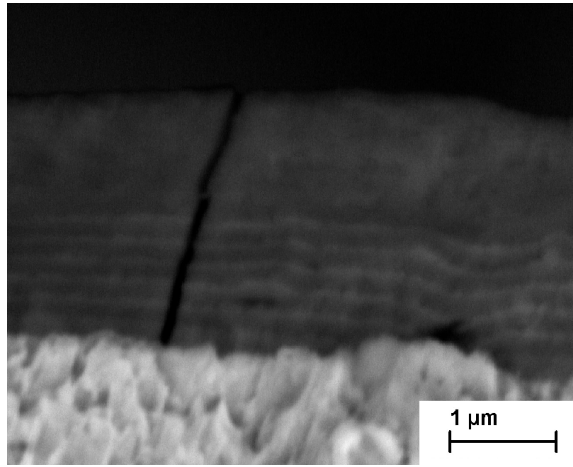


Figure 3.58. SEM image of a crack propagation in duplex microlaminate TiAlN PVD coating.

To estimate the cracking resistance of the coated system, a quantitative analysis of the samples was performed. The lengths of radial cracks from the impression corner were measured and presented on graphs (Figure 3.59 and 3.60) vs. the number of indentation cycles. The error bars show the standard deviation of 2.3 μm.

Radial cracks become the dominant mode of indentation fracture that lead to accelerated cracking resistance degradation of the coating. Fracture analysis revealed that apart from other coatings, in microlaminate TiAlN and multilayer nACo-gold[®] the "brittle" damage mode occurred with the formation of cone cracks, driven by tensile stresses in addition to "quasi-plastic". On the other hand, the obscured subsurface damage and the nucleation of few radial cracks could be found below cone cracks. TiN has the lowest and TiAlN monolayer coating has the second lowest H/E ratio, which result in low elastic recovery ability of the coating.

Gradient AlTiN and TiCN also exhibited well under various indentation loads, resulting considerable amount of radial cracks with length of 20 – 40 μm, which is similar to crack evaluation criteria III (Table 2.4). Such radial fatigue cracks are common to "quasi-plastic" damage mode, which is typical for low H/E ratio coatings. Gradient AlTiN has the mid and gradient nACo coating has the highest H/E ratio, which result in modest elastic recovery ability of the coating. The H/E ratio of AlTiN is 0.089 and gradient nACo has 0.144 (Table 3.9).

Microlaminates and multilayers have higher fatigue resistance than monolayer or gradient coatings despite higher H/E ratio.

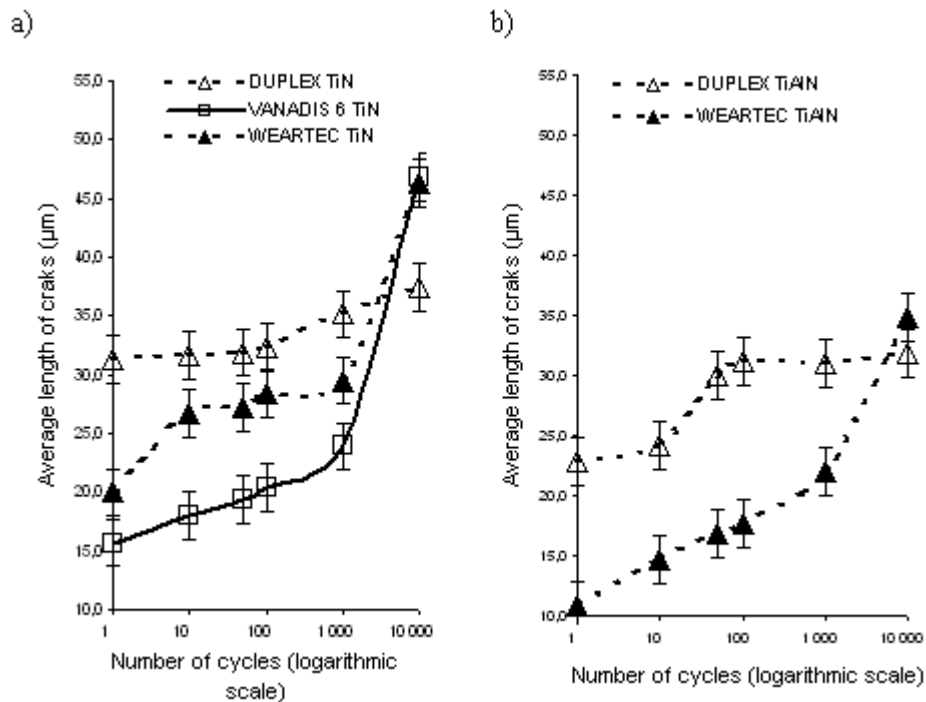


Figure 3.59. Dependence of a substrate material to the average length of cracks of indentation cycles (indentation load of 500 N): a –TiN; b – monolayer TiAlN

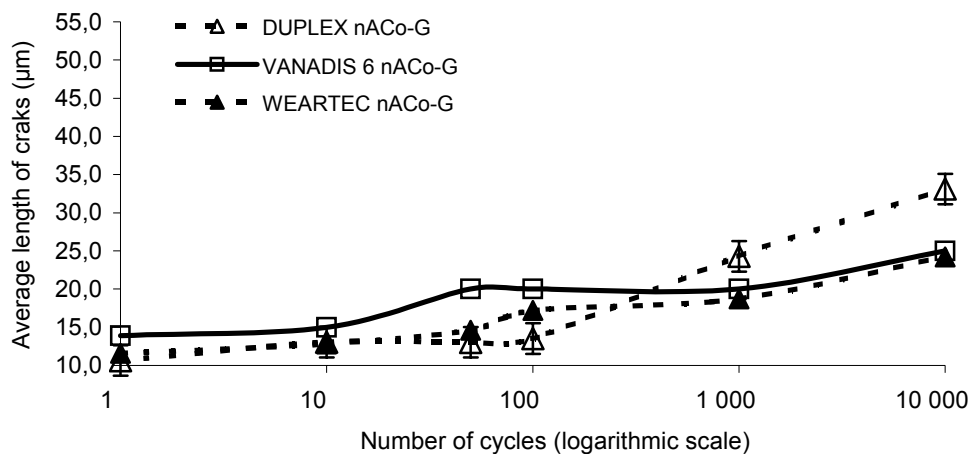


Figure 3.60. Dependence of a substrate material to the average length of cracks of indentation cycles on gradient nACo coating (indentation load of 500 N).

Table 3.9. Properties of studied materials and coatings

Material studied	H_c/E_c	H, GPa	E, GPa	σ , GPa
NS (nitrided steel)	-	8,50	300,00	-
TiN	0,072	25,86	357,00	3,16
TiCN	0,090	31,04	345,00	7,13
TiAlN-multilayer	0,088	30,17	342,00	6,50
TiAlN-monolayer	0,088	30,17	342,00	6,50
AlTiN-gradient	0,089	29,00	325,00	2,94
nAlCo-gradient	0,144	46,18	320,00	4,11
nAlCo-multilayer	0,144	46,18	320,00	4,11
nAlCo-gold (multilayer)	0,144	46,18	320,00	4,11

The results of cyclic indentation are given in Table 3.10. At indentation after the first indentation cycle, mostly contact region model of coating deformation was presented due to the high indenting load of 500 N applied.

Table 3.10. Crack types and crack evaluation criteria for duplex coatings, based on cyclic Vickers indentation.

Number of indentation cycles	1	10	50	100	1000	10000
Coating/substrate						
Nitrided steel 38CrMoAl8	0	0	0	IV	IV	IV
TiN	II	II	II	II	II	II
TiCN	I, II	I, II	I, II	II	III	VI
TiAlN multilayer	V	V	V	V	V	V
TiAlN monolayer	0, I	I	I	II	II	II
AlTiN gradient	0, I	I	I	II	II	III
nAlCo gradient	0, I	I	II	II	II	III
nAlCo multilayer	0, I	VI	VI	VI	VI	VI
nAlCo-gold (multilayer)	V	V	V	V	V	V

The "quasi-plastic" damage mode prevailed as the Vickers diamond pyramid was used in the indentation test. In contrast to spherical indenters, a sharp indenter penetrates easily into the coating surface and cone-cracking formation is suppressed by the radial cracks nucleation. Radial cracks become the dominant mode of indentation fracture and lead to accelerate cracking resistance degradation of the coating. Fracture analysis revealed that apart from other coatings, in microlaminate TiAlN and multiplayer nAlCo® the "brittle" damage mode occurred with the formation of cone cracks, driven by tensile stresses in addition to "quasi-plastic". On the other hand, the obscured subsurface damage and the formation of radial cracks could be found below cone cracks. Multilayer, especially microlaminate coatings have the advantage in structure dependent stress

distributions in wear resistance. As the mechanical properties of substrate play important role in cyclic loading, especially at high loads, coating resistance to plastic deformations under high loads should be assured. Therefore recently, a new assessment criteria for hard coatings was proposed – resistance of coatings to plastic deformations of substrate as a ratio of H_s^3/E_s^2 should be used and maximized [135].

Impact wear

The damage of a material occurred after running of 10^4 cycles is usually referred as a low cycle fatigue [141] while fatigue at higher number of cycles is accepted to be mentioned as high cycle fatigue. In the current study, the loading under the surface fatigue testing was limited by $10^6 - 2 \times 10^6$ cycles since it is often used by authors active in the area of surface fatigue of PVD coatings [142, 143] and that under any conditions of loading below that limit most of the characteristic fatigue failure modes take place [141]. The extent of failure around the imprint is described through the ratio FR which is defined as the ratio of the region in which the substrate is revealed (or highly damaged area, for low number of cycles) vs. the overall contact area [144] – see Figure 3.61.

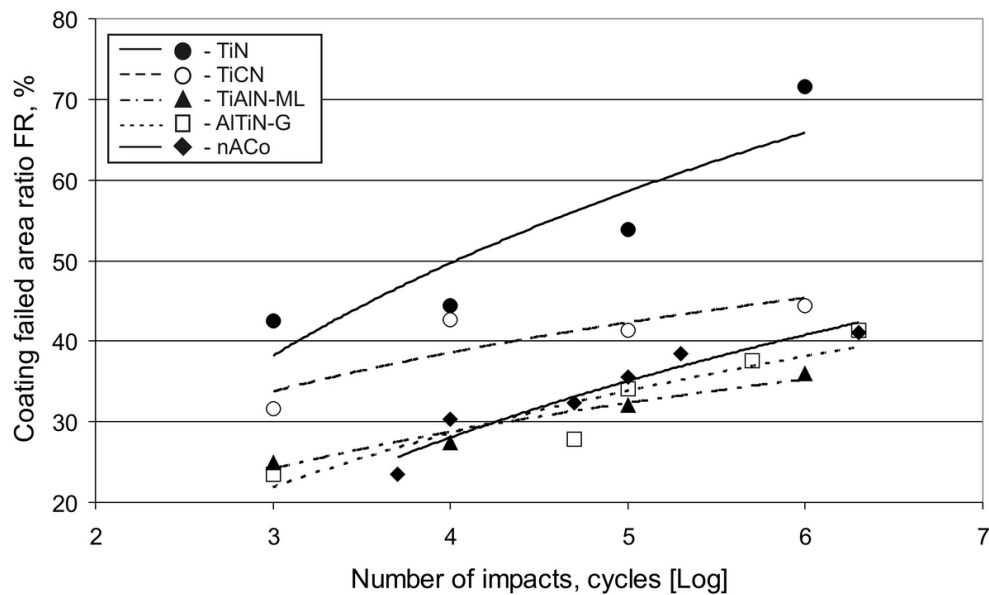


Figure 3.61. Dependence of coating fracture ratio FR on number of impact cycles for normal impact (80 mJ) on CWTS.

The high value of FR warns about the high risk of coating removal through the low adhesion led mechanism. The lines on the plot in Figure 3.61 show the effect of cycle's number on fracture propagation dynamics. TiN coating has sufficiently lower resistance to impact demonstrating the FR values up to 2 times higher than

the group of Al containing coatings at all range of applied number of cycles. Although the FR of the TiCN coating has higher FR ratio as compared to Al containing coatings, the obtained trend allows to assume that after the ultra long run (longer than 10^6 cycles that is possible in interrupted-cut machining) this coating are still resistant to impact because of absence of the further growth of FR value after 10^4 cycles. The degradation of the coating in the centre of the crater, where the compressive dynamic stresses are the highest ones, is minimal (as compared to other coatings) or even invisible at low number of cycles in the case of nano-composite gradient coating nACo[®]. This coating possesses the highest hardness; the nanometric sized AlTiN crystals are distributed throughout tough Si₃N₄ matrix providing the improvement in impact properties. An initial coating failure may be accelerated by the presence of defects or, if the surface has some local protuberance (as far as the surface is rough). Final roughness is hardly be avoided because of droplets that are characteristic to PVD process [123]. The crack propagation, removal of the layer to some or to the whole depth result in redistribution of the contact pressures, oversteering around the areas of removed layer that in its turn facilitate the further removal of layer. Similar effect may be led by coating debris that was not removed from the indentation site. The several concentric cracks are seen around the defect initiated damaged zone (Figure 3.62).

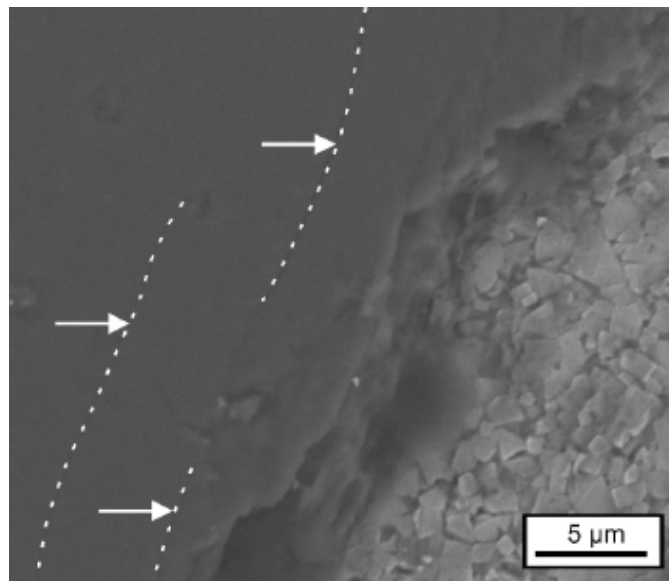


Figure 3.62. Defect initiated failure of the nACo coating by means of the impact testing at 10^6 number of impacts

If coatings are well adherent then cohesive failure mode prevails with traces of microcracking and chipping of small segments of coating material, as it can be seen from Figure 3.63. Some coating debris could be revealed in the lower left corner of the Figure 3.63. The crack grows in the plane parallel to the surface from the initial

defected area and after reaching the critical size under repetitive impacts the large chip is removed from the surface. However, the substrate was kept undamaged that indicate sufficient adherence.

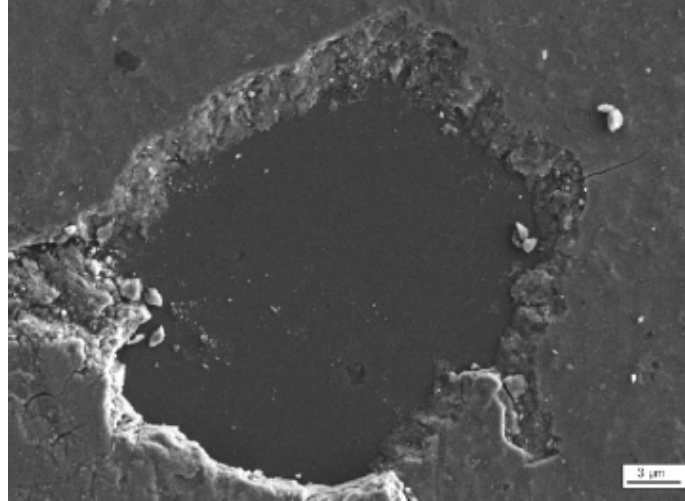


Figure 3.63. Microchipping and cracking of nACo[®] coating.

These results can be explained by greater elastic recovery ability (higher H/E or lower E/H ratios) of multilayer TiAlN coating. Although, the mechanical properties of substrate play important role in cyclic loading, especially at high loads. During the impact test there is a stress gradient, depending on the elastic modulus ratio between the coating and substrate.

The stress ratio between the coating and substrate can be determined based on the rearranged Hook equation [145]:

$$\frac{\sigma_c - \sigma_s}{\sigma_s} = \frac{E_c - E_s}{E_s} \quad (3.2)$$

where σ_c – is the stress applied to coating;
 σ_s – is the stress applied to substrate;
 E_c – is the coating elastic module;
 E_s – is the substrate elastic module.

According to Eq. (3.2) the stress gradient would be zero if where is no different between coating and substrate elastic modules ($E_c=E_s$). Therefore, the smaller the difference between the coating and substrate elastic modules, the lower is the stress gradient, the higher is the wear resistance in impact (cyclic) conditions. The matrix for studied coatings-substrate systems is shown in Table 3.11.

Table 3.11. Differences between coating and substrate elastic modulus matrix

Coating/Substrate	HM	CWTS	NS
TiN	-0.26	1.09	0.59
TiAlN-ML	-0.49	0.43	0.09
WC-17Co	-0.19	1.29	0.75

The better performance of duplex-coating systems can be explained by much lower magnitude of the tensile stresses in the loaded area due to compressive subsurface stresses (from the nitriding treatment) in combination with compressive stresses in the film (produced by the ion plating technique). This explains the better impact resistance of duplex coatings in comparison to their non-duplex rivals.

Residual stresses

Curvature measurements on bimaterial specimens are examined for determination of residual strain/stress of coatings. The PVD deposition of films given in (Table 3.12) at temperatures 450 – 475 °C leads to compressive stresses in the range of –2 to –8 GPa [109]. By using specimens with material layers of comparable thickness, large deflections and thereby high measurement accuracy is obtained [108]. Experiments were performed on PVD coatings deposited on a thick Ni-alloy plates (Figure 2.11), steel and brass stripes (Figure 2.12) and according to following Table 2.5 by PVD method. The characteristic residual stresses, i.e. the thin-film stresses at room temperature, are given in below in Table 3.12.

Table 3.12. Results of residual stress measurements in various PVD coatings

Coating	Residual stresses
TiN	-3.16
TiCN	-7.13
TiAlN	-6.50
AlTiN-G	-2.94
nACo	-4.11

Deposited coatings exhibit dense and fine crystalline structure. The high compressive stress is less influenced by thermal expansion, but more by the layer growth. The atoms or ions forming the film have limited mobility at the substrate surface compared to CVD. The residual stresses are strongly influenced by the deposition temperature, bias voltage, pressure, plasma ionisation and evaporation rate [109]. High compressive stress condition leads to high fracture toughness and fatigue strength of the coated tools. Stable compressive stress is one of the reason of improvement of fracture toughness and fatigue strength of PVD coated tools. The residual compressive stresses of the coating should be lower at the interface to the substrate. Preheated substrate has usually compressive stresses of few hundred

MPa that can be compensated by depositing a coating with the PVD coating of higher stress. If the stress difference is too high, coating-substrate adhesion would be reduced. Fracture toughness and fatigue strength can be increased by depositing coatings with compressive stresses that reach its maximum value in a depth of 1.3 – 1.5 μm towards the coating surface. In case of multilayer coating nACo-gold top layer of thin (200 – 300 nm) TiN has lower compressive residual stresses than the bottom layer of gradient nACo and therefore the improved fatigue strength (Figure 3.57) can be explained by non-linear compressive stress distribution within the coating. As well as because of the lower hardness, wear and oxidation resistance, lower residual stresses and due to lower lattice deformation and defect density of TiN toplayer. TiN layer tends to have a certain stabilizing effect on the reduction of residual stress of gradient nACo coating towards the surface [141]. Effect of Ti interlayer between TiN and steel is used to enhance the adhesion of the coating to substrates and to reduce the thermal mismatch between them [146]. Chemically, diffused mixing of elements forming a broad interface and strong epitaxial relation between the TiN and Ti layers is attributed for better adhesion with Ti interlayer. Mechanically, the Ti interlayer acts as soft, flexible layer, reducing the shear stresses at the coating-substrate contact, stopping the propagation of cracks in the inter-surface area. [146].

3.1.1.1 Characterisation of friction and wear

Coefficient of friction

Recently, it was shown that the relatively high friction coefficient of TiAlN (0.7 – 0.75) is a consequence of the formation of droplets on the surface of coatings, and such an effect is more pronounced in the case of TiAlN in comparison to TiN (0.55) [90].

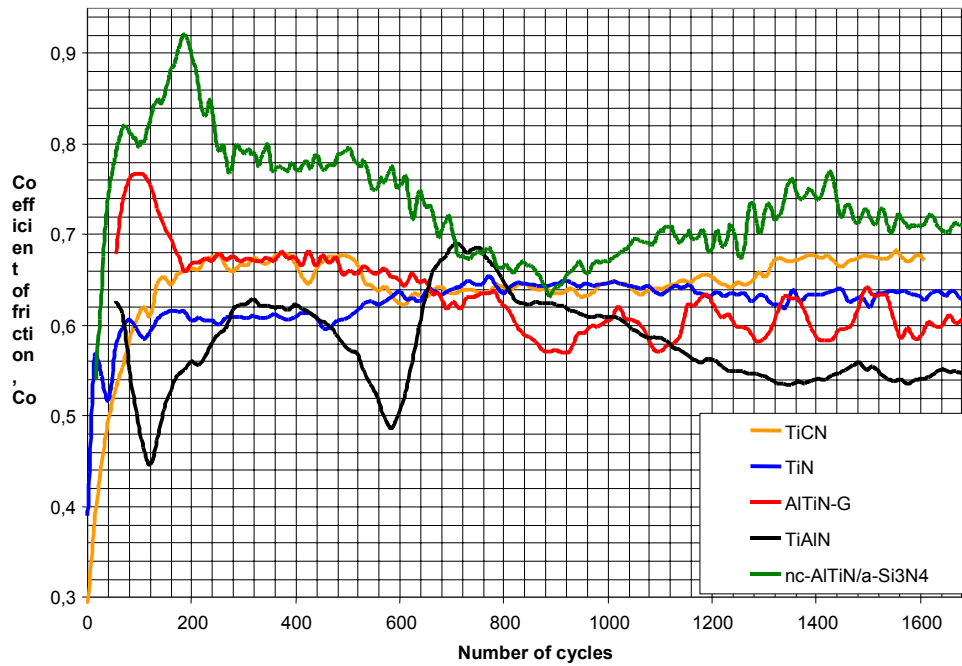


Figure 3.64. Coefficient of friction of selected PVD coatings.

Abrasion and erosion resistance

Uncoated cemented carbides on the base of conventional WC-Co has been widely applied since the early 1920's and it is often said that they are versatile materials and it is mostly due to their sufficiently well performance in many conditions of interest [147, 148]. That is why the coatings of interest in addition to impact were tested also in erosive and abrasive environment and their performance compared in order to give complete overview on materials wear mechanisms.

During the erosion the zone affected by the contact is much smaller and the velocity is higher than during the impact testing (compare Table 2.6 and Table 2.7 and Figure 2.14 and Figure 2.16). That means this testing could give more information regarding the "true" surface properties of the coating itself excluding the effect of substrate or adherence properties of coating to substrate. In order to compare the behaviour of coatings under various conditions the wear rate map was created. The zones of low, medium and high wear rates are shown to make it more comfortable for comparative assessment (Figure 3.68).

The abrasion sliding tests were conducted with the presence of the identical abrasive as erosion ones. Sand particles were fed between the rubber disk and tested specimen (Figure 2.14). Due to the elastic nature, the rubber partially deforms and holds the abrasives scratching in the contact zone. Hardness of the sand is at least twice lower than the hardness of the coatings that means the direct cutting is hardly possible [149]. That is why the fatigue-led or defect-initiated mechanisms are playing an important role.

The coatings are quite sensitive to the energy of the impacting particle in erosive conditions [150]. The energy dependent threshold in material behaviour was previously observed by authors for ceramic-metal composites with defects. For example, materials with porosity of 5% have exhibited the abrupt increase in wear rate when the velocity has reached threshold value. At velocities below the threshold the mechanism of materials removal was rather selective and high cycle; above the threshold, the energy of the impact was sufficient to induce the rapid crack propagation and large particles of material of several micrometers size were removed [151].

Difference in erosion rate of TiN and TiCN indicates (Figure 3.68) that the erodent energy is enough to cause higher damage in TiCN. However TiN behave the same well as nACo. The leading mechanisms of material removal of PVD coating during erosive and abrasive tests originate from the same microstructural features as was previously shown for the impact conditions. The nano-composite gradient structured nACo has the highest wear resistance under erosive and abrasive conditions. This coating exhibits well adherence to the substrate during the abrasive test (Figure 3.65 a). As compared with impact wear testing, the geometry of the crater formed would indicate low FR value (ratio between the region in which the substrate is revealed versus the overall crater area in this case). However, the development of cohesive failure at macro scale (up to 1000 μm in size) takes place and is critical that means that during the extended abrasion test the coating will rapidly fail (Figure 3.65 b).

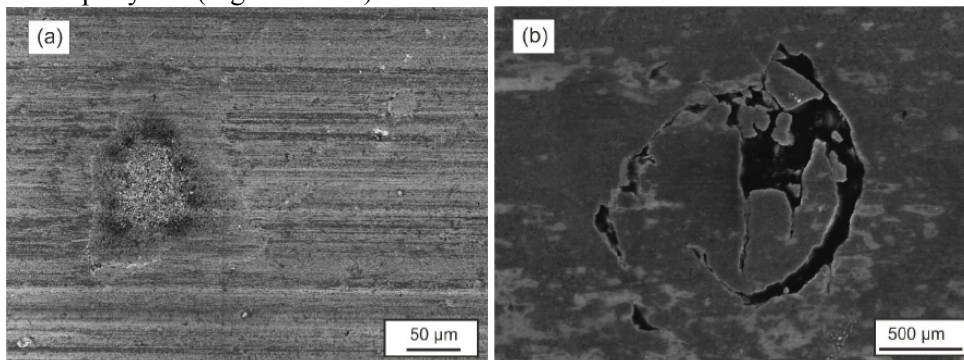


Figure 3.65. Performance of nACo coating under abrasive conditions: a – scratches; b – cohesive failure of the coating.

The initial failure takes place at micro-nano level according to cohesion lost mechanism. The micrograph in shows the damage caused by abrasive particles embedded into the surface irregularity and forced to rotate between rubber wheel and coated surface. Such process results in temporary ploughing. Because of lower mechanical properties, sand particle was broken. Fine abrasive fragments are seen on the left side of the figure. In Figure 3.66 b, the selective removal of the nACo layer fragments during erosion is illustrated. The areas of lost chips are ranging between $1\mu\text{m}$ and some tenths of micrometers.

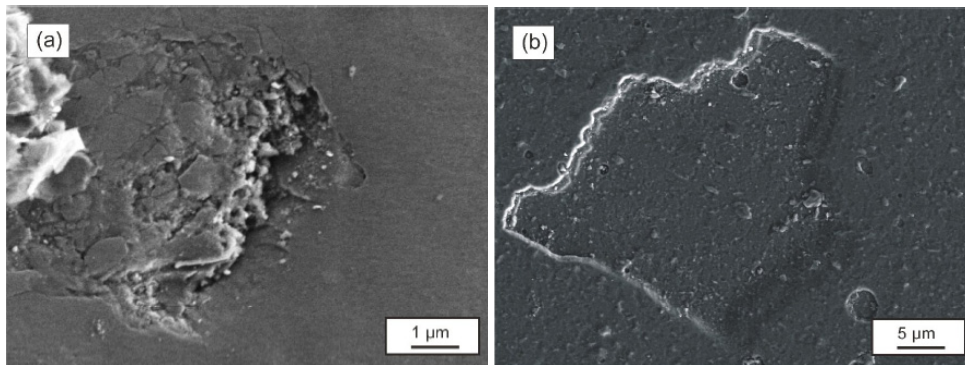


Figure 3.66. Performance of nACo coating under abrasive and erosive conditions: a – formation of the crater as the result of abrasive sliding action; b – cohesive failure of the coating during erosion.

The brittle fracture can be observed around the original defects of nACo coating after erosive testing (Figure 3.67 a and b). The sharp edges point to the fact that they are removed rather through brittle fracture than through removal with some degree of plastic deformation and cutting like it was shown above (Figure 3.65 a) in case of abrasive wear.

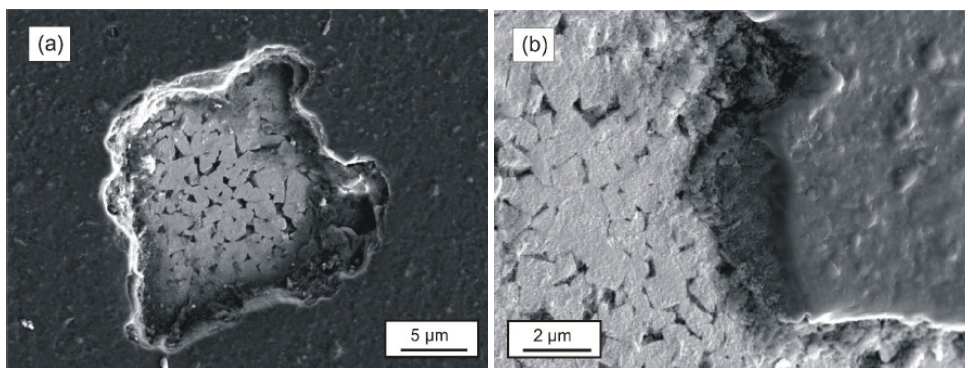


Figure 3.67. Adhesive failure mode of nACo coating under erosive conditions at different magnifications.

The velocity of the abrasive motion influences the resistance of the coatings to a great extent. In the case of abrasion it was 10 times less than during erosion (Table 2.6 and Table 2.7). At higher loading rate the fracture toughness of materials is usually decreased [152] that enhance the possibility of brittle fracture.

The wear mechanisms of coatings under different conditions may be summarized as following:

- High wear resistance: Cohesive mechanism with consecutive removal of flakes. High cycle fatigue mode. Plastic deformation and flow is presented to some extent, selective removal.
- Medium wear resistance: mixed adhesive – cohesive mechanisms.
- Low wear resistance: adhesive failure mechanism with prevailing low cycle fatigue. Removal of layer to the whole depth. Brittle fracture and chipping.

In order to compare the behavior of coatings under various conditions the wear rate map was created. The zones of low, medium and high wear rates are shown to make it more comfortable for comparative assessment (Figure 3.68).

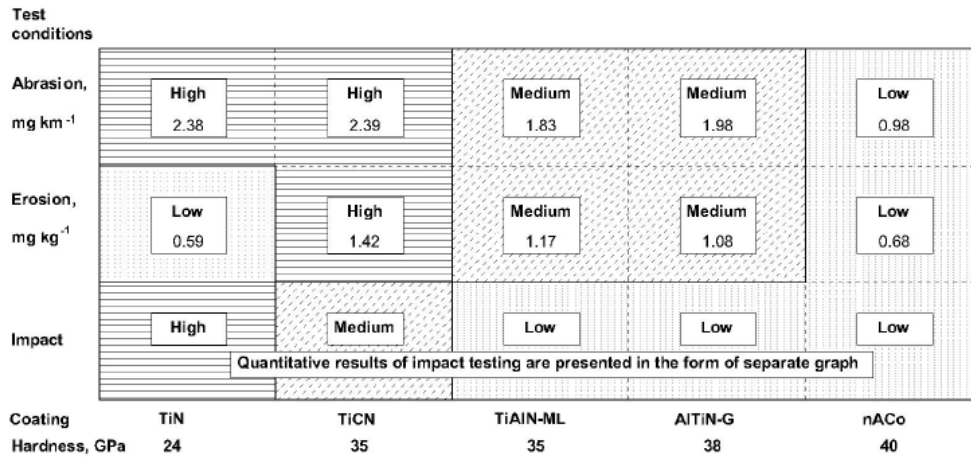


Figure 3.68. Wear rate map of studied PVD coatings under different wear conditions.

Besides “Duplex coating” technique, laser beam treatment (also referred as Duplex treatment) is attracting strong attention worldwide [153]. In comparison to other methods, it allows to obtain higher hardness values, than other heat treatment methods, low distortion of the surface, localized treatment, obtaining of structures that cannot be obtained, applying other technologies [153].

4 SELECTION OF HARD COATINGS FOR TOOLING

PVD technology, being an environmentally friendly has gained a well-known worldwide reputation in these years. Due to the steadily growing demand of the increase in tool lifetime, cutting speed and oxidation resistance in processing alloys and composites – new coatings and surface treatment technologies are to be developed to replace the state of the art TiN PVD coatings.

The usage of hard PVD coatings has gained much acknowledgement as a way to remarkably improve tribological and corrosion resistance properties of the material as new high performance coatings have higher hardness; better wear resistance; lower surface roughness; lower coefficient of friction, higher fatigue and oxidation resistance. However, their application is restricted by the possibility of plastic deformation of the substrate [82, 83, 84], as the coatings themselves are very thin, and the load to be carried by the substrate.

Therefore, the importance of the selection of appropriate substrate material and heat treatment, coating material with its unique physical and chemical properties for particular application is crucial. Various PVD coatings differ from adhesion; hardness; coefficient of friction; state and magnitude of residual stresses; resistance to erosive, abrasive, impact and fatigue wear. Although introduced more than two decades ago, TiN still dominates among the hard coatings employed in the industry. Despite the many numbers of new PVD coatings and coating systems introduced in the last decade there are only few published works of cracking, fatigue, erosion, abrasion and impact resistance of PVD coatings. Thus to suppress wear and cracking in metal cutting and forming tools by the application of the coating, the wear and cracking mechanism must be determined.

Despite the numerous studies that have been carried out by other authors in the field of Ti and Al-based nitride and carbonitride PVD coatings such as TiN, TiCN, (TiAl)N, (AlTi)N having mono-, multilayer, gradient or nanocomposite design, relatively moderate attention has been paid to duplex coatings and duplex treatment techniques of PVD coatings. Plasma-nitriding exhibits characteristic advantages, being environmentally clean, and allowing an efficient low-temperature processing of materials for which only a certain maximum temperature is allowed, e.g. in order to avoid the formation of undesired phases for low tempering steels, due to the activation in the glow discharge plasma. For a large variety of different tool and machine components, a longstanding experience with plasma-nitriding has been acquired in mostly small companies, with successful applications mostly for conventional tool steels. The surface hardness of the tools can be increased by a factor of 2 – 3 [154]. The behaviour of PVD coatings under erosive, abrasive and impact wear conditions; fatigue and the cracking resistance of PVD coatings are important parameters for the design of tools of the metal sheet forming. Therefore,

the present research was focused on the design and characterization of coatings that can be used in tooling.

4.1 Selection based on the properties of the system substrate – coating

Hardness and modulus of elasticity of coatings (H_c/E_c)

The modulus of elasticity E and the ratio H/E have importance in determining the endurance capability and ability to accommodate substrate deflections under load of a surface coating [155]. Recent studies have shown that hard nanocomposite coatings with the same hardness can, according to their chemical composition, exhibit different values of the effective modulus of elasticity E . This could mean that there is a possibility of tailoring the mechanical properties of a material for a given application, but there is no simple relationship between hardness H and modulus of elasticity E . The H/E ratios of studied coatings and their cracking and wear resistance are given in Table 4.1.

As hard coatings have become a standard application in industry, coating properties and tool lifetime has to be understood. Below are given important coating – substrate parameters (Figure 4.1).

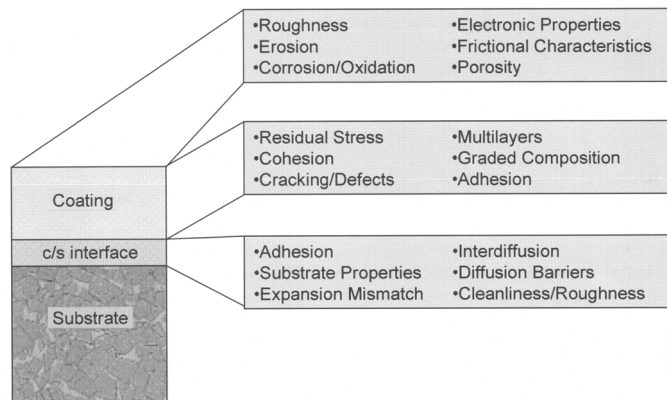


Figure 4.1. Important coating/substrate parameters.

Hardness is one of the most important and easily measurable properties, which has a major effect in tool wear. By sliding and adhesion wear, coating wear rate depends on coating hardness – with increasing of hardness the wear rate is decreasing. Below, in Figure 4.2 is given a map of hardness and Young’s modulus values of studied coatings and substrates.

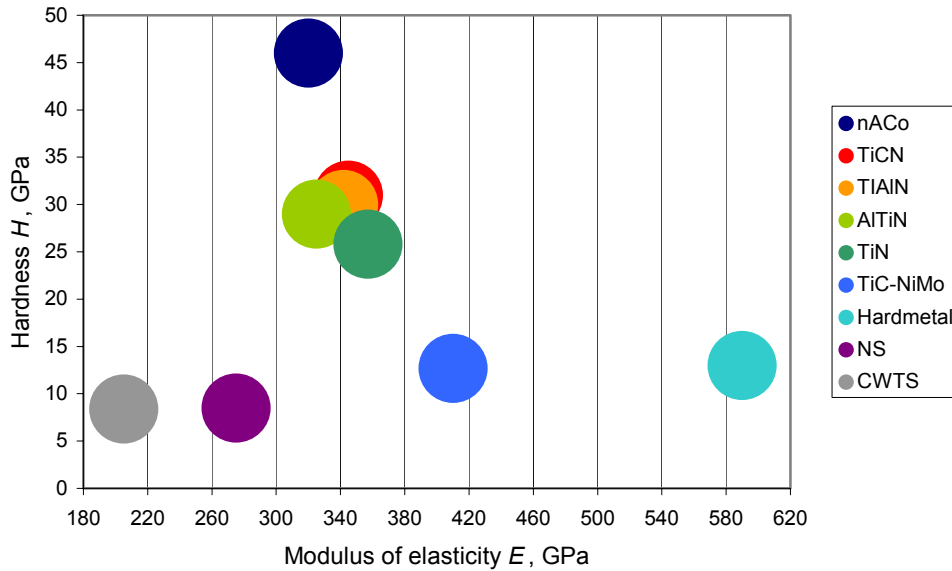


Figure 4.2. Hardness – modulus of elasticity map of studied PVD coatings and substrates

Table 4.1. Wear rating parameters of coating vs H_c/E_c

Type of coating	H_c/E_c	Cracking resistance	Wear resistance	
			At abrasion	At erosion
TiN, monolayer	0.072	+++	+	+
TiCN, gradient	0.090	++	+	+
TiAlN, multilayer	0.088	+	++	++
AlTiN	0.089	+	++	++
nACo	0.144	+	+++	+++

+ - Low resistance
 ++ - medium resistance
 +++ - high resistance

Recent studies show that hardness and modulus of elasticity and with them the relationship between hardness and modulus of elasticity of H/E of the hard coatings can be controlled by its chemical composition and by deposition parameters used for the formation of the coating (also coating architecture) [155].

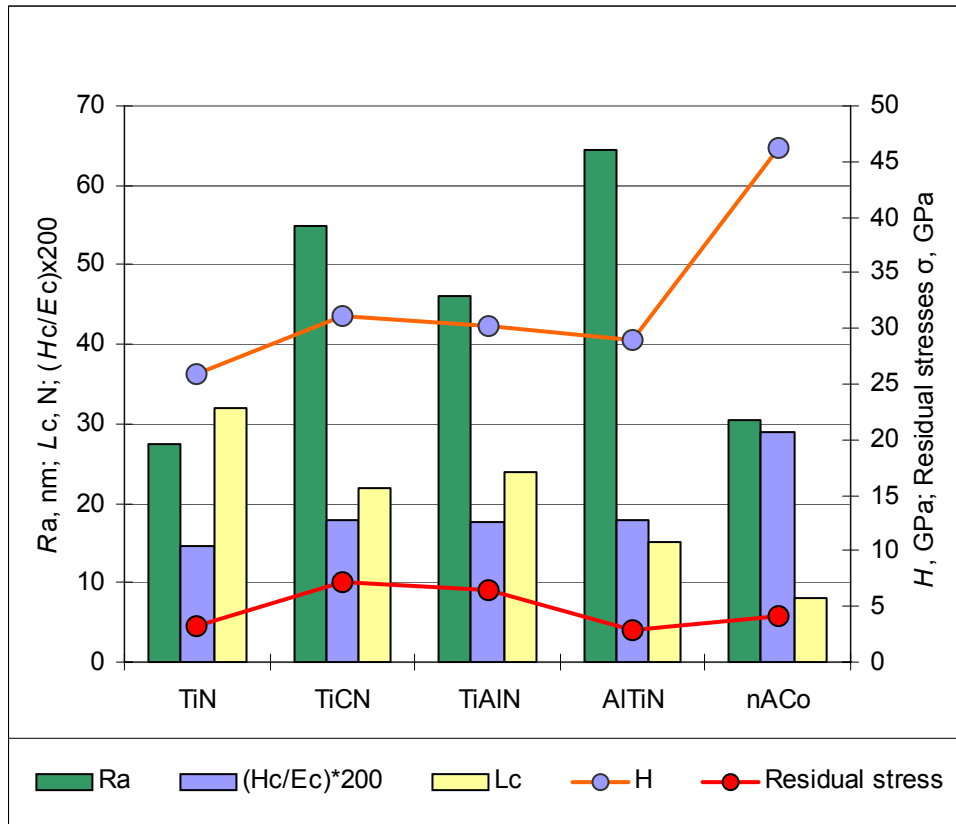


Figure 4.3. Dependence of critical load of various coatings deposited onto CWTS substrates on the surface roughness, R_a ; ratio H_c/E_c ; nanohardness, H , and residual stresses, σ .

Architecture similar to the hardness of the coatings can be controller by deposition parameters and by its chemical composition.

The concept of coatings was given recognition in official documents and specifications in the 1950s. Coating – a layer of a material formed naturally or synthetically or deposited artificially on the surface of an object made of another material, with the aim of obtaining required technical or decorative properties [85].

For obvious reasons, the coating has a laminar structure and because of the great variety of coatings, it is difficult to develop one universal model of coating structure [85]. Below in Figure 4.4 are given a figure of a selection of coating structures that are used most often and that were used in this study. Gradient coatings are not listed below; because the nature of all coatings already listed there is actually also gradient type. The transition from one layer (intermediate layer) to

another is most often gradient. Multilayer, especially microlaminate coatings have the advantage in structure dependent stress distributions and behave better in indentation based surface fatigue tests. The nano-composite coatings again have the highest wear resistance under erosive and abrasive conditions. These coatings exhibits well adherence to the substrate during the abrasive test (Figure 3.65 a).

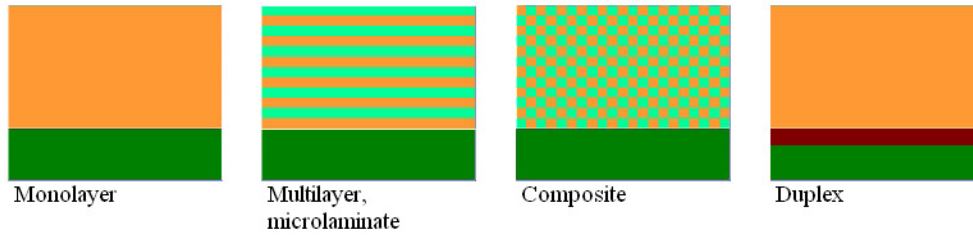


Figure 4.4. Selection of architectures of coatings

Surface roughness

In the results of laboratory pin-on-disc tests and industrial test it was demonstrated that there exists optimal coating surface roughness (Figure 3.64). Coatings with increased surface roughness (TiCN, TiAlN, AlTiN) at pin-on-disc wear tests have higher wear rate and showed higher surface roughness of worn surfaces. At industrial tests coatings with smoother surface, as well coatings with higher surface roughness demonstrated higher adhesion wear at punch tests. Surface roughness is hardly being avoided because of droplets that are characteristic to AIP PVD process, but may be reduced by following followed abrasive (polishing) post-treatment of deposited coatings.

Hardness and modulus of elasticity of substrate as criteria in selection

Hardness of the substrate is the resistance of a substrate material to permanent penetration by another harder material. It cannot be stressed enough that, for tribological applications, the substrate hardness is of prime importance. If the thin fragile hard coating is not sufficiently supported, it will fail at relatively low contact stresses, because it cannot follow deformation of the substrate (so-called “eggshell” effect). The thin hard coating does not resist due to the plastic deformation of substrate material. The resistance to plastic deformation can be estimated by the ratio H_s^3/E_s^2 that is proportional to the resistance of the substrate to plastic deformation. This essentially means that the higher is the resistance to plastic deformation, the higher is the ratio H_s^3/E_s^2 . The H_s^3/E_s^2 ratio of different substrates and their wear rating parameters to surface fatigue and impact wear is given in below (Table 4.2).

Table 4.2. Surface fatigue and impact wear rating parameters vs H_s^3/E_s^2

Substrate	H_s^3/E_s^2	Surface fatigue resistance	Impact wear resistance
WC-Co hardmetal	0.0046	+	+
TiC-Ni-Mo cermet	0.0122	++	++
CWTS	0.0151	+++	+++
Nitrided steel	0.0098	++	++

- + - Low resistance
- ++ - medium resistance
- +++ - high resistance

4.2 Selection based on wear conditions/operation parameters

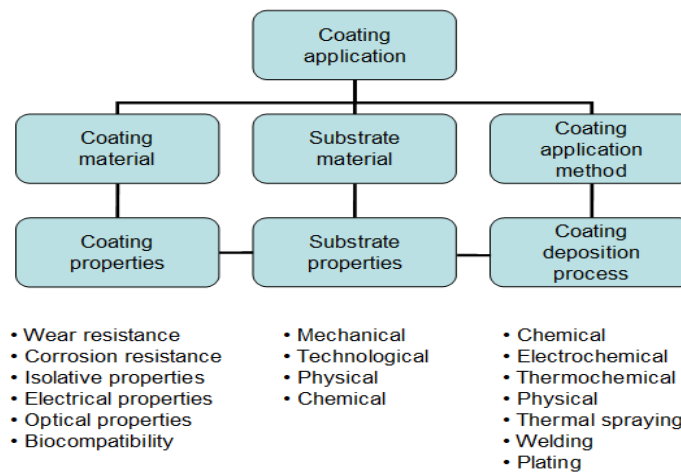


Figure 4.5. Coating application relations to coating material, substrate material and

Different wear types and parameters of wear

Table 4.3. Recommendations for coating selection

	Sliding wear	Adhesion wear	Impact wear	Abrasive wear	
				Abrasion	Erosion ($\alpha < 45^\circ$)
Hardness/Modulus elasticity					
– substrate	-	max. H_s^3/E_s^2	max. H_s^3/E_s^2	max H	0
– coating	max H	max H/E	-	$H_c > H_s$	max H , $H_c > H_s$
Architecture of coating and substrate					
– at low load	hardmetal or hardened substrate	hardmetal or hardened substrate	hardened or NS steel	-	-
– at high load	Hardmetal or cermet	Hardmetal or cermet	CWTS or HSS, hardmetal or cermet	-	-
Frictional and wear properties					
– CoF	min CoF	min CoF	-	-	-

- has little influence

CONCLUSIONS

In the result of the study of different “substrate-coating” systems (hardmetal – coating, tool steels – coating, nitrided steel – coating (duplex coatings) and using different methods for characterisation of coating systems (adhesion and indentation based surface fatigue tests, different wear tests – pin-on-disc, abrasion, erosion and impact wear), following main conclusions can be done:

1. The quality of coatings (adhesion, surface roughness) and with them service performance depend of various parameters as surface preparation, technological parameters of the PVD process as well as post-treatment of coated surfaces. To increase the application range of traditional substrate materials gamma (hardmetals and high speed steels) the low tempering temperature constructional steels are prospective as substrates for PVD coatings, also using duplex treatment as pretreatment (nitriding, case hardening) as well as post-treatment (laser hardening, and polishing treatment for the removal of surface irregularities as microdroplets.

2. In the result of adhesion tests among the tested PVD coatings TiN coatings seems to be most endurable. The mixed failure modes are characteristic, presented are chipping, delamination with buckling and fracture. The smaller the difference between the coating and substrate elastic modules, the lower is the stress gradient, the higher is the wear resistance in impact (cyclic) conditions. High compressive stress condition leads to high fracture toughness and fatigue strength of the coated tools.

3. In the result of indentation cyclic tests the “quasi-plastic” damage mode with formation of radial cracks prevailed and is typical for low H/E values of coatings. The increase of the number of cycles leads to the radial crack growth. “Brittle” damage with formation of cone cracks as characteristic of the PVD coatings with highest H/E ratio. Multilayer coatings had higher impact fatigue resistance than monolayer coatings with high H/E ratio. On the other hand in fatigue tests by indentation – multilayer structure leads to inter-layer delamination and chipping.

4. Coatings with high H/E ratio (TiCN, nACo) demonstrated improved wear resistance at low energy impact wear – at solid particle erosion. To assure the resistance of coatings at high loads and high-energy impact wear for estimation of performance of coatings resistance to plastic deformation of the substrate – a ratio H_s^3/E_s^2 should be maximized and coating with multilayer microstructure (preferably having a TiN coating on top of the underlying coating) is preferable.

5. The main principles for coatings selection for different wear conditions are proposed as following;

- for sliding wear and abrasion – PVD coatings with highest hardness (max H/E) should be used. Nanocomposite coatings behave well under these conditions. At low normal loads as it is mostly in case of sliding wear – substrate selection is not so critical.
- for solid particle erosion – It is believed that hard PVD coatings do not work in erosion conditions. However, nanocomposite and TiN coatings behave well under . Depends on the impact angle and kinetic energy of the solid particle – the substrate may have an important role in wear rate.
- for impact wear – it is believed that thin PVD coatings have low performance in such conditions.

6. Future plans include the study and optimisation of surface roughness as it is often considered as most important parameter wear of punches in tooling, specially in fine blanking. Other interest includes the study of the influence of top surface layers to the indentation resistance of on various PVD coatings and the relations between coating thickness and compressive residual stresses. Also, thick PVD coatings are attractive due to the possibility to increase the wear resistance of substrate. Another interest is to study the possibility to grow carbon nanotubes simultaneously into the PVD coating during deposition process enabling to increase the toughness of hard coatings.

REFERENCES

- [1] Axenov et al. Vacuum-arc plasma apparatus. 1985. U.S. Pat. No. 4551221
- [2] Bunshah R.F. Handbook of Deposition Technologies for Films and Coatings. Ed. Noyes, New Jersey, 1995
- [3] Holleck. H., Designing Advanced Coatings for Wear Protection, Surface engineering, 7, (1991), 137- 144.
- [4] D.S. Rickerby, A. Matthews, Advanced surface Coatings – A Handbook of surface Engineering, Blackie and Sons, London, 1991
- [5] Protective Coatings and Thin Films, Kluwer Academic Publishers, Dordrecht/Boston/London, 1997
- [6] Navinsek, B., Sudipta S. Transition metal nitride functional coatings. JOM, Volume 53, Number 9, September 2001, pp. 51-54 (4)
- [7] Cselle T., Morstein M., Holubar P., Jilek M., Karimi A. Nanostructured Coatings and Processes on an Industrial Scale. Advanced Coatings and Surface Systems for Cutting Tools & Wear Parts Gorham Conference, Nov/2002, Atlanta, GA, USA
- [8] Braic M., Braic V., Balaceanu M., Pavelescu G., Vladescu A., Tudor I., Popescu A., Borsos Z., Logofatu C., Negri C. C. Micromechanical and mechanical characteristics of arc plasma deposited TiAlN and TiN/TiAlN coatings. Journal of Optoelectronics and Advanced Materials Vol. 7, No. 2, April 2005, p. 671 - 676
- [9] Hsieh J. H., Liang C., Yu C. H., Wu W., Surf. Coat. Technol., 132 (1998) 108-109
- [10] Imbeni V., Martini C., Lanzoni E., Poli G., Hutchings I. M., Wear 251 (2001) 997
- [11] Hovsepian P. Eh., Lewis D. B., Münz W. D., Surf. Coat. Technol. 133-134 (2000) 166
- [12] Mattox D. M. The foundations of vacuum coatings technology. Noyes publications, William Andrew publishing, Norwich, New York, USA
- [13] Snaper A. A. Arc deposition process and apparatus. 1971. U.S. Pat. No. 3625848
- [14] Snaper A. A. Arc deposition apparatus. 1974. U.S. Pat. No. 3836451
- [15] Sablev et al. Apparatus for vacuum-evaporation of metals under the action of an electric arc. 1974. U.S. Pat. No. 3783231
- [16] Sablev et al. Apparatus for metal evaporation coating. 1974. U.S. Pat. No. 3793179
- [17] Sablev et al. Consumable cathode for electric-arc metal vaporizer. 1986. U.S. Pat. No. 4563262
- [18] Sablev et al. Electric arc metal evaporator. 1995. U.S. Pat. No. 5451308
- [19] Sablev et al. Method and device for treatment of products in gas-discharge plasma. 1996. U.S. Pat. No. 5503725

-
- [20] Veprek S., Jilek M. Superhard nanocomposite coatings. From basic science toward industrialisation. *Pure Appl. Chem.*, Vol. 74, No. 3, 2002, 475–481
- [21] Zhang S. Wang H. L., Ong S.-E., Sun D., Bui X. L. Tough yet hard nanocomposite coatings – present status and future trends. *Plasma Process. Polym.* 2007, 4, 219–228
- [22] Tjong S.C., Chen H. Nanocrystalline materials and coatings. *Materials Science and Engineering R* 45 (2004) 1–88
- [23] Korhonen A. S., Harju E. Surface engineering with light alloys – hard coatings, thin films, and plasma nitriding. *Journal of Materials engineering and performance.* (2000), 9, 302 – 305.
- [23] Ryabchikov, A.I., Koval N.N., Stepanov I.B., Goncharenko I.M., Sivin D.O., Ryabchikov I.A., Shulepov I.A. Formation of Wear-Resistant TiN and (Ti_{1-x}, Al_x)N Coatings Using DC Filtered Vacuum Arc Plasma. 13th International Symposium on High Current Electronics (2004)
- [25] Bemporad E., Sebastiani M., Pecchio C., De Rossi S. High thickness Ti/TiN multilayer thin coatings for wear resistant applications. *Surface & Coatings Technology* 201 (2006) 2155–2165
- [26] Dobrzański L. A., Golombek K. Structure and Properties of Selected Cemented Carbides and Cermets Covered with TiN/(Ti,Al,Si)N/TiN Coatings Obtained by the Cathodic Arc Evaporation Process. *Materials Research*, Vol. 8, No. 2 (2005)113-116
- [27] Gregor, A., Podgursky, V., Adoberg, E., Kulu, P. Hard coatings manufacturing technology used in tooling. 5 International DAAAM Baltic Conference “Industrial engineering – adding innovation capacity of labor force and entrepreneurs” 2006, Estonia
- [28] MacKenzie M., Craven A.J., Hatto P. Erosion and deposition during the sputter cleaning of substrates prior to the cathodic arc evaporation of transition metal nitride coatings. *Thin Solid Films* 349 (1999) 176 - 185
- [29] Harris S.G., Doyle E.D., Wong Y-C., Munroe P.R., Cairney J.M., Long J.M. Reducing the macroparticle content of cathodic arc evaporated TiN coatings. *Surface and Coatings Technology* 183 (2004) 283–294
- [30] Ahlgren M., Blomqvist H. Influence of bias variation on residual stress and texture in TiAlN PVD coatings. *Surface & Coatings Technology* 200 (2005) 157– 160
- [31] Andreev et al. Coating for metal cutting tools. 1984. U.S. Pat. No. 4436830
- [32] Andreev et al. Multilayer coatings for metal-cutting tools. 1985. U.S. Pat. No. 4554
- [33] Andreev et al. Method and apparatus for controlling plasma generation in vapour deposition. 1985. U.S. Pat. No. 4512867
- [34] Axenov et al. Arc plasma generator and a plasma arc apparatus for treating the surfaces of work-pieces, incorporating the same arc plasma generator. 1984. U.S. Pat. No. 4452686

-
- [35] Prabhakara H.R. Plasma Assisted Physical Vapour Deposition. <http://bangaloreplasmatek.com/plasma.html> (8. Nov.2009)
- [36] Arps J. H. Ion surface engineering. <http://www.swri.org/3pubs/brochure/d06/ionbeam/Ion%20Surface%20Brochure.pdf> (8. Nov. 2009).
- [37] Boxman R. L., Sanders D. M., Martin P. J. Handbook of vacuum arc science and technology. Fundamentals and applications. Noyes Publications New Jersey 1995, 772 p.
- [38] Brown I. G. Cathodic arc deposition of films. Annual review of materials science 1998. 28. 243 – 269.
- [39] O. Lloyd, The origin of anomalously fast ions in the vacuum arc. 10th international conference of ionised Gases, Oxford, 1, 184, 1971.
- [40] Cakenbergh V. Device for manufacturing thin layers of mineral substances. 1974. U.S. Pat. No. 3922214
- [41] Schuelke T., Witke T., Scheibe H-J., Siemroth P., Schultrich B., Zimmer O., Vetter J. Comparison of DC and AC arc thin film deposition techniques. Surface and Coatings Technology 120 – 121 (1999) 226-232.
- [42] Boxman R. L., Zhitomirsky V. N. Vacuum arc deposition devices. Review of scientific instruments, 77, 021101, (2006).
- [43] Boxman R. L., Beilis I. I., Gidalevich E., Zhitomirsky V. N. in vacuum arc deposition: a review. IEEE transactions on plasma science. 2005, vol. 33 (1), 5, 1618-1625
- [44] V. V. Gasilin, V.A. Zavaleyev, Yu. N. Nezovibat'ko, O.M. Shvets, V.S. Taran, E.V. Skorina. Coating in the arc discharges with plasma flow filtration. Problems of Atomic Science and Technology. 2006, Nr. 6. Series: Plasma Physics (12), p. 210-212
- [45] Boxman R. L., Beilis I. I., Gidalevich E., Zhitomirsky V. N. in vacuum arc deposition: a review. IEEE transactions on plasma science. 2005, vol. 33 (1), 5, 1618-1625
- [46] Rudenja S. Duplex TiN coating on stainless steel. An electrochemical and surface analysis study. PhD thesis, Royal Institute of Technology, Stockholm 1999, 136 p.
- [47] Castleman B. W. Anode assisted sputter etch and deposition apparatus. 1980. U.S. Pat. No. 4201654
- [48] Kurijama N. Sputtering device. 1980. U.S. Pat. No. 4221652
- [49] Wright et al. Cathode sputtering with multiple targets. 1981. U.S. Pat. No. 4252626
- [50] Morrison Jr. Magnetically enhanced sputtering device. 1981. U.S. Pat. No. 4265729
- [51] Aksyonov D. S., Aksenov I. I., Zadneprovsky Yu. A., Loboda A. M., Melnikov S. I., Shulayev V. M. Vacuum-arc plasma source with steered cathode spot. Problems of atomic science and technology. 2008. № 6. Series: Plasma Physics (14), p. 210-212.

-
- [52] Awad S. H., Qian H. C. Deposition of duplex Al₂O₃/TiN coatings on aluminum alloys for tribological applications using a combined microplasma oxidation (MPO) and arc ion plating (AIP). *Wear* 260 (2006) 215–222
- [53] Ducros C., Benevent V., Sanchette F. Deposition, characterization and machining performance of multilayer PVD coatings on cemented carbide cutting tools. *Surface and Coatings Technology* 163–164 (2003) 681–688
- [54] Ho W-Y., Hsu C-H., Huang D-H., Cheng Y-P., Lin Y-C., Chang C-L. Oxygen effect on the mechanical behaviors of Cr(N,O)/CrN double-layered coatings by cathodic arc evaporation. *Surface & Coatings Technology* 188–189 (2004) 129–134
- [55] Chang Y-Y., Wang D-Y., Hung C-Y. Structural and mechanical properties of nanolayered TiAlN/CrN coatings synthesized by a cathodic arc deposition process. *Surface & Coatings Technology* 200 (2005) 1702–1708
- [56] Chang C-L., Jao J-Y., Chang T-C., Ho W-Y., Wang D-Y. Influences of bias voltage on properties of TiAl-doped DLC coatings synthesized by cathodic arc evaporation. *Diamond & Related Materials* 14 (2005) 2127–2132
- [57] Veltrop et al. Cathode arc discharge evaporating device. 1988. EP No. 0284145
- [58] Veltrop et al. Cathode arc discharge evaporating device. 1989. U.S. pat. No. 4849088
- [59] Kuriyama et al. Sputtering device. 1980. U.S. Pat. No. 4221652
- [60] Welty R. B. Apparatus and method for coating a substrate using vacuum arc evaporation. 1993. U.S. Pat. No. 5269898
- [61] Anton B. R., Esquibel P. C. Decorative and functional TiN coatings for aluminium bicycle parts.
http://www.vaportech.com/pdf/VaporTech_RockShox.pdf (9. Nov. 2009)
- [62] Sablev L. P., Andreev A. A., Kunchenko V. V., Grigoriev S. N. Vacuum-arc evaporator of metals with an extended planar cathode. *Materials science forum*. Vols – 287 – 288 (1998) pp. 323 – 326
- [63] Hanaguri et al. Arc ion plating device and arc ion plating system. 1998. U.S. Pat. No. 5730847
- [64] Tamagaki et al. Vacuum arc deposition apparatus. 1998. U.S. Pat. No. 5744017
- [65] Akari K. Vacuum arc evaporation method. 1999. U.S. Pat. No. 5961729
- [66] Holubar P. Wear resistant coating. 2000. WO 00/56946
- [67] Gołombek K., Dobrzański L.A., Sokoviński M. Properties of the wear resistant coatings deposited on the cemented carbides substrates in the cathodic arc evaporation process. *Journal of Materials Processing Technology* 157–158 (2004) 341–347

-
- [68] Holubar et al. Apparatus for evaporation of materials for coating of objects. 2002. WO 02/50864 A1
- [69] Morstein et al. Apparatus for evaporation of materials for coating of objects. 2002. WO 02/50865 A1
- [70] Morstein M., Cselle T., Holubar P., Jilek M., Blosch P. Arc-coating process with rotating cathodes. 2004. U.S. Pat. No. 2004/0007455A1
- [71] Morstein M., Cselle T., Holubar P., Jilek M., Blosch P. Arc-coating process with rotating cathodes. 2005. U.S. Pat. No. 6926811B1
- [72] Capa M., Tamer M., Gülmez T., Bodur T. Life enhancement of hot – forging dies by plasma-nitriding. Turkish Journal of Engineers, Environmental Science, 24 (2000), 111 – 117.
- [73] Luo Q., Hovsepian P. Eh., Lewis D. B., Münz W. – D., Kok Y. N., Cockrem J., Bolton M., Farinotti A. Tribological properties of unbalanced magnetron sputtered nano – scale multilayer coatings TiAlN/VN and TiAlCrYN deposited on plasma nitrided steels. Surface and coatings technology, 93, (2005) 39 – 45.
- [74] Jurci P., Panjan P. Surface processing of PM Vanadis 6 steel with plasma nitriding and CrN PVD – coating. EuroPM 2005, Prague.
- [75] EPRI centre for materials fabrication. Improve metallurgical properties and increase productivity using ion nitriding. Technocommentary, Vol 2, No. 5, 1994.
- [76] Gomez B. J., Caruso R., Nachez L., Diaz-Parralejo A., Feugeas J., de Sanctis O. Influence of ion nitriding process on the properties of zirconia coating deposited on stainless steel. Brazilian journal of physics. Vol 36, No. 3B, 2006, 1000 – 1003.
- [77] Ueda M., Gomes G. F., Kostov K. G., Reuther H., Lapienski C. M., Soares P. C., Takai O., Silva M. M. Results from experiments on hybrid plasma immersion ion implantation/nitriding processing of materials. Brazilian journal of physics, Vol 34, No. 4B, 2004, 1632 – 1637.
- [78] Panjan P., Urankar I., Navinsek B., Tercelj M., Turk R., Cekada M., Leskovsek V. Improvement of hot forging tools with duplex treatment. Surface and coatings technology, 151 – 152, (2002), 505 – 509
- [79] Navinsek B., Panjan P., Urankar I., Cvahte P., Gorenjak F. Improvement of hot-working processes with PVD coatings and duplex treatment. Surface and coatings technology, 142 – 144, (2001), 1148 – 1154.
- [80] Spalvins T. Advances and directions of ion nitriding/carburising. 2nd international ion nitriding /carburising conference sponsored by the American society of metals, Cincinnati, Ohio, September 18-20, 1989.
- [81] Podgornik B., Vizintin J., Wänstrand O., Larsson M., Hogmark S., Ronkainen H., Holmberg K. Tribological properties of plasma nitrided and hard coated AISI 4140 steel. Wear 249 (2001) 254 – 259.

-
- [82] Batista J. C. A., Matthews A., Godoy C. Micro – abrasive wear of PVD duplex and single – layered coatings. *Surface and coatings technology*, 142 – 144, (2001), 1137 – 1143.
- [83] Batista J. C. A., Godoy C., Buono V. T. L., Matthews A. Characterisation of duplex and non-duplex (Ti,Al)N and Cr-N PVD coatings. *Materials science and engineering A*, 336, 2002, p. 40.
- [84] Alsaran A., Celik A., Celik C., Efeoglu I. Optimisation of coating parameters for duplex treated AISI 5140 steel. *Materials science and Engineering A*, 371, 2004, p. 141.
- [85] Burakowski T., Wierzchon T. *Surface engineering of metals. Principles, equipment, technologies.* CRC Press PLL, 1999, 592 p.
- [86] Hogmark S., Jacobson S., Larsson M. Design and evaluation of tribological coatings. *Wear*, 246, (2000), 20–33.
- [87] Holmberg K., Ronkainen H., Laukkanen A., Wallin K., Hogmark S., Jacobson S., Wiklund U., Souza R. M., Stähle P. Residual stresses in TiN, DLC and Mo₂S coated surfaces with regard to their tribological fracture behaviour, *Wear*, 2009.
- [88] Clyne T. W. *Encyclopedia of Materials: Science and Technology, Elasticity and residual stresses.* PJ Withers (ed.), Elsevier 2001.
- [89] Gökkaya H., Nalbant M. The effects of cutting tool Coating on the surface roughness of AISI 1015 steel depending on cutting parameters. *Turkish Journal of Engineering. Environmental Science.* 30, (2006), 307 – 316.
- [90] Holmberg K., Matthews A. *Coatings tribology – Properties, mechanisms, techniques and applications in surface engineering.* Second edition. Tribology and interface engineering series, vol. 56, 2009, 560 p.
- [91] Stachowiak G. W., Batchelor A. W. *Engineering tribology.* Second edition. Butterworth – Heinemann, 2001,
- [92] Kleis I., Kulu I. *Solid Particle Erosion: Occurrence, Prediction and Control.* Springer-Verlag New York Limited, 2007, 233p.
- [93] Kim D. K., Jung Y.-G., Peterson I. M., Lawn B. R. *Acta Mater.* 47 (1999) 4711 – 4725.
- [94] Bauer C. et al. Towards a framework for life cycle thinking in the assessment of nanotechnology. *Journal of cleaner production.* 16, (2008), 910 – 926.
- [95] Möller W., Mukherjee S. Plasma-based ion implantation. *Current science*, 83, 3, (2002), 237 – 253.
- [96] Holmberg K., Laukkanen A., Ronkainen H., Wallin K., Varjus S. A model for stresses, crack generation and fracture toughness calculation in scratched TiN-coated steel surfaces. *Wear* 254, (2003), 278–291.
- [97] Jacobs R., Meneve J., Dyson G., Teer D.G., Jennett N.M., Harris P., Stebut, J. Comte C., Feuchter P., Cavaleiro A., Ronkainen H., Holmberg K., Beck U., Reiners G., Ingelbrecht C.D. A certified reference material for

-
- the scratch test. *Surface and Coatings Technology*, 174 –175, (2003), 1008–1013.
- [98] Hogmark S., Jacobson S., Larsson M. Design and evaluation of tribological coatings. *Wear* 246, (2000), 20–33.
- [99] Bull S.J., Berasetegui E.G. An overview of the potential of quantitative coating adhesion measurement by scratch testing. *Tribology International*, 39, (2006), 99–114.
- [100] Berg G., Friedrich C., Broszeit E., Berger C. Scratch test measurement of tribological hard coatings in practice. *Fresenius Journal Analytical Chemistry*, (1997), 358, 281–285.
- [101] Stebut J., Lapostolle F., Bucsa M., Vallen H. Acoustic emission monitoring of single cracking events and associated damage mechanism analysis in indentation and scratch testing. *Surface and Coatings Technology*, 116–119, (1999), 160–171.
- [102] Bull S.J., Bhat D.G., Staia M.H. Properties and performance of commercial TiCN coatings. Part 2: tribological performance. *Surface and Coatings Technology*, 163 –164, (2003), 507–514.
- [103] Technical Specification Guide CEN/TS 1071-8:2004 of the European Committee for Standardization, “Advanced technical ceramics – Methods of test for ceramic coatings, Part 8: Rockwell indentation test for evaluation of adhesion”.
- [104] VDI 3198:1992-08, coating (CVD, PVD) of cold forging tools, VDI-Verlag, Dusseldorf, 1991.
- [105] Palmqvist S. The work for the formation of a crack during Vickers indentation as a measure of the toughness of hard metals (in German), *Arch. Eisenhüttenwes.*, 1962, 33, 629 – 34.
- [106] Murotani T., Hirose H., Sasaki T., Okazaki K. Study on stress measurement of PVD-coating layer. *Thin solid films*, 377-378, (2000), 617-620.
- [107] Clyne T. W. Residual stresses in thick and thin surface coatings. *Encyclopedia of materials: Science and Technology*. Withers P. J., Elsevier (2001).
- [108] Gunnars J., Wiklund U. Determination of growth-induced strain and thermo-elastic properties of coatings by curvature measurements. *Materials science and engineering*, A336, (2002), 7-21.
- [109] Arndt M., Westphal H. Influence of residual stresses and nanostructure on the properties and applications of PVD coatings. Proceedings of the 7th international conference “THE” Coatings in manufacturing engineering, 1-3 October 2008, Chalkidiki, Greece.
- [110] Shull A. L., Spaepen F. Measurements of stress during vapour deposition of copper and silver thin films and multilayers. *Journal of applied physics*, 80, 11, (1996), 6243-6256.

-
- [111] Wiedemann R., Oettel H., Bertram T., Weihnacht V. Mechanical properties of TiN coatings. *Advanced engineering materials*, (2001), 3, No. 11, 865-870.
- [112] Withers P. J., Bhadeshia H. K. D. H. Residual stresses, Part 1 – Measurement techniques. *Materials science and technology*, (2001), Vol. 17, 355-365.
- [113] Withers P. J., Bhadeshia H. K. D. H. Residual stresses, Part 2 – Nature and origins. *Materials science and technology*, (2001), Vol. 17, 366-375.
- [114] Hussainova I., Antonov M. Assessment of cermets performance in erosive media. *International journal of materials production technology*. 28, (2007), 361 – 376.
- [115] Antonov M. et al. New high frequency surface fatigue wear tester: design and first results. *Proceedings of the 13th Nordic Symposium on Tribology – NORDTRIB 2008*, (2008), 1- 10
- [116] Kugscheider E. et al. Structure and properties of PVD-coatings by means of impact tester. *Surface and coatings technology*. 116 – 119, (1999), 141 – 146.
- [117] Bouzakis K.-D. et al. The inclined impact test, an efficient method to characterise coatings cohesion and adhesion properties. *Thin solid films*, 469 – 470, (2004), 254 – 262.
- [118] Sekkal C. et al. Tribologically transformed structure of titanium alloy (TiAl6V84) in surface fatigue induced by repeated impacts. *Materials science engineering A – structures*. 393, (2005), 140 – 146.
- [119] Guillou M. O. et al. The measurement of surface contact fatigue and its application to engineering ceramics. *Materials science engineering A-structures*. 209, (1996), 116 – 127.
- [120] Klaasen H., Kübarsepp J. Wear of advanced cemented carbides for metalforming tool materials. *Wear*, 256, (2004), 846 – 853.
- [121] Klaasen, H. et al. Peculiarities of hardmetals wear in blanking of sheet metals. *Tribology International*, 39, (2006), 303 – 309.
- [122] Kübarsepp J. et al. Performance of cemented carbides in cyclic loading wear conditions. *Materials science forum*, 534 – 536, (2007), 1221 – 1224.
- [123] Bunshah R. F. *Handbook of hard coatings*. Noyes Publications/William Andrew Publishing LLC., New York, 2001.
- [124] Kübarsepp J., Klaasen H., Pirso J. Behaviour of TiC-base cermets in different wear conditions. *Wear*, 249, (2001), 229 – 234.
- [125] Hussainova I. Effect of micro-structure on the erosive wear of titanium carbide based cermets. *Wear*, 255, (2003), 121 – 128.
- [126] Kollo L., Volobujeva O. Reactive sintering of (Ti,W)C-Ni and TiCFeNiSi cermets from high-energy milled powders. *Proceedings of Euro PM 2007 Congress and Exhibition, Toulouse, France, 14 – 17 Oct., 1, 2007*, 227 – 231.

-
- [127] Podgursky V., Nisumaa R., Gregor A., Adoberg E., Kulu P. Roughness of TiN and nanocomposite (nc-Ti_{1-x}Al_xN)/(a-Si₃N₄) evaluated by means of AFM. (2008). Roughness of TiN and Nanocomposite nc-Ti_{1-x}Al_xN/a-Si₃N₄ Surface Evaluated by Means of AFM. *Latvijas Kimijas Zurnals*, 1, 62 - 66.
- [128] Carlsson P., Olsson M. PVD coatings for sheet metal forming processes – a tribological evaluation. *Surface and coatings technology*, 200, 14-15, (2006), 4654-4663.
- [129] Annuka H., Klaasen H., Kübarsepp J., Suvi V. Adhesive wear behaviour of carbide composites and tool steels. 4th International DAAAM Conference “Industrial engineering – innovation as competitive edge for SME”, 29 - 30th April 2004, Tallinn, Estonia.
- [130] Veprek S., Veprek-Heijman M. J.G. Industrial applications of superhard nanocomposite coatings. *Surface & Coatings Technology*, 202, (2008), 5069.
- [131] Jiang N., Shen Y.G, Zhang H.J., Bao S.N., Hou X.Y. Superhard nanocomposite Ti–Al–Si–N films deposited by reactive unbalanced magnetron sputtering. *Materials Science and Engineering*, B, 135, (2006), 1–9.
- [132] Jilek M., Cselle T., Holubar P., Morstein M., Veprek-Heijman M. G. J., Veprek Stan. Development of Novel Coating Technology by Vacuum Arc with Rotating Cathodes for Industrial Production of nc-(Al_{1-x}Ti_x)N/a-Si₃N₄ Superhard Nanocomposite Coatings for Dry, Hard Machining. *Plasma chemistry and plasma processing*, Vol. 24, No. 4, (2004), 493-510.
- [133] Choi E. Y., Park J. H., Kim K. H. Synthesis and mechanical properties of Ti-Al-Si-C-N coatings by hybrid coating system. *Materials science forum*, Vol. 569, (2008), 105 – 108.
- [134] Yaldiz C. E., Veinthal R., Gregor A., Georgiadis K. Determination of the mechanical properties of thin hard coatings using nanoindentation. *Estonian Journal of Engineering*. 2009, 15, 4, 329 – 339.
- [135] Musil. J., Kune F., Zeman H., Polakova H. Relationships between hardness, Young’s modulus and elastic recovery in hard composite coatings. *Surface and Coatings Technology*, 154, (2002), 304 – 313.
- [136] Bouzakis K.-D., Siganos A., Leyendecker T., Erkens G., Thin hard coatings fracture propagation during the impact test, *Thin Solid Films*, vol. 460, (2004), p. 181–189.
- [137] Musil. J., Kune F., Zeman H., Polakova H. Relationships between hardness, Young’s modulus and elastic recovery in hard composite coatings. *Surface and Coatings Technology*, 154, (2002), 304 – 313.
- [138] Bouzakis K.-D., Siganos A., Leyendecker T., Erkens G., Thin hard coatings fracture propagation during the impact test, *Thin Solid Films*, vol. 460, (2004), p. 181–189.

-
- [139] Kulu P., Saarna M., Sergejev F., Gregor A., Surzenkov A. Selection of coating systems and processes for different wear conditions. 18th International Congress of the ABM, July 26 – 30th 2010, Rio de Janeiro – RJ – Brazil.
- [140] Palmqvist S. The work for the formation of a crack during Vickers indentation as a measure of the toughness of hard metals (in German), Arch. Eisenhüttenwes., 1962, 33, 629 – 34.
- [141] Murakami Y., Metal Fatigue: Effects of Small Defects and Nonmetallic Inclusions, Elsevier Science Ltd., UK, 2002.
- [142] Bouzakis K.-D., Siganos A. Fracture initiation mechanisms of thin hard coatings during the impact test, Surface and Coating Technology, 185, (2004), 150-159.
- [143] Bouzakis et al., The influence of the coating thickness on its strength properties and on the milling performance of PVD coated inserts, Surface and Coating. Technology, 174 –175, (2003), 393–401.
- [144] Bouzakis et al., Thin hard coatings fracture propagation during the impact test, Thin Solid Films, 460, (2004), 181–189.
- [145] Batista, J. C. A et al. An approach to elucidate the different response of PVD coatings in different tribological tests. Surface and coatings technology, 2003, 174-175, 891-898.
- [146] Haider J., Rahman M., Corcoran B., Hashmi M. S. J. Simulation of thermal stress in magnetron sputtered thin film coating by finite element analysis. Journal of materials processing technology, 168, (2005), 36 – 41.
- [147] Almond E.A. Hardmetals. Mater. Des., 7, (1986), 324-329.
- [148] Upadhyaya G.S. Cemented tungsten carbides - production, properties, and testing, William Andrew Publishing/Noyes, 1998.
- [149] Hutchings I.M. Tribology: Friction and Wear of Engineering Materials, Edward Arnold, UK, 1992.
- [150] Wood R.J.K. The sand erosion performance of coatings, Mater. Des., 20, (1999), 179–191.
- [151] M. Antonov et al., Solid particle erosion of Cr₃C₂-Ni metal-matrix composites, Proceedings of OST-01 Symposium on Machine Design, (2001), 233–243.
- [152] B. Farahmand, Fracture Mechanics of Metals, Composites, Welds, and Bolted Joints - Application of LEFM, EPFM, and FMDM Theory, Springer – Verlag, 2001.
- [153] Surzenkov, A.; Kulu, P.; Gregor, A.; Vuoristo, P.; Latokartano, J.; Ruppenen, M. (2008). Laser Treatment of PVD Coated Carbon Steels and Powder Steels. In: Materials Science-Medžiagotyra: 17th International Baltic Conference "Materials Engineering 2008", 6-7 November 2008, Kaunas, Lithuania. (Edit.) Tamulevičius, S. Kaunas, Lithuania: Kaunas Technologija, (2008) 301 - 305.

-
- [154] Möller W., Mukherjee S. Plasma-based ion implantation. *Current science*, 83, 3, (2002), 237 – 253.
- [155] Musil J., Kunc F., Zeman H., Polakova H. Relationships between hardness, Young's modulus and elastic recovery in hard nanocomposite coatings. *Surface and Coatings Technology*, 154, (2002), 304 – 313.

LIST OF PUBLICATIONS

- a. Sivitski A., **Gregor A.**, Saarna M., Kulu P., Sergejev F. Properties and performance of hard coatings on tool steels under cyclic indentation. *Acta Mechanica Slovaca*. Vol 13, No. 4, 2009, 84 – 94.
- b. Sivitski A., **Gregor A.**, Saarna M., Kulu P., Sergejev F. Indentation method application for cracking resistance evaluation of hard coatings on tool steels. – *Estonian Journal of Engineering*, 2009, 15, 4, 309 – 317.
- c. Yaldiz C. E, Veinthal R., **Gregor A.**, Georgiadis K. Determination of the mechanical properties of thin hard coatings using nanoindentation. *Estonian Journal of Engineering*, 2009, 15, 4, 329 – 339.
- d. Antonov M., Hussainova I., Sergejev F., Kulu P., **Gregor A.** Assessment of gradient and nanogradient PVD coatings behaviour under erosive, abrasive and impact wear conditions. *Wear*, 2009, 267, 898 – 906.
- e. Podgursky V., Nisumaa R., **Gregor A.**, Adoberg E., Kulu P. Roughness of TiN and nanocomposite (nc-Al_{1-x}Ti_xN/a-Si₃N₄) evaluated by means of AFM. – *Latvijas Kimijaz Zurnals*, 2008, 1, 62-66.
- f. Podgursky V., Torp B., Traksmaa R., Veinthal R., Viljus M., Coddet O., Morstein M., **Gregor A.**, Kulu P. Investigation of (Ti, Al)N based coatings grown by physical vapour deposition. – *Materials Science (Medziagotyra)*, 2005, 11, 4., 352 – 355, ISSN 1392 – 1320.
- g. Podgursky V., **Gregor A.**, Adoberg E., Kulu P. Wear of hard coatings, evaluated by means of kaloMax. *Proc. Estonian Acad. Sci. Eng.*, 2006, 12, 4, 419 – 426.
- h. Sergejev, F., Antonov, M., **Gregor, A.**, Hussainova, I., Kulu, P., Kübarsepp, J. Investigation of the surface fatigue of carbide composites and PVD hard coatings. – 6th International DAAAM Baltic Conference Industrial Engineering, 2008, 543 – 548.
- i. Surzhenkov A., Kulu P., **Gregor A.**, Vuoristo P., Latokartano J., M. Ruppenen. Laser treatment of PVD coated carbon steels and powder steels. – *Materials Science (Medziagotyra)*, 2008, 14, 4, 301 – 305, ISSN 1392 – 1320.
- j. **Gregor A.**, Podgursky V., Adoberg E., Kulu P. Hard Coatings manufacturing technology used in tooling. – 5th International DAAAM Conference „Industrial Engineering – Adding Innovation Capacity of Labour Force and Entrepreneurs“. 2006, 255 – 260.

ABSTRACT

Functional properties of PVD hard coatings play an essential role in an increasing number of industrial applications as sheet metal forming, cutting, milling, drilling, turning, sawing, punching and tapping. PVD coatings as they appear in different forms as mono -, nano - and multilayer's, gradient coatings and nanocomposites are widely used on the surface of wear components because of their excellent combination of mechanical properties - high hardness combined with low coefficient of friction, high oxidation resistance, and high state of residual stresses. At service conditions the correct selection of substrate material and thermal treatment; the selection of coating, type, thickness and process parameters are essential. Often incorrect selection of any of those listed parameters can lead to surface cracking and delamination of the coating.

This thesis gives an overview of AIP PVD technology and methods suitable for characterizing thin PVD hard coatings. Interactions between coating and substrate structure and properties are the subject analysed in this thesis.

As a result a good numeric and image database of cracking, wear and scratch resistance, microstructure, residual stresses, nanohardness, surface roughness and CoF of five different PVD coatings was obtained that enables us to compare the characteristics of the coatings with new experimental coatings with modified process parameters combined with modified surface treatment i.e. duplex treatment or duplex coating methods. The careful selection of process type and parameters, type and consistence of the coating and substrate material could enable us to produce thick PVD coatings that can be used on tools to extend the tool life boundaries even further. The integration of CNT-s into a structure of the coating could lead to a new paradigm in development of hard PVD coatings– Thick-Hard-Yet-Tough coatings.

Keywords: PVD coatings, AIP, surface fatigue, wear resistance, nanohardness, residual stresses, nanocomposites.

KOKKUVÕTE

Füüsikaliselt aurustussadestatud kõvapinnete funktsionaalsed omadused etendavad olulist rolli mitmetes tööstuslikes rakendustes nagu lehtvormimisel, lõikamisel, freesimisel, puurimisel, treimisel, saagimisel, stantsimisel, keermestamisel. Füüsikaliselt aurustussadestatud pinnakatted esinevad mitmel erineval kujul – mono-, nano-, mitmekihilised, gradientsed ja nanokomposiitsed pinnakatted. Nad on laialdaselt kasutusel kuluvdetatilide pindade katmisel, just nende pinnakatete suurepärase mehaanikaliste omaduste tõttu – suur kõvadus kombineerituna madala hõõrdeteguriga, kõrge oksüdatsiooniline stabiilsus ja kõrge jääkpingete osakaal. Töötingimustes on õige alusmaterjali ja selle termotötluse valik, pinnakatte valik, pinnakatte tüüp, pinnakatte paksus ja pindamisprotsessi parameetrite valik määrav. Sageli kas või ühe eespool nimetatud parameetri väär valik võib viia pinnakatte mõranemiseni ning järkjärgulise pinnakatte eemaldumiseni.

See töö annab hea statistilise ja graafilise andmete kogumi viie erineva füüsikaliselt aurustussadestatud pinnakatte hõõrdeteguri, pinnakareduse, nanokõvaduse, mikrostruktuuri, jääkpingete ja pinnaväsimuse omaduste kohta, mis võimaldab meil võrrelda antud pinnete omadusi juba uute eksperimentaalsete pinnakatetega, mis saadakse pindamisprotsessi parameetreid varieerides ning kombineerituna omakorda teiste pinnatötlustehnoloogiatega ehk duplex töötusega või duplex pinde meetodiga. Pindamisprotsessi ja selle parameetrite, pinde ja alusmaterjali tüübi ning koostise hoolikas valik võib võimaldada luua “paksusid” füüsikaliselt aurustussadestatud pinnakatteid, mis leiaksid rakendust tööriistamajanduses ning võimaldaksid suurendada tööriista püsivusaega enamgi. Süsiniknanotorude integreerimine pinnakatte struktuuri võib viia uue paradigmani pinnakatete arengus – üheaegselt kõvade, sitkete ning paksude pinnakateteni.

CURRICULUM VITAE (CV)

1. Personal data
- | | |
|-------------------------|------------------------------|
| Name and surname | Andre Gregor |
| Date and place of birth | 29.05.1980, Tallinn, Estonia |
| Citizenship | Estonian |

2. Contact information
- | | |
|---------|---|
| Address | Kummeli tee 90, 11912, Tallinn, Estonia |
| Phone | +372 56652349 |
| E-mail | andre.gregor@ttu.ee |

3. Education

Educational institution		
TUT Faculty of Mechanical Engineering, Production Engineering	2004	Master of Engineering scientist
Tallinn College of Engineering, Automotive Engineering	2002	Diploma of Automotive Engineering
Tallinn Üldgümnaasium	1998	Secondary education

4. Language competence/skills (native; fluent; average; basic skills)

Language	Level
Estonian	native language
English	average level
Finnish	average level
Russian	average level

5. Special Courses

Name of the course	Time of the study and place	Educational organization
PERA project management courses	October 2008, Melton Mowbray, UK	PERA Innovation Ltd.
Belbin's teamwork and roles	October 12 th 2006, Pärnu, Estonia	IMG Konsultant AS
Technology Transfer and Innovation; Techniques and Tools	October 2 nd to 6 th , 2006, Bologna, Italy	University of Bologna
Loewe ProCollege – LCD and Plasma TV-s	September 25 th to 26 th , 2006, Kronach, Germany	Loewe AG

DTA Engine Management Systems	July 20 th , 2006, Manchester, UK	DTA Ltd.
TOEFL test course	February – May 2004, Tallinn Estonia	Tallinn University of Technology
Showroom sales, training	November 11 th 2002, Tallinn, Estonia	Silberauto AS
Statoil International Seminar in lubricants and lubricating technology	October 25 th to 26 th 2000, Tallinn, Estonia	Statoil in co-operation with Tallinn College of Engineering

6. Professional Employment

Period	Organization	Position
2008 – ...	Eesti Innovatsiooni Instituut OÜ (PERA Estonia)	Project manager
2009 – 2010	Tallinn University of Technology, Institute of Thermal Engineering	Project manager
2007 – 2009	Tallinn University of Technology	Researcher
2006 – 2007	TUT Centre of Technology and Innovation	Technology Transfer Specialist
2005 – 2006	Tallinn University of Technology	Researcher
2005	Nisstek Ltd., Maldon, Essex, UK	Engineer
2004	Terry Hoyle Racing Engineers Ltd., Maldon, Essex, UK	Engineer
2001 – 2004	Balmoral OÜ	Bosch Service manager
2000 – 2002	Tallinn College of Engineering	Assistant
2000	Tulika Autoteeninduse OÜ	MOT technician

7. Scientific work

Papers are shown in pages

Related projects

Period of the project	Project name	Project no. and budget
2008 – 2013	SF 0140091908	3 MEEK

2009 – 2010	Project “Increasing the availability of qualified engineers and technicians for the car sale and service companies and for the MOT stations with the goal to avoid the increase of unemployment of young and elder employed people”.	IN9046 – applied research, budget 3.172 MEEK.
2007 – 2008	“The development of training courses for the material and quality engineers in the area of polymer and composite materials”.	IN7081 – applied research, budget 1.766 MEEK.
2006 – 2007	Project “The development of disintegrator for fine ceramic powders”, an order from company – Primet Precision Materials Inc., USA.	V337 – applied research, budget 175000 EEK
2005 – 2006	Project “High Technology Hard PVD Coatings for Tooling”	517F – applied research, budget 2.775 MEEK.

8. Thesis defended under supervision
 - a) The design of automation of Froude Consine F249 hydraulic dynamometer. Bachelor degree, *Mart Soodla*, 2007.
 - b) Laser treatment of surfaces and coatings. Master degree, *Andrei Surzenkov*, 2007
9. Main areas of scientific work/Current research topics
 - a) Wear resistant materials and wear (hard coatings, technology and properties). SF0142505s03
 - b) Hard coatings and surface technology. SF0140091s08
 - c) New technology for plastic waste utilization. ETF7705
10. Other research projects
 - a) Self-healing composites and damage indicating coatings. EU FP7, R4SMEs (Functional materials) - ca. 15 MEEK
 - b) Fuel additives. EAS, EU27821 – 200000 EEK

ELULOOKIRJELDUS

1. Isikuandmed

Ees- ja perekonnanimi Andre Gregor
Sünniaeg ja -koht 29.05.1980, Tallinn
Kodakondsus eestlane

2. Kontaktandmed

Aadress Kummeli tee 90, 11912 Tallinn
Telefon +372 56652349
E-posti aadress: andre.gregor@ttu.ee

3. Hariduskäik

Õppeasutus (nimetus lõpetamise ajal)	Lõpetamise aeg	Haridus (eriala/kraad)
TTÜ Mehaanikateaduskond, Tootmistehnika õppesuund	2004	Materjalitehnika, tehnikateaduste magister
Tallinna Tehnikakõrgkool, Autoinseneri õppesuund	2002	Autoinsener, diplom
Tallinna Üldgümnaasium	1998	Keskharidus

4. Keelteoskus (alg-, kesk- või kõrgtase)

Keel	Tase
Eesti	emakeel
Inglise	kesktase
Soome	kesktase
Vene	kesktase

5. Täiendusõpe

Täiendusõppe nimetus	Õppimise aeg ja koht	Täiendusõppe läbiviija nimetus
PERA projektijuhtimise koolitus	Oktoober 2008, Melton Mowbray, Inglismaa	PERA Innovation Ltd.
Koostöö ja Belbini meeskonnarollid	12 oktoober 2006, Pärnu, Eesti	IMG Konsultant AS
Tehnoloogiasirde ja innovatsioonitehnikad	02-06 oktoober 2006, Bologna, Itaalia	University of Bologna
Loewe ProCollege seminar	25-26 september 2006, Kronach, Saksamaa	Loewe AG
DTA	20 juuli 2006,	DTA Ltd.

mootorijuhtseadmete koolitus	Manchester, Inglismaa	
Toefl testi ettevalmistuskursus	Veebruar- mai 2004, Tallinn, Eesti	Tallinna Tehnikaülikool
Mercedes Benz teeninduskoolitus	22.11.2002, Tallinn, Eesti	Silberauto AS
Statoil rahvusvaheline määrdeainete ja määrimistehnika seminar	25-26 oktoober 2000, Tallinn, Eesti	Statoil koostöös Tallinna Tehnikakõrgkooliga

6. Teenistuskäik

Töötamise aeg	Tööandja nimetus	Ametikoht
2008 –	Eesti Innovatsiooni Instituut OÜ (PERA Estonia)	Projektijuht
2009 – 2010	Tallinna Tehnikaülikool, Soojustehnika instituut	Projektijuht
2007 – 2009	Tallinna Tehnikaülikool, Materjalitehnika instituut	Erakorraline teadur
2006 – 2007	TTÜ Tehnoloogia – ja innovatsioonikeskus	Tehnoloogiasirde spetsialist
2005 – 2006	Tallinna Tehnikaülikool	Erakorraline teadur
2005	Nisstek Ltd., Inglismaa	Insener
2004	Terry Hoyle Racing Engineers Ltd., Inglismaa	Insener
2001 – 2004	Balmoral OÜ	Bosch töökoja juhataja
2000 – 2002	Tallinna Tehnikakõrgkool	Assistent
2000	Tulika Autoteeninduse OÜ	Tehnoülevaatuspunkti töötaja

7. Teadustegevus

2008 – 2009	Projekt “Kvalifitseeritud tööjõu pakkumise suurendamine autode müügi- ja teenindusettevõtetele ning tehnoulevaatuspunktidele, lisaeesmärgiga ennetada töötavate noorte ja vanemaealiste töötajate tööturult väljalangemist”.	IN9046 – Täiendkoolitusprojekt, rakendusuring (eelarve 3.172 MEEK).
2007 – 2008	Projekt “Täiendkoolitus ja e-õppe süsteemi väljaarendamine materjalitehnoloogidele ning kvaliteediinseneridele polümeer- ja komposiitmaterjalide valdkonnas”.	IN7081 – Täiendkoolitusprojekt, rakendusuring (eelarve 1.766 MEEK).

2006 – 2007	Teadustöö tellimus firmalt Primet Precision Materials Inc.	V337 – Desintegraatori projekteerimine ja valmistamine, rakendusuuring (eelarve 175 tuhat EEK).
2005 – 2006	Projekt “Kõrgtehnoloogilised kõvapinded tööriistamajanduses”	517F – Õhukeste kõvapinnete kasutamine tööriistamajanduses, rakendusuuring (eelarve 2.775 MEEK).

8. Juhendamisel kaitstud lõputööd

a) Soodla, magistrant (teadus), 2007, (juh) **Andre Gregor**, FROUDE CONSINE F249 hüdraulilise dünamomeetri automatiseerimine (FROUDE CONSINE F249 hüdraulilise dünamomeetri automatiseerimine), Tallinna Tehnikaülikool, Mehaanikateaduskond, Materjalitehnika instituut

b) Andrei Surzenkov, magistrikraad (teaduskraad), 2007, (juh) **Andre Gregor**, Pindade ning pinnete lasertöötlus (Pindade ning pinnete lasertöötlus), Tallinna Tehnikaülikool, Mehaanikateaduskond, Materjalitehnika instituut

9. Teadustöö põhisuunad

- a) Kulumiskindlad materjalid ja kulumine (pinnakatted, tehnoloogia ja omadused) SF0142505s03
- b) Kõvapinded ja pinnatehnika SF0140091s08
- c) Uus komposiitplastjäätmete taaskasutustehnoloogia ETF7705

10. Teised uurimisprojektid

- a) Iseparanevad, mehaanilist kahjustust inditseerivad komposiitmaterjalid (funktsionaalsed materjalid), Euroopa 7RP projekt, R4SMEs, 2009-2010.
- b) Eeluring “Kütuselisandid”, EAS, EU27821, 2008